Organic Template-Assisted Synthesis & Characterization of Active Materials for Li-ion Batteries

By

Chae-Ho Yim

A thesis submitted to the Faculty of Graduate and Postdoctoral Studies in partial fulfillment of the requirements for the degree of Master's of Applied Science

In

Department of Chemical and Biological Engineering
Faculty of Engineering
University of Ottawa

Acknowledgements

I would like to sincerely thank my supervisors, Dr. Elena Baranova and Dr. Yaser Abu-Lebdeh, for their guidance, support and continued encouragement throughout my research. I truthfully appreciate their inspiring suggestions and efforts to provide the best research environment.

I appreciate the permission to use all the equipment available at ICPET-NRC for my research from Dr. Isobel Davidson.

I would like to thank my colleagues at ICPET-NRC: Dr. Fabrice Courtel and Dr. Hugues Duncan for their technical and professional advice.

I appreciate the help in materials characterization from the following people: Mr. David Kinston for SEM and Mr. Gilles Robertson for TGA measurements, at ICPET-NRC.
I would like to thank Mrs. Svetlana Niketic and Mrs. Dominique Duguay for the preparations and supply of batteries, which ensured that my research ran smoothly.

I would also like to thank my colleagues from the Laboratory of Electrochemical Engineering at the University of Ottawa—Paul Kim, Thegy Lomosco, Alexandra Tavasoli, Jihad Arafa, Tariq Amir, Benoit Clavette, and Noemie Dorval-Courchesne—for open discussions on electrochemistry.

Last but not least, I would like to extend my thanks to my family. Thank you to my mother, Mi-Gyoung Yim, and my brothers, Chol-Ho Yim and Shin-Hyo Yim, for their continuous love and support. Also, my gratitude goes to my father, Dr. Young-Bae Yim, who passed away a long time ago, for teaching and guiding me in my childhood to become a good engineer and scientist, just like he was.

Abstract

The Lithium-ion (Li-ion) battery is one of the major topics currently studied as a potential way to help in reducing greenhouse gas emissions. Major car manufacturers are interested in adapting the Li-ion battery in the power trains of Plug-in Hybrid Electric Vehicles (PHEV) to improve fuel efficiency. Materials currently used for Li-ion batteries are $LiCoO_2$ (LCO) and graphite—the first materials successfully integrated by Sony into Li-ion batteries. However, due to the high cost and polluting effect of cobalt (Co), and the low volumetric capacity of graphite, new materials are being sought out. $LiFePO_4$ (LFP) and SnO_2 are both good alternatives for the cathode and anode materials in Li-ion batteries. But, to create high-performance batteries, nano-sized carbon-coated particles of LFP and SnO_2 are required. The present work attempts to develop a new synthesis method for these materials: organic template-assisted synthesis for three-dimensionally ordered macroporous (3DOM) LFP and porous SnO_2. With the newly developed synthesis, highly pure materials were successfully synthesized and tested in Li-ion batteries. The obtained capacity for LFP was 158m Ah/g, which is equivalent to 93% of the theoretical capacity. The obtained capacity for SnO_2 was 700 mAh/g, which is equivalent to 90% of the theoretical capacity. Moreover, Hybrid Pulse Power Characterization (HPPC) was used to test LFP and LCO for comparison and feasibility in PHEVs. HPPC is generally used to test the feasibility and capacity fade for PHEVs. It simulates battery use in various driving conditions of PHEVs to study pulse energy consumption and regeneration. In this case, HPPC was conducted on a half-cell battery for the first time to study the phenomena on a single active material, LFP or LCO. Based on the HPPC results, LFP proved to be more practical for use in PHEVs.

Table of content

List of Figures

List of Tables

Chapter 1 Introduction

1.1 Background

Finding a solution for reducing hydrocarbon use and developing renewable energy sources has been a hot topic in recent years. The energy crisis that people have experienced in the last decade has indicated the need to develop and invest in renewable energy. The Lithium-ion battery is one of the possible solutions for energy production and storage that will reduce the use of hydrocarbon fuel and hence the amount of greenhouse gas generation. This type of battery has been used quite extensively in small portable devices. However, the use of Li-ion batteries for mid- to industrial-sized devices presents some challenges. The Li-ion battery has attracted significant attention from car manufacturers who are looking to improve fuel efficiency and reduce greenhouse gas production. Electric Vehicle is the holy grail of the car manufacturers for zero emission vehicles, but this is farfetched using with the current technology. The main focus of the automobile industry is to develop a Plug-in Hybrid

Electric Vehicle (PHEV) using the Li-ion battery as a power source and energy-storage system for the vehicle.

Recently, there has been extensive research in battery safety and performance in electric vehicles. However, the active materials currently used in Li-ion batteries pose a few problems that need to be resolved before the batteries can be used in PHEVs. $LiCoO_2$ (LCO) is the cathode material currently in use. However, cobalt is expensive and has a negative effect on the environment. $LiFePO_4$ (LFP) is suggested as a cheaper and environmentally benign alternative for the cathode material. However, due to the low electric conductivity of LFP, it is necessary to use nanocrystal-sized and carbon-coated LFP. The anode material currently in use is graphite, which has a low capacity compared to other available materials. SnO_2 is suggested as an alternative due to its high theoretical capacity. However, due to the large volume expansion of SnO_2 during battery operation, it is necessary to use nanocrystal-sized and carbon-coated SnO_2.

Another concern regarding the application of Li-ion batteries in PHEVs is the capability to withstand a pulse charge/discharge. Hybrid Pulse Power Characterization (HPPC) is a common testing simulation for Li-ion batteries that examines the capability of extreme charge/discharge rates and the aging of Li-ion batteries. In this thesis, HPPC protocol was tested on a half-cell battery for the first time to study the phenomena of the active material. Most HPPCs reported in literature have been performed only on the full cell.

1.2 Research objectives

The overall research objectives of this thesis were to develop highly efficient and stable material for electrodes during the repeated charging and discharging. Moreover, develop an inexpensive cathode materials compared to the $LiCoO_2$ and demonstrate the performance of these novel materials in Li-ion batteries used in PHEVs. The specific research goals were the following:

1. To develop a synthesis route in order to obtain three-dimensionally ordered macroporous (3DOM) $LiFePO_4$ to controlled crystal size and carbon coating, using the organic template method.
2. To develop a synthetic route in order to prepare porous SnO_2 to controlled size, structure and optimal carbon coating, using the developed organic template synthesis.
3. To perform battery testing under conditions similar to those during PHEV operation using HPPC simulation on a half-cell LFP battery in order to study the material behaviour during extreme charge/discharge, as well as its stability; to compare the new cathode materials with current state-of-the-art materials, e.g. $LiCoO_2$.

1.3 Thesis structure

This thesis consists of three main chapters of results (chapters 3 to 5), corresponding to research objectives 1, 2 and 3. Chapter 1 gives a short introduction of the subject matter and objectives of this work. Chapter 2 contains literature reviews and Chapter 6 contains conclusions as well as discussion of future work.

Chapter 2 presents literature reviews on various battery types, the fundamentals of batteries, currently used and suggested active materials, as well as characterization methods used to test active materials and batteries.

Chapter 3 discusses new synthesis routes for 3DOM LFP (i.e. organic template-assisted synthesis), as well as the characterization and battery performance results of LFP.

Chapter 4 presents the new synthetic method for porous SnO_2 (i.e. organic template-assisted synthesis via hydrothermal reaction), as well as the characterization and battery performance results of SnO_2.

Chapter 5 discusses the results of the first HPPC testing conducted on a half-cell battery with LFP active material and its comparison to LCO.

Finally, Chapter 6 summarizes the main findings of this thesis and discusses potential topics for future research.

Chapter 2

Literature Review

2.1 Fundamentals of batteries

A battery is an electrochemical device that converts chemical energy into electrical energy during discharge. Generally, it comprises three components: an anode, a cathode and an electrolyte. The anode is a negative electrode that provides electrons from an active material through an oxidation reaction, where active material is the material that generates or accepts electron by means of redox reaction. The electrons produced from the anode's active material are transferred through the external circuit to the cathode. The cathode is a positive electrode that, in turn, accepts the electrons and causes the reduction of an active material in the cathode. The electrolyte is a material that provides ionic conductivity to transfer the oxidized or reduced chemicals from the anode to the cathode, or vice versa during charging.

In a battery, these three components work together, using oxidation-reduction (redox) reactions in the anode and cathode as well as mass transfer through the electrolyte, to turn chemical energy into electrical energy. Figure 2.1 demonstrates this simple process.

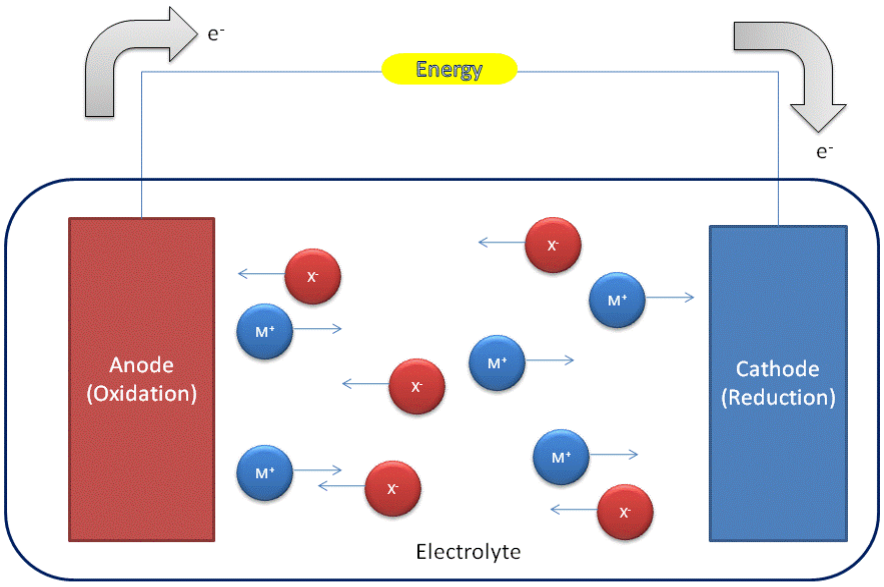

Figure 2.1 Fundamental processes in a battery during discharging

2.1.1 Classification of batteries

Batteries can be divided into three types, based on their main application: primary, secondary and reserve. From these, more classifications are possible based on the battery structure or design.

2.1.1.1 Primary batteries

Primary batteries are generally disposable and non-rechargeable. Most primary batteries are dry cells, which use an absorbent or separator as an electrolyte. Common primary batteries are carbon-zinc, alkaline and lithium batteries.

The carbon-zinc battery is the most common battery produced worldwide. It uses zinc for the cathode, manganese oxide (MnO_2) for the anode and an aqueous solution of zinc chloride ($ZnCl_2$) for the electrolyte. One type of carbon-zinc battery is the Leclanché cell. The wet Leclanché cell was first invented in 1876 by Georges Leclanché, and the dry Leclanché cell was first introduced in 1888 by Dr. Carl Gassner. Since then, continuous improvements have been made to develop the current state-of-the-art carbon-zinc battery. Figure 2.2 illustrates the typical carbon-zinc cell. Due to the long history and development of the carbon-zinc battery, it can be produced in any design and size at a low cost.

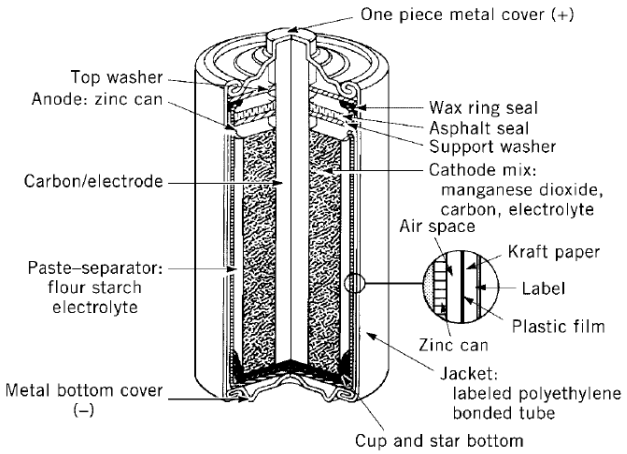

Figure 2.2 Typical carbon-zinc cell (Leclanché cell)[1]

Alkaline batteries use an alkaline aqueous electrolyte such as potassium or sodium hydroxide. Zinc is a common choice for the anode material, while a variety of materials can be used for the cathode. Figure 2.3 shows the cross-section of a cylindrical alkaline cell. Unlike the carbon-zinc cell, the alkaline cell uses a carbon electrode as a current collector. Moreover, in an alkaline cell, the electrolyte is mixed with the anode material instead of with the cathode material. Due to the high conductivity and low polarization of alkaline electrolytes, the battery can run close to the theoretical capacities of the active materials: zinc and the cathode material (MnO_2, HgO, Ag_2O and O_2). As a result, minimal amounts of active materials are required to build a high-performance battery that shows less capacity variation at different discharge rates. The only disadvantage of the alkaline cell when compared to the carbon-zinc cell is the higher cost. This higher cost can be attributed to the high purity of the active materials and the complex design of the battery. However, with research and development, the cost has been reduced by minimizing the use of the active materials and electrolytes.[1]

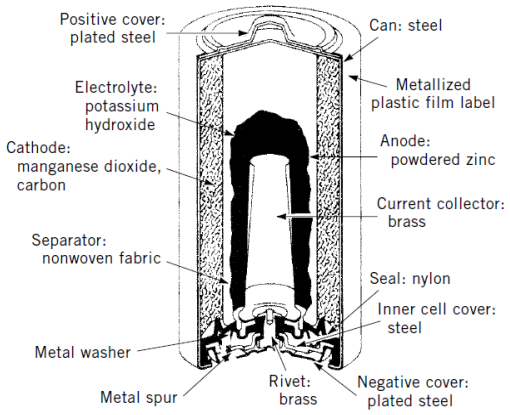

Figure 2.3 Cylindrical alkaline cell[1]

Lithium batteries use lithium for the anode, regardless of the cathode material. Lithium is the lightest metal and has a high energy density, which gives about 3.8 Ah/g of the theoretical specific capacity and 3.7 V of the potential. This voltage is more than two times higher than that of carbon-zinc or alkaline batteries. Due to the high performance of the lithium battery, it is commonly used for important devices that require long life such as artificial pacemakers. With careful review of cost-efficiency, it can also be used in other devices instead of alkaline batteries for longer life. The main reason for the high cost of lithium batteries is the high reactivity of the lithium metal, which requires great care and attention to numerous safety factors; such as explosion due to increase of temperature and pressure, short circuiting, and leakage of the electrolytes.

2.1.1.2 Secondary batteries

Secondary batteries are known as rechargeable batteries. The reversible redox reactions in the electrodes cause the battery to charge and discharge, making the battery reusable. Common secondary batteries include alkaline, lead-acid and lithium-ion (Li-ion) batteries.

In the previous section, alkaline batteries were introduced as primary batteries. However, depending on the active materials, they can also be used as secondary batteries, which also use potassium hydroxide as the electrolyte. The only criteria for the active materials in secondary alkaline batteries are safety and irreversibility. Possible cathode materials for secondary alkaline batteries include the oxide or hydroxide forms of copper, manganese, mercury and nickel. Possible anode materials include cadmium, iron and zinc. A

well-known secondary alkaline battery is the Nickel-cadmium (NiCd) battery. However, due to the low energy density and environmental hazard of cadmium, new materials for the alkaline battery have been developed. These new batteries, also known as NiMH, use a hydrogen-absorbing alloy for the anode. Until the Li-ion battery was introduced, NiMH batteries were used extensively in electric vehicles due to their acceptable performance and reasonable cost.

Lead-acid batteries use lead oxide for the cathode, lead (Pb) for the anode and sulphuric acid (H_2SO_4) for the electrolyte. They are one of the most successful secondary batteries due to their low manufacturing cost and high columbic efficiency (~95%). Their applications are diverse, although they are mainly used in the automotive industry. Lead-acid batteries are the most widely known and successful secondary battery. However, due to their low energy density, their application in weight-sensitive devices such as electric vehicles and small electric devices is limited.

Lithium-ion (Li-ion) batteries have been extensively studied in recent decades, due to their high energy and power density, and low capacity fade. They were first introduced in the 1970s by M. S. Whittingham, and then commercialized in 1991 by Sony. Lithium cobalt oxide is the main material used for the cathode, graphite for the anode, and lithium salt ($LiPF_6$, $LiBF_4$ or $LiClO_4$) in an organic solvent (e.g. ethylene carbonate) for the electrolyte. Due to the high energy density of Li-ion batteries, they have been integrated into small portable devices such as laptops, cell phones, cameras, camcorders and MP3 players. Moreover, their application in electric vehicles is growing. The main disadvantages of these batteries are the high material cost of $LiCoO_2$ (LCO), which occupies 70% of Li-ion battery material cost. Moreover, LCO is a hazard that may harm or irritate eyes, skin or the

respiratory tract and may cause harm if swallowed. Nonetheless, as more and more new active materials for Li-ion batteries are being introduced, there is promise for a less expensive and environmentally benign battery in the future.

2.1.1.3 Reserve batteries

Reserve batteries are commonly used for industrial purposes due to their long inactive storage ability and high-intensity discharge use. To obtain high-intensity discharge use with long-term storage, a key component—an anode, a cathode or an electrolyte—has to be separated from the battery system and mechanically activated when required. A common anode material is lithium due to its low standard potentials. Cathodes and electrolytes vary, depending on the application of the battery. One example of a reserve battery is the lithium-water battery, which is used in marine environments where water is easily accessible.

2.1.2 Electrochemical processes in batteries

To obtain good electrical energy from a chemical reaction, spontaneous redox reactions of anode and cathode materials are required. However, to control energy use in a battery and prevent spontaneous redox reactions (also known as short circuiting), it is necessary to separate the anode and the cathode. An electrolyte is used to achieve this physical separation. The electrolyte has to have good ionic conductivity, but no electrical conductivity, in order to obtain a good physical separation of the electrodes that will prevent short circuiting. Ionic conductivity is a measure of conductivity through ionic charged carriers, for Li-ion battery the conductivity of lithium ion in the organic solvent. As a result,

electrons produced from the redox reaction will transfer through the external circuit only when the circuit is closed.

As mentioned earlier, a spontaneous redox reaction produces a flow of electrons or current through an external circuit of a battery, resulting in the production of electrical energy. The main driving force of battery discharge is the thermodynamics of the active materials at the electrodes, where the Gibbs free energy (ΔG) is negative with positive potential ($^{0}E_{cell}$). As mentioned earlier, the electrodes are assembled as if the chemical reaction is separated into two half-reactions. One half reaction, which occurs at the anode, favours the oxidation that will produce the electrons. The other half-reaction, which occurs at the cathode, favours the reduction that will accept the electrons. The potential strength of the oxidation and reduction is generally known and can be obtained in a general chemistry textbook.[2] Table 2.1 summarizes some useful values.

Table 2.1 Selected standard electrode potentials[2]

Reaction	E^0, Potential (V)
$Li^+ + e^- \rightleftarrows Li$	-3.045
$Co^{3+} + e^- \rightleftarrows Co^{2+}$	1.92
$Fe^{3+} + e^- \rightleftarrows Fe^{2+}$	0.771
$Mn^{3+} + e- \rightleftarrows Mn^{2+}$	1.5
$Zn^{2+} + 2e^- \rightleftarrows Zn$	-0.7626
$Pb^{2+} + 2e^- \rightleftarrows Pb$	-0.1251
$Ni^{2+} + 2e^- \rightleftarrows Ni$	-0.257
$Cd^{2+} + 2e^- \rightleftarrows Cd$	-0.4025

Based on Table 2.1, lithium has the lowest potential (E^0), making it a strong oxidizing agent. Due to their high potentials, transition metals (i.e. cobalt, iron, manganese and nickel) are currently used in Li-ion batteries for the counter half reactions. As a result, the pairing of lithium with transition metals gives a high voltage range of up to 3.7 V.

One difference between primary and secondary batteries is the reversibility of the redox reactions at the active materials. In a Li-ion battery, the active materials consist of lithium insertion materials that cause the lithium ion to shuttle or rock between the cathode and anode during charge/discharge. This is the main reason why the Li-ion battery is also called a “rocking-chair cell”. Figure 2.4 shows a good schematic of a Li-ion battery from Patil et al. (2008).

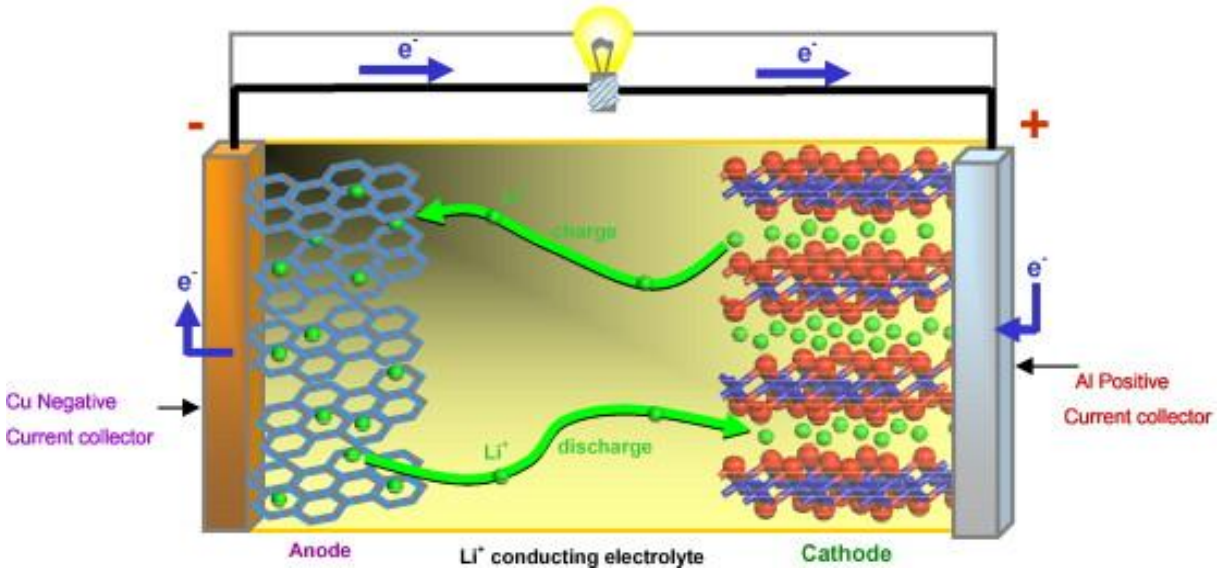

Figure 2.4 Schematic of Li-ion battery[3] – The rocking of Li^+ is shown during charge/discharge

2.1.3 Thermodynamics of batteries

As mentioned in previous chapters, a battery is a storage device that converts chemical energy into electrical energy. To estimate the amount of useful energy that results from the reaction, Gibbs free energy can be used. The reaction in the battery can be generalized as follows:

$$aA + bB \leftrightarrow cC + dD \quad \textbf{2.1}$$

$$aA + e^- \leftrightarrow cC \quad \textbf{2.2}$$

$$bB \leftrightarrow dD + e^- \quad \textbf{2.3}$$

The reaction shown is not a detailed illustration of the mechanism of electron movement, which is the main source of battery energy for electrical power. A detailed description of the electron movement during the reaction can be better demonstrated as two half reactions. During one half reaction, one element in the battery undergoes oxidation favourable to thermodynamics and produces electrons (Equation **2.2**), which will also be the material of the half reaction at the anode during the discharge. The electrons produced from the anode will be transferred through the external circuit and will reach the cathode—the counter electrode—during the discharge. As mentioned earlier, the chemistry for the discharge in the battery is set to favour the thermodynamics of the reaction, meaning that the reaction is spontaneous and that Gibbs free energy is negative. The battery also contains a physical barrier to prevent a spontaneous reaction and allow control only by the electron transfer through the external circuit.

The electron kinetics caused by a chemical reaction in an electrochemical cell is described by Faraday's law as shown in Equation **2.4**. The Faraday's law describes the mass of a substance altered and the charge produced when the currents flow are produced through the external circuit

$$m_i = -\frac{s_i M_i I t}{nF} \qquad \textbf{2.4}$$

Where:

m_i = mass of species i

s_i = stoichiometric coefficient of a reaction

M_i = molecular weight

I = current passed

t = time

n = number of electrons transferred

F = Faraday's constant, 96487 coulombs/equivalent

Electrochemical redox reactions in batteries can be described thermodynamically using Gibbs free energy (ΔG). As known, the value of the Gibbs free energy has to be negative to promote a spontaneous reaction. Gibbs free energy in coupled half reactions is obtained by the production of electrons, resulting in current within a circuit to produce energy, as described by Faraday's law. Using Faraday's law, Gibbs free energy from the electrochemical cell can be described as follows:

$$\Delta G = -nFE \quad \textbf{2.5}$$

Gibbs free energy related to the equilibrium constant K is shown as follows:

$$\Delta G^0 = -RT \ln K_{eq} \quad \textbf{2.6}$$

For bulk chemical reactions:

$$\Delta G = \Delta G^0 + RT \ln K \quad \textbf{2.7}$$

where K is based on Equation **2.1**:

$$K = \frac{[C]^c[D]^d}{[A]^a[B]^b} \quad \textbf{2.8}$$

Using previous equations **2.5** to **2.8**:

$$E = E^0 - \frac{RT}{nF} \ln K \quad \textbf{2.9}$$

Equation **2.9**, known as the Nernst equation, is the potential during the reaction that takes into account only the concentration of the active materials in the electrodes. When other factors in the battery (such as the diffusion of ions in the electrolytes, the polarization

of the electrodes and electrolytes, and the rates of the reactions at the electrodes) considered, different phenomena are needed to simulate the change of the potentials and currents.

2.2 Battery characterization

As previously discussed, a battery is an energy storage device that comprises three major components: an anode, a cathode and an electrolyte. To characterize the battery, the battery must be simplified. In most cases, researchers conducted testing in half-cell batteries. For instance, a half-cell battery uses lithium metal for the anode while the cathode is an active material that needs to be characterized. The battery produces a current and potential difference throughout the circuit. Controlling and applying this current and potential difference makes it possible to characterize the active materials and to obtain useful information about battery performance.

The device that controls the potential of the battery is called a potentiostat. By applying different potentials to the battery or to the active materials, it is possible to measure and analyze the current produced or consumed from the battery. A common application of the potentiaostat is cyclic voltammetry (CV). A detailed description of CV will be given in Chapter 2.2.2.1.

A galvanostat is a device that controls current to the battery or to the active materials and measures the potential during charge/discharge at different currents. To compare the performance of the different active materials, a C-rate (mA or A) is used to normalize the current to the amount of active materials, as described in the following equation:

$$C-rate=\frac{1}{t}C=\frac{SC\times m_{activematerial}}{t} \quad \textbf{2.10}$$

Where:

C = Capacity (mAh or Ah)

SC = Specific capacity of active material (mAh/g or Ah/g)

$m_{active\ material}$ = mass of active material used in the cell or battery (g)

t = duration to fully charge from fully discharged state (h)

The 1C of C-rate is defined as the amount of current necessary to use all of the specific capacity in one hour. Different C-rates are used to test the capacities of the active materials. Another application of the galvanostat in electric vehicles is HPPC, which will also be discussed in Chapter 2.2.2.2. HPPC is the process of applying a high pulse C-rate to a battery in order to simulate driving conditions of an electric vehicle. The potential is measured during the HPPC testing and characterized for electric vehicle use of the battery.

2.2.1 General definitions and phenomena of Li-ion batteries

Active materials used for the electrodes have the ability to intercalate lithium ions. During the redox reactions, the active materials produce electrons. It is possible to evaluate the theoretical capacity of an active material by estimating the number of electrons produced.

A common battery parameter is specific energy or power, which is defined as the energy or power available per unit of weight or volume. These parameters are essential when total weight or volume is an important factor in the application of the battery (e.g. in cell phones, laptops, MP3 players and electric vehicles). As discussed earlier, lithium has the smallest atomic number and therefore, the highest energy density and power, as shown in Figure 2.5 from Patil et al. (2008).[3] Even with the high energy density of the Li-ion battery, more improvements can be made using microstructure.[3] The discovery of materials with higher energy and power is a major reason why people still invest in Li-ion battery research.

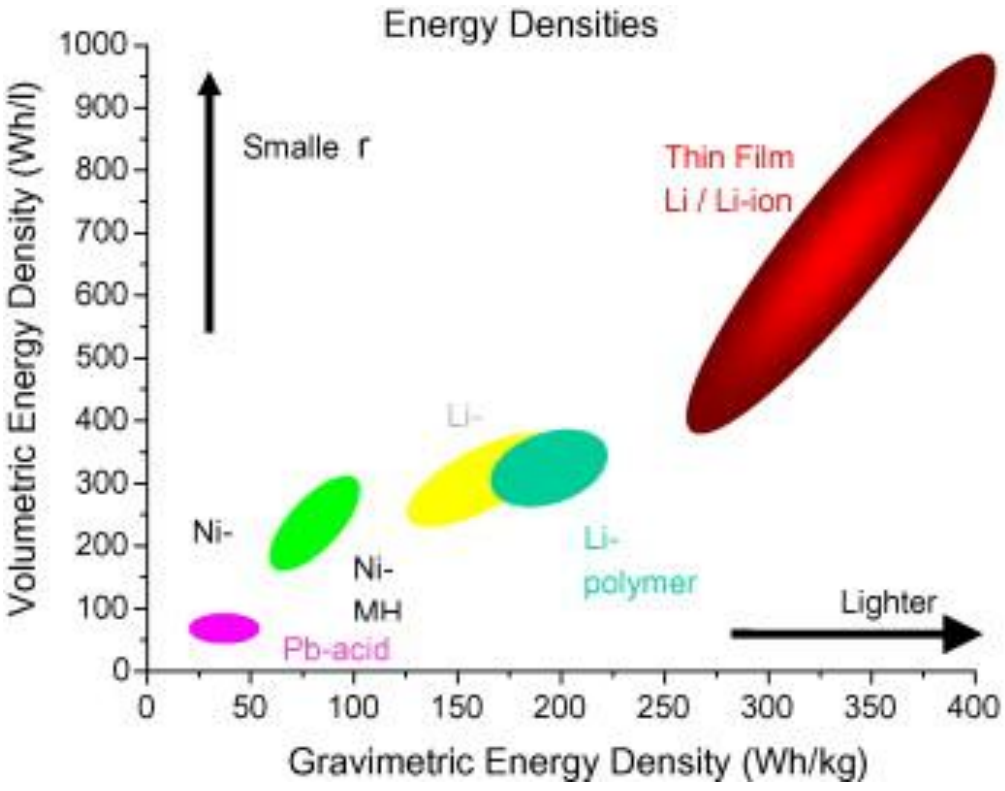

Figure 2.5 Comparison of energy density with various rechargeable batteries[3]

Power in electrical systems is defined as the porduct of potential (E) and current (I), as shown in Equation **2.11**. The same fundamental principle is used for specific energy: the integral of the potential (E), multiplied by the charge capacity (q). Moreover, the efficiency of the battery can be obtained using the energy used and produced during charge/discharge.

$$Power = EI \quad \textbf{2.11}$$

$$q = It \quad \textbf{2.12}$$

$$SE = \frac{\int Edq}{m_{active\ material}} \quad \textbf{2.13}$$

$$\varepsilon = \frac{SE_{Discharge}}{SE_{Charge}} \times 100\% \quad \textbf{2.14}$$

Where

I = Current (A)

q = charge produced or consumed (Ah)

t = time (h)

SE = Specific Energy (Wh/g)

E = Potential (V)

$m_{active\ materials}$ = Mass of a active material testing (g)

ε = Energy efficiency of a battery

Specific energy can be evaluated using Faraday's Law. The Faraday constant is the amount of electric charge per mole of electrons. Since the theoretical electrons produced during the reduction reaction of the active material is known, it is possible to calculate the specific energy. From the half reaction in Equation **2.15**, the specific energy can be evaluated using Equation **2.16**:

$$A^+ + ne^- \rightarrow A \qquad \textbf{2.15}$$

$$SC = \frac{nF}{MW_A} \qquad \textbf{2.16}$$

Where:

SC = Specific Capacity (Ah/g or mAh/g)

F = Faraday constant (96500 As/mol or C/mol)

n = number of electrons produced per mol of half reaction A

MW_A = Molecular weight of species A (g/mol)

Using Equation **2.16**, the theoretical capacities of common active materials are calculated. The values are summarized in Table 2.2. Some materials such as the metal oxides cannot achieve full capacity due to a change in the crystal structure when the lithium is intercalated. For $LiCoO_2$ in a fully charged state, a significant volume change, caused by the change in crystal structure[4], was observed by Amatucci et al. (1996). As a result, the particles breake and lose contact, leading to irreversible capacity loss, which has been found and

studied by others.[5-7] For this reason, less than 50% of the theoretical capacity can be used. Similar results were observed for other oxide-based active materials.

Table 2.2 Theoretical and practical capacities of common active materials

Type of electrodes	Active Materials	Theoretical Capacity (mAh/g)	Practical Capacity (mAh/g)
Cathode	$LiCoO_2$	274	140~160
	$LiMn_2O_4$	148	110
	$LiNiO_2$	275	220
	$LiFePO_4$	170	160
Anode	Graphite	372	320~330
	Sn	939	N/A
	Si	4010	N/A

As discussed earlier, phenomena within batteries are complex due to kinetic reactions at the electrodes and mass transfer trhough the electrolytes. The operating voltage depends on all the transport phenomena. Figure 2.6 shows a typical polarization curve. Figure 2.6 shows a relationship between the potential and the current while the electrochemical cell is operating. The open circuit potential in a fully charged battery can be obtained using Equation **2.9**. However, as soon as the battery is discharged, the potential drops. Region (I) in Figure 2.6 is a good example of a potential drop. Three main types of internal resistance

exist in a battery: internal resistance due to the electrodes themselves; resistance caused by the ionic conductivity of the electrolyte, and the interfacial resistance between the active material and the electrolyte. The main resistance in Region (I) is caused by the over voltage of charge transfer at the electrodes. This is also called charge transfer polarization and it is an example of internal resistance by the electrodes. Region (II) shows an increase of slopes, dV/dI, as the current passes, reflecting an increase of the cell's internal resistance. The main resistance in this region is caused by the ionic conductivity of the electrolytes, also called ohmic polarization. A voltage drop in Region (III) is caused by a lack of ion-accepting sites in the active materials.[8] To summarize the process, the following equation can be derived:

$$R_{Tot} = R_{electrolyte} + R_{Int} + R_{electrodes} \quad \textbf{2.17}$$

$$V = V_{OC} - IR_{Tot} \quad \textbf{2.18}$$

Where:

R_{Tot} = Total internal resistance

$R_{electrolyte}$ = Resistance due to ohmic polarization

R_{int} = Resistance due to diffusion polarization

$R_{eletrodes}$ = Resistance due to charge transfer polarization

V = operating voltage, V_{OC} = open-circuit voltage also equal to E^0

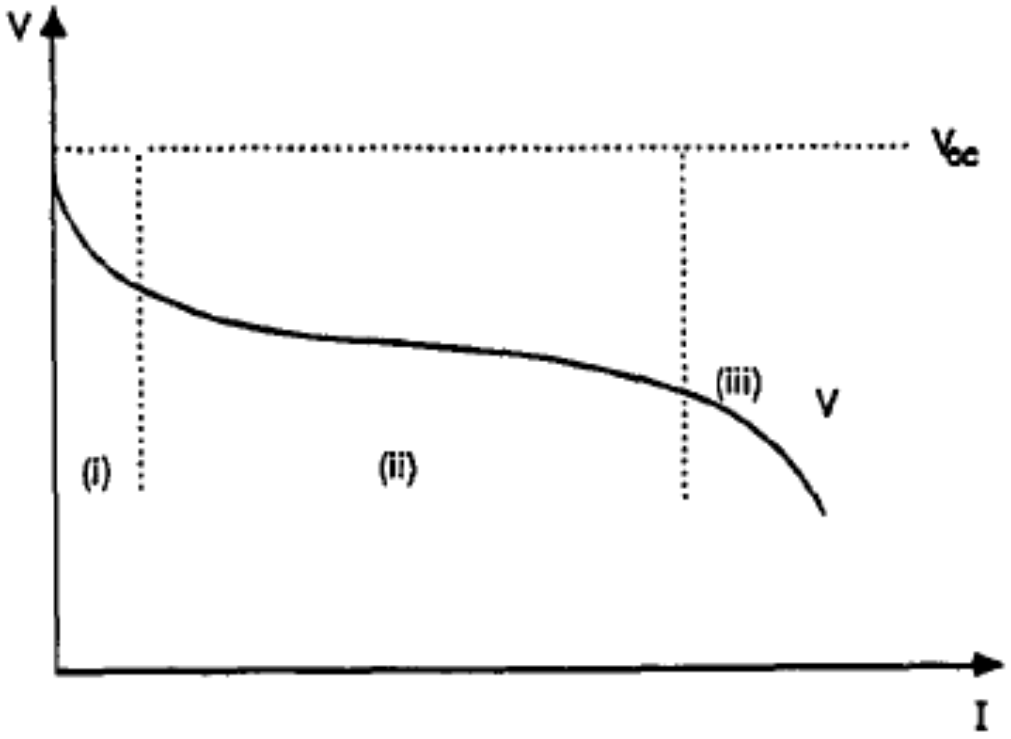

Figure 2.6 Typical polarization curve of Li-ion battery[8]

2.2.2 Electroanalytical techniques

Many steady and dynamic analytical techniques are available to characterize an electrochemical cell. Three main techniques have been used to test a battery: Cyclic voltammetry (CV) and hybrid pulse power characterization (HPPC).

2.2.2.1 Cyclic voltammetry (CV)

Cyclic voltammetry is the most common technique used in electroanalytical chemistry to study redox reaction phenomena.[9-15] It is a dynamic technique that involves measuring current when electrodes' potential is swept linearly and cycled between two designated potentials of interest. Due to the dynamic electroactive measurement of CV, a variety of substances (such as biomaterials, catalysts, materials for a battery and super capacitors[15]) can be tested to discover its electrochemical characteristics and reversibility.

Changes in the electrode potential cause a redox reaction of the material of interest at the electrode interface. The magnitude of the potential will depend on the redox coupling of the materials. The redox reaction of the material at the electrode interface will produce or supply electrons or current. This current can be measured and interpreted. From the obtained CV, the oxidation or reduction potentials are obtained, also from the repeatedly cycled result. It is also possible to find out the reversibility of the redox reaction. In order to obtain a reliable result, the rate of the potential sweep should be small enough to measure the current caused by the redox reaction, due to the slow diffusion of the materials at the electrodes interface. Detailed fundamentals of CV have been explained by many people including Kissinger et al. (1983 and 1984).[14, 15] Figure 2.7 shows the general potential change of the CV, which cycles the potential between -0.2 and 0.8 V.

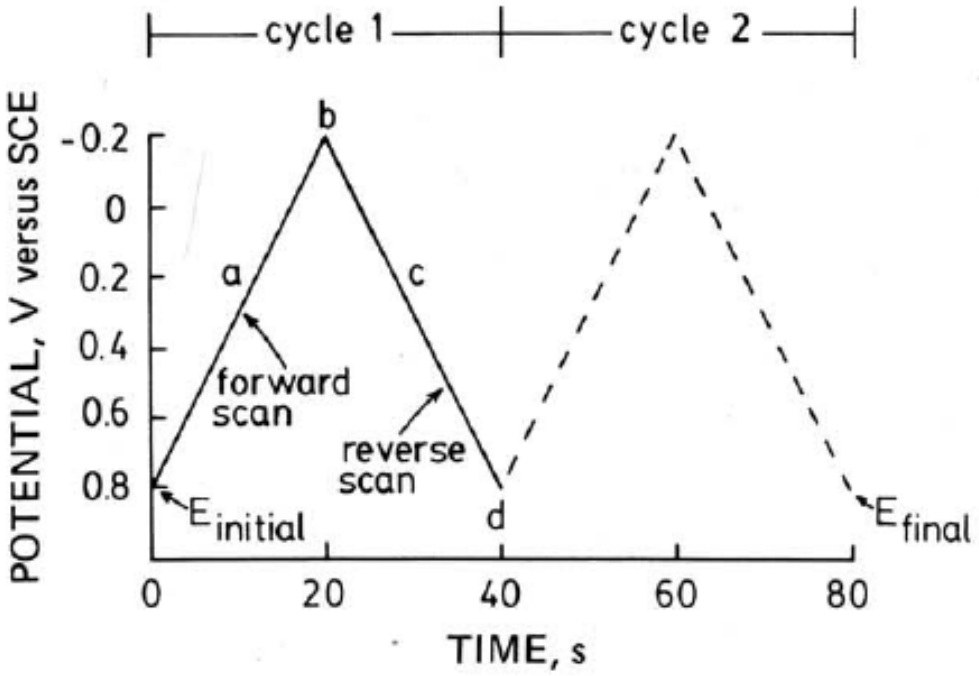

Figure 2.7 Typical excitation signal for CV[14] – a triangular potential waveform with switching potentials at 0.8 and 0.2V versus saturated calomel electrode.

Figure 2.8 shows the CV of $K_3Fe(CN)_6$. The redox peaks are caused by the oxidation of Fe ions in cyanide complex. When the potential is ramped down as shown in Figure 2.7, the Fe(III) ion reduces to Fe(II). When the potential is ramped up, the iron will oxidize back to Fe(III). During the linear sweep of the potential, electrons will be exchanged. The exchanged electrons can be obtained taking the difference of the two potential peaks at the anode and cathode for reversible redox reaction only, as shown in Equation **2.19**.

$$\Delta E_p = E_{pa} - E_{pc} = \frac{0.059}{n} \quad \textbf{2.19}$$

Where n is the number of electrons exchanged, and E_{pa} and E_{pc} are the potentials at the anode and cathode peaks. The open circuit potential of the system is at the centre of E_{pa} and E_{pc}, as shown in Equation **2.20**.

$$E^0 = \frac{E_{pa} + E_{pc}}{2} \quad \textbf{2.20}$$

Based on the results of the CV, reversibility can be determined by evaluating the i_{pa} and i_{pc}. For a general reversible reaction, the current produced or consumed must have similar values, as shown in the following equation:

$$\frac{i_{pa}}{i_{pc}} \approx 1 \quad \textbf{2.21}$$

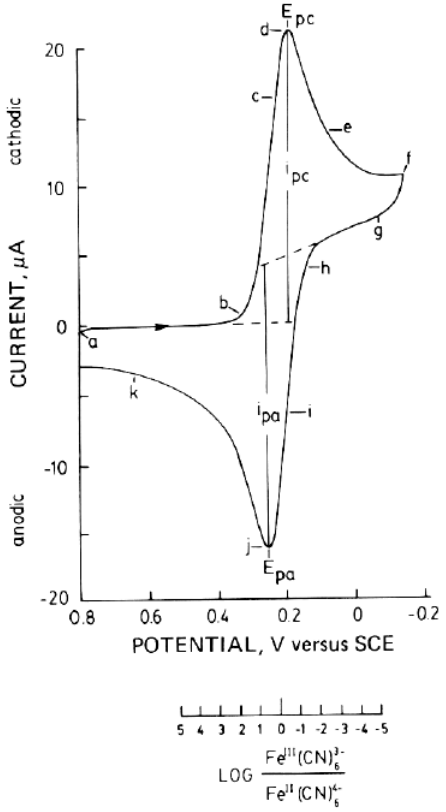

Figure 2.8 CVs of 6mM $K_3Fe(CN)_6$ in 1 M KNO_3[14] using the potential profile from Figure 2.7

Since the active materials in Li-ion batteries undergo redox reactions during charge/discharge, CV is an appropriate technique for studying the cycling behaviour during charge/discharge processes. It is also a great tool for finding the practical reversible potential range of the active materials. Figure 2.9 through Figure 2.13 show typical CVs of active materials used for Li-ion batteries. $LiCoO_2$, $LiMn_2O_4$ and $LiFePO_4$, were tested as cathode materials at different scan rates by Fu et al. (2005) and Takahashi (2002). For oxide materials, several redox peaks were observed. The main peaks were caused by the redox reaction of the

active materials, while the other smaller peaks were caused by the structural changes of the oxides.[16-20] For $LiFePO_4$, the only main redox peaks were observed due to the two-phase redox reaction, where the structural changes were maintained during intercalation of the lithium ion. As a result, only the main redox peaks appeared on the CV.[21] As previously explained, a faster scan rate results in wider and larger peaks due to the higher polarization of the electrodes.[2, 14, 15] For anode materials, CV was repeated to observe the reversibility of the materials. CVs obtained on graphite (Figure 2.12) by Yao et al. (2003)[22] show irreversible peaks that are the result of solid electrolyte interface (SEI) formation between 0.2 and 0.4 V during the first cycle. For SnO_2, an irreversible reduction of SnO_2 to Sn was observed between 1.25 and 1.5 V. Formation of SEI was also observed from the second cathode peak at approximately 0.65 V.

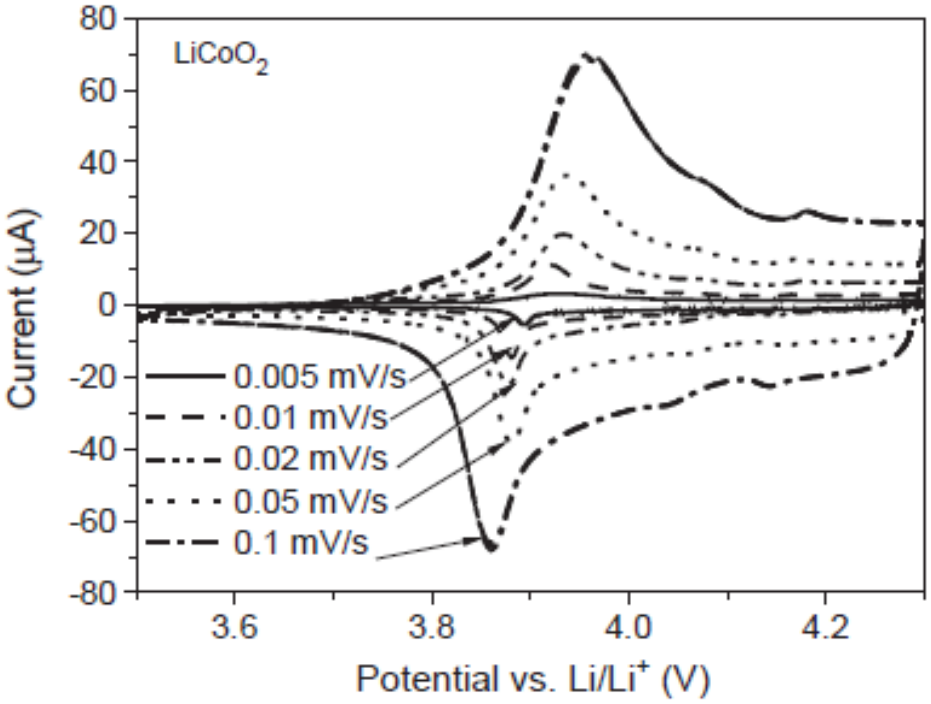

Figure 2.9 CVs of $LiCoO_2$ at different scan rates[23]

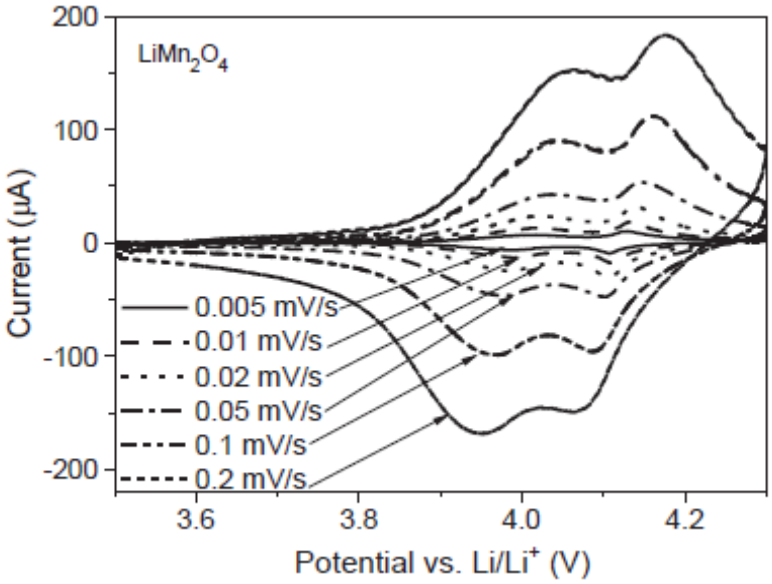

Figure 2.10 CVs of $LiMn_2O_4$ at different scan rates[23]

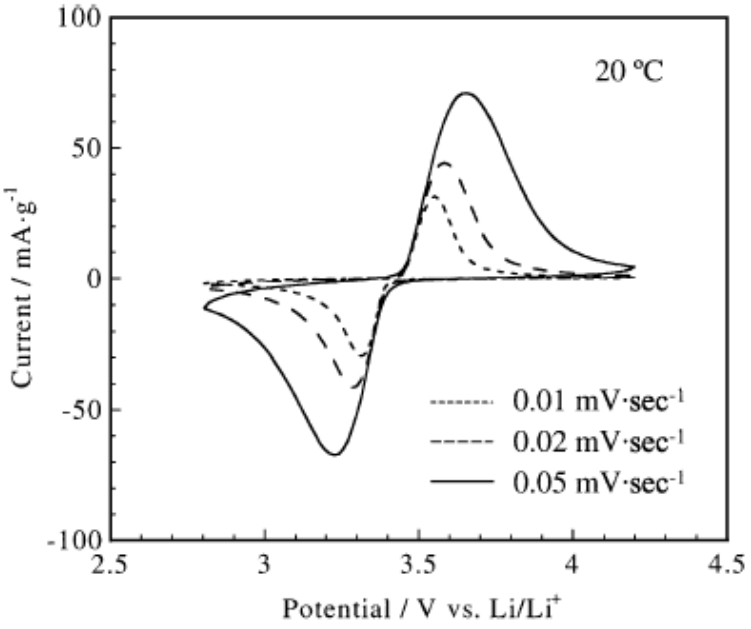

Figure 2.11 CVs of $LiFePO_4$ at different scan rates[24]

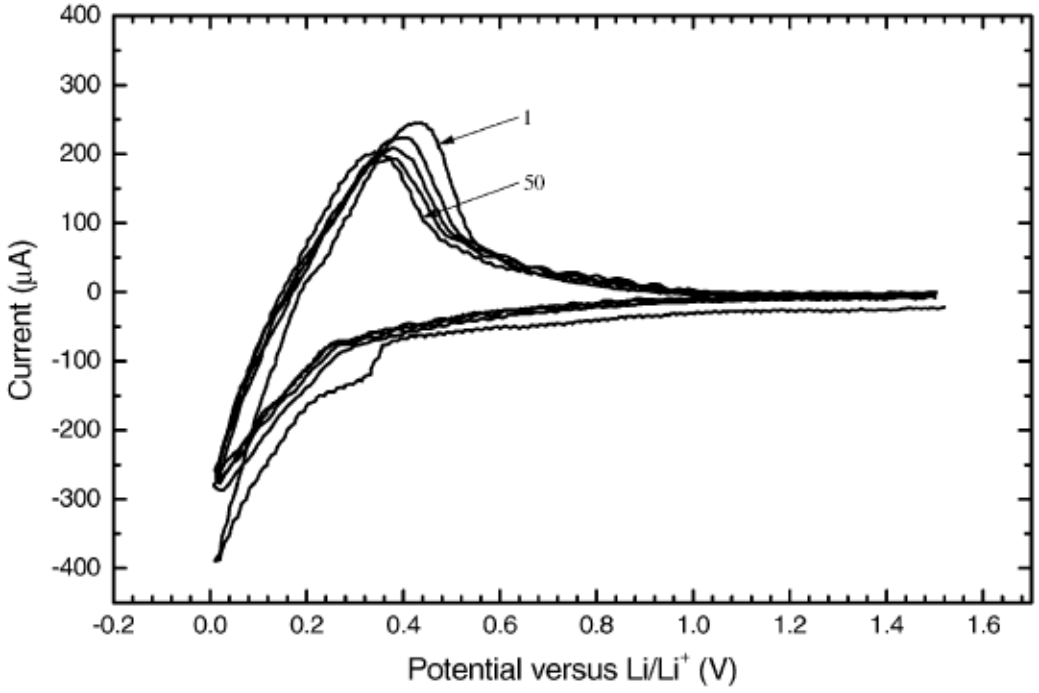

Figure 2.12 CVs of anode material MCMB[22]

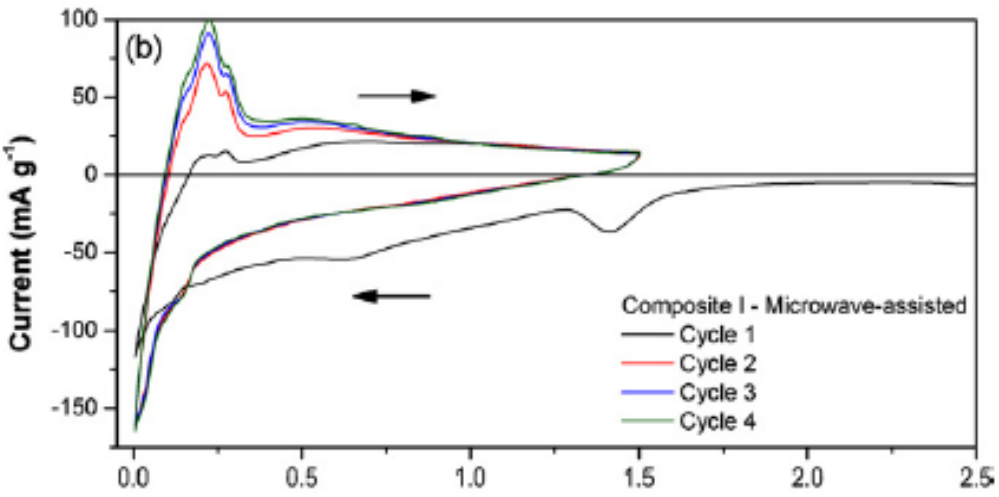

Figure 2.13 CV of SnO_2[25]

2.2.2.2 Hybrid pulse power characterization

Hybrid pulse power characterization was originally developed by the U.S. Department of Energy to test the capability of batteries used in hybrid electric vehicles. The original objective of HPPC testing was to establish the dynamic power capability of batteries using pulse charge/discharge at different states of charge (SOC). Another objective of the testing was to measure the ohmic polarization resistance of batteries. The HPPC testing comprises a simple driving model, which assumes the acceleration, cruising and deceleration conditions. During acceleration, the battery is discharged at a high pulse C-rate. During cruising, no power use from the battery is assumed. Finally, during deceleration, braking power is used to charge the battery also at a high pulse C-rate. This process is also called regeneration pulse. Table 2.3 and Figure 2.14 summarize the procedure of simple HPPC profiles.

Table 2.3 HPPC profile to test the batteries

Cumulative Time (s)	Time Increment (s)	C-rate	Condition
18	18	5C	Acceleration
50	32	0	Cruising
60	10	3.75C	Deceleration

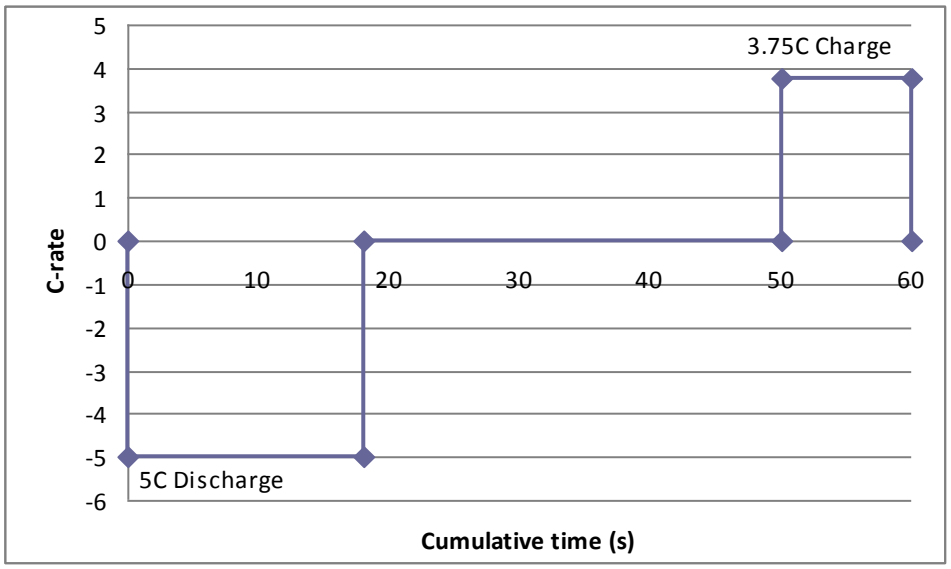

Figure 2.14 Graphical representation HPPC profile to test the batteries

HPPC testing has received great attention due to the application of the Li-ion battery in electric vehicles. Li-ion batteries have mostly been used in small electric devices that require a mild charge/discharge rate. However, in electric vehicles, the use of a battery is dynamic and extreme. For this reason, HPPC testing of the battery capability is strongly recommended. NiMH and Li-ion batteries were tested by Eskra et al. (2006)[26] and Belt et al. (2003).[27] The

results showed that both batteries could control the high pulse charge/discharge. Abraham et al. (2004 and 2005)[28, 29] studied the effect of HPPC on impedance and found that the impedance increased as the batteries were aged under HPPC testing. Holland et al. (2002)[30] studied a hybrid system of Li-ion batteries and super-capacitors using HPPC. They concluded that the use of a hybrid system did not improve the performance of the whole system. Their suggested method in the hybrid system was to use a higher fraction of pulse power from the super capacitor. A computational method was also used to predict the capacity and capability of HPPC.[31-33] Dees et al. (2008) successfully simulated the HPPC results by implementing electrochemical impedance spectroscopy models. Smith and Wang (2006)[33] predicted HPPC results by implementing solid-state diffusion limitation, which is one important aspect to improve for an active material, into the 1D electrochemical model developed by Doyle et al. (1993).[34]

2.3 Materials for batteries

Massive research has been conducted on active materials for anodes and cathodes.[35-43] The following is a list of criteria for active materials:

- allow large amount of lithium intercalation for maximum capacity;
- have good reversibility of lithium intercalation process;
- have good conduction of lithium ions and electrons;
- be chemically stable during lithium intercalation without reacting to electrolyte, and

- be easy to synthesize, inexpensive, environmentally benign and lightweight.

Based on these criteria, many materials have been suggested and studied as active materials. The first Li-ion battery, which was developed and commercialized by Sony, used lithium cobalt oxide for the cathode and graphite for the anode. However, cobalt is a rare, expensive and environmentally hazardous material[44]. In addition, graphite has a low capacity compared to lithium metal. As a result, newly developed materials are being sought out, including $LiMn_2O_4$, $LiNiO_2$, $LiFePO_4$ and LiV_2O4[37] for cathodes, and Sn, Si and $LiTi_5O_{12}$[35] for anodes. Even though these materials have an advantage over the active materials currently in use, there is still some lack of practicality, such as short life cycles, lack of experimental data. For the purposes of this thesis, two of the major materials will be studied: $LiFePO_4$ and SnO_2 that are promising and extensively studied active materials for Li-ion battery.

2.3.1 Olivine-based materials

Olivine is magnesium iron silicate ($(Mg,Fe)_2SiO_4$) categorized as a mineral. Olivine-based materials used for Li-ion battery has the same crystalline structure as olivine. Olivine-based materials, $LiMPO_4$ (M = Fe, Mn, Co, Ni), have received great attention since 1997, when Padhi et al. (1997)[21] introduced them. The olivine-based material, $LiMPO_4$, is an orthorhombic unit cell with a Pnma space group, which is well-ordered[45]. Figure 2.15 is a graphical representation of $LiFePO_4$. The one way to determine the crystalline materials is X-Ray Diffraction (XRD) analysis—a tool for analyzing crystal structures, atomic spacing

and phase purity of materials. Figure 2.16 shows the XRD patterns of the olivine materials. Table 2.4 shows the lattice parameters of $LiFePO_4$. Some papers report the space group of the olivine to be Pmnb; however, Table 2.4 shows that the difference in the space groups is caused by a different lattice as a standard point of view, where the lattice values for a and b are switched between Pnma and Pmnb.

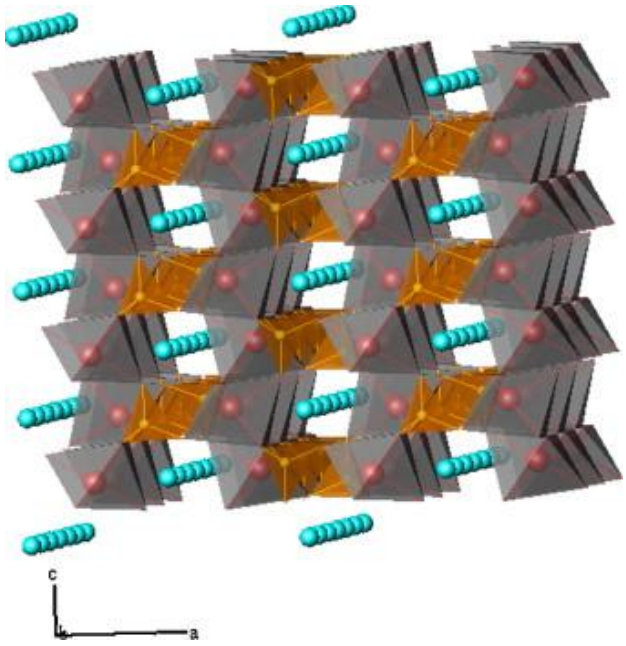

Figure 2.15 Structure of $LiFePO_4$[46] FeO_6 shown as a grey octahedral; PO_4 shown as a brown tetrahedral, and Li^+ shown as a blue sphere in the one-dimensional tunnel

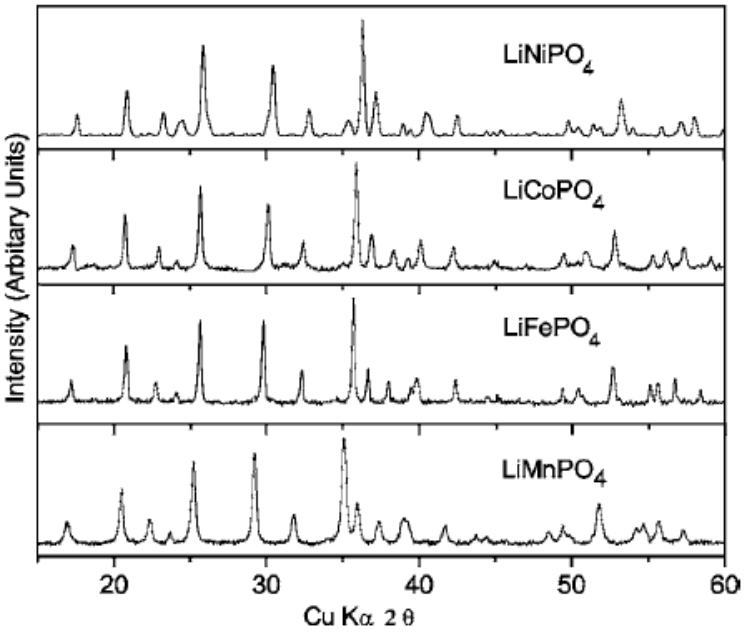

Figure 2.16 XRD patterns of olivine materials[47]

Table 2.4 Lattice parameters of $LiFePO_4$

	Space group	
Lattice parameters	Pnma	Pmnb
a (Å)	10	6.0
b (Å)	6.0	10
c (Å)	4.7	4.7

Figure 2.17 shows the theoretical capacities of olivine materials, which are calculated using Equation **2.16**. The theoretical capacities of olivine materials are much smaller

compared to those of oxide materials. However, due to the structural change of oxide materials during lithium intercalation, only half of the capacity (~140 mAh/g) or less can be used. For olivine material $LiFePO_4$, close to 80% (~140 mAh/g) of the theoretical capacity use was reported.[48-51] This is one of the major reasons why olivine materials are receiving so much attention as alternative cathode materials in Li-ion batteries. Another advantage of olivine materials is the flat discharge curve caused by the two-phase reaction[21] during lithium intercalation, as shown in Figure 2.17. During intercalation of lithium ion the $LiFePO_4/FePO_4$ exist as two crystalline that is why the intercalation of the $LiFePO_4$ is also called as a two-phase reaction. The constant potential output during the discharge gives great control over the pack of series or parallel-connected batteries in an electric vehicle.

Table 2.5 Theoretical capacity and operating potential of olivine materials

Olivine material	Theoretical Specific Capacity (mAh/g)	Operating Voltage (V)
$LiFePO_4$	169.9	3.5
$LiMnPO_4$	170.9	4.1
$LiNiPO_4$	166.9	5
$LiCoPO_4$	166.7	4.8

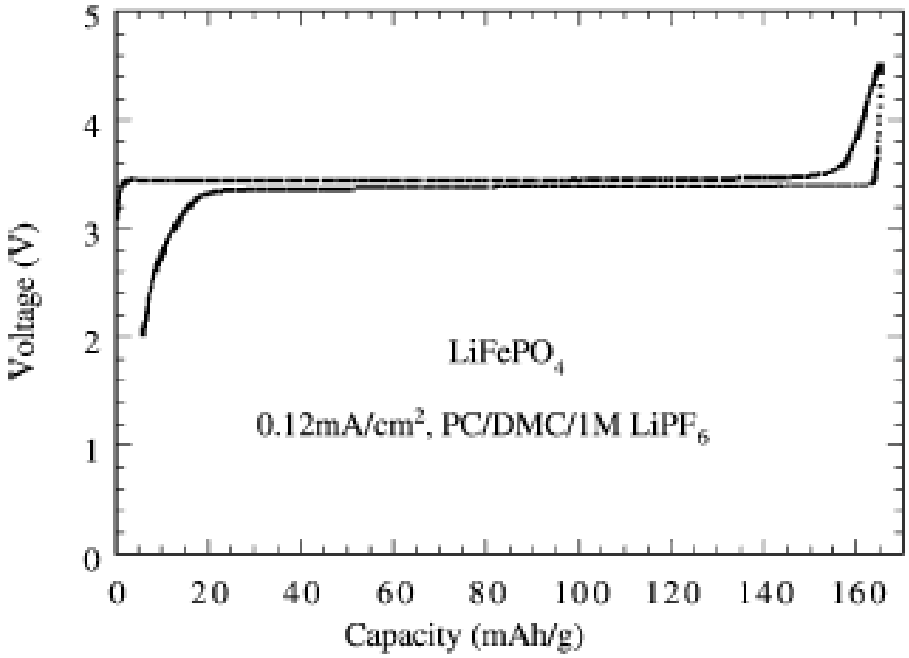

Figure 2.17 Charge/discharge curve of $LiFePO_4$[45]

Among all the olivine materials ($LiMPO_4$, M = Fe, Mn, Ni, and Co), $LiFePO_4$ (LFP) is one of the most promising and well-studied materials because it was the only material that was able to intercalate the lithium ion, as shown in the early studies of Padhi et al. (1997).[21] Other olivine materials such as $LiMnPO_4$ (LMP) have been synthesized with carbon coating to improve electrical conductivity; however, the battery performance of the LMP synthesized by Yang et al. (2006)[52] and Vadivel Murugan et al. (2009)[53] was unsuccessful compared to the LMP synthesized by Martha et al. (2009)[54] and Li et al. (2002)[35]. The reason for the success of the lithium intercalation in LMP is not known and further study is required. The same reasons are driving further studies of all other olivine materials ($LiNiPO_4$ or $LiCoPO_4$), except LFP.

2.1.1.1Synthesis of olivine materials

The electrochemical results of LFP in early stages were promising[21, 55, 56], but not strong enough to lead to a replacement of the current oxide material because of the low electronic conductivity of olivine materials. The poor performance of the LFP can be explained by the low electronic and lithium-ion conductivity. To overcome the low conductivities, the use of nano-sized and carbon-coated LFP was suggested[44]. The nano-sized particle of LFP reduces the intercalation path of lithium ion, and the carbon coating improves the electrical conductivity of LFP. To obtain nano-sized and carbon-coated material, the following methods are generally used: solid-state, hydrothermal and sol-gel syntheses. Many other syntheses are currently being studied and reviewed.[46, 57-59]

Solid-state synthesis was frequently used to synthesize the olivine structure.[21, 60] The basic concept of this synthesis is to promote the reaction in solid state by mixing and crushing the reactants at high temperatures. The advantage of this method is its simplicity. To synthesize the olivine material using a solid-state reaction, metal-based (Li and Fe) precursors (such as acetate, nitrate, oxalate and sulphate) are mixed with phosphate salts and carbon source. The mixed powders are ball milled at high temperatures (~700 ^{0}C) until the desired particle sizes are obtained. This method has been used in ceramic synthesis[46] and has also proven effective in mass-producing the cathode materials (LCO, LMO and LFP) in industry (A123 system INC and Phostec Lithium Inc.). However, the disadvantage of solid-state synthesis is the high heat and kinetic energy required to produce the final product. As a

result, other reactions such as sol-gel and template-assisted reactions need to be considered to achieve lower energy consumption synthesis.

A hydrothermal reaction is any heterogeneous reaction that occurs in the presence of a solvent at high temperatures and pressures in order to dissolve reactants and crystallize the final product. One of the advantages is that the crystal size and purity of the product can be easily controlled using surfactant[61]. Many people have reported successful synthesis of olivine materials using hydrothermal synthesis.[53, 59] However, depending on the conditions of the hydrothermal synthesis, heat treatment is necessary to change the amorphous $LiFePO_4$ into ordered crystals[53, 62]. Faster and simplified hydrothermal synthesis using a microwave to minimize the energy requirement during the reaction was reported.[53]

Sol-gel synthesis is a soft chemical process widely used in materials science and ceramic engineering. As the name suggests, the reactants are dissolved or suspended in a solution. The solution is polymerized to form a complex network of precursors. Due to the complex network, the particles are separated in nanoscale to perform nanoparticle crystal growth, which provides a basic fundamental of nanotechnology of bottom-up process. A sol-gel reaction is a great method of synthesizing nano-sized particles, which is an key factor for olivine materials to improve the conductivity in Li-ion batteries. Due to the simplicity of the synthesis, many sol-gel methods have been introduced.[40, 42, 48, 52, 63-70] There are many different types of solutions used in the sol-gel method, organic solvent, ethylene glycol and water, the most common of which being water.[65, 66, 68, 70, 71]

The three synthesis methods described above are the most common methods used to prepare olivine materials. It is hard to say which one is the best or most efficient method for

synthesizing olivine materials. As a result, many other methods including precipitation[72], microwave-assisted methods[73], polyol[74] and emulsion drying[75,47, 76, 77] are being introduced.

2.3.1.1 Methods to improve electronic conductivity of LFP

To improve the electronic conductivity of LFP, it is a common practice to carbon coat LFP particles.[48, 51, 68, 78] Most of the carbon coated LFP produced performs close to 80% (140 mAh/g) of the theoretical capacity in Li-ion batteries. Many studies were conducted related to the effect of the carbon and the carbon source. Dominko et al. (2005) showed the effect of carbon coating. The lowest amount of carbon in LFP composites obtained was 3.2 wt % and this particular amount corresponds to the carbon coating thickness of about 1-2 nm, which delivers close to 80% of the theoretical capacity at 1C.[68] Nien et al. (2009) showed physical and electrochemical properties of LFP from various polymer containing precursors. The results showed that the structure of polymer precursors played an important role in improving the performance of $LiFePO_4$/C composites.[79] The addition of carbon also has advantage of reducing the iron to Fe^{2+} in high temperature sintering process.[80]

The drawbacks of carbon coating are the need for additional processing to carbon coat LFP and the loss in energy density due to the electrochemically inert additive, which sometimes constitutes as much as 30 vol% of the resulting composite.[44] As a result, an alternative method to improve the electronic conductivity is suggested by doping the LFP.[71, 81] Chung et al. (2002) showed that doping by metals supervalent to Li^+ increases the electronic conductivity of LFP by a factor of 10^8.[81] Wang et al. (2006) studied on LFP and its

doped derivatives, where doped LFP demonstrated a stable discharge capacity of 160-165 mAh g-1, almost approaching the theoretical capacity.[71]

2.3.2 Tin oxide (SnO_2)

Based on the criteria for active materials in Li-ion batteries (described in section 2.3), carbon-based active materials are a popular choice due to their long life cycles, low cost and negligible volume expansion.[82] However, because of their small capacities (372 mAh/g) when compared to lithium metal (3746 mAh/g), other active materials are being sought out as alternatives. Tin (Sn) is one of the major candidates for the anode material. Along with other metal alloys such as Al, Si, Ge, Pb, Sb and Bi, Sn was one of the first metal alloys considered—even before carbon-based materials were tested[83]—due to its high specific capacity. A major drawback of using Sn or other metallic materials for the anode is the severe volume expansion during the intercalation of the lithium ion. This causes mechanical stress, leading to the pulverization of Sn and the loss of contacts for electron transfer at the electrodes during battery cycling. Table 2.6 compares the specific capacities and volume changes of various metals and carbon during lithium intercalation, leading to alloy formation.

Table 2.6 Specific capacities and volume changes of carbon and metal alloys[83]

Active material	C	Al	Si	Sn	Bi
Lithiated phase	LiC_6	Li_9Al_4	$Li_{21}Si_5$	$LI_{17}Sn_4$	Li_3Bi
Theoretical specific capacity (mAh/g)	372	2235	4010	959	385
Volume changes (%)	12	238	297	257	115

To overcome the capacity loss caused by the pulverization, a nano-szied particle of Sn with multiphase alloy matrices is suggested[84]. Many research and development efforts have been devoted to obtaining and optimizing the Sn-based materials.[84] SnO_2 is one of the main Sn-based materials currently studied.[25, 84-88]

SnO_2 are commonly used in many fields such as a catalyst for the oxidation of aromatic compounds, as an opacifier in the ceramic industry, or as a sensor in carbon monoxide detectors. SnO_2 crystallises in rutile structure with P42/mnm space group. Graphical representation is shown in Figure 2.18, and the XRD pattern are shown Figure 2.19.

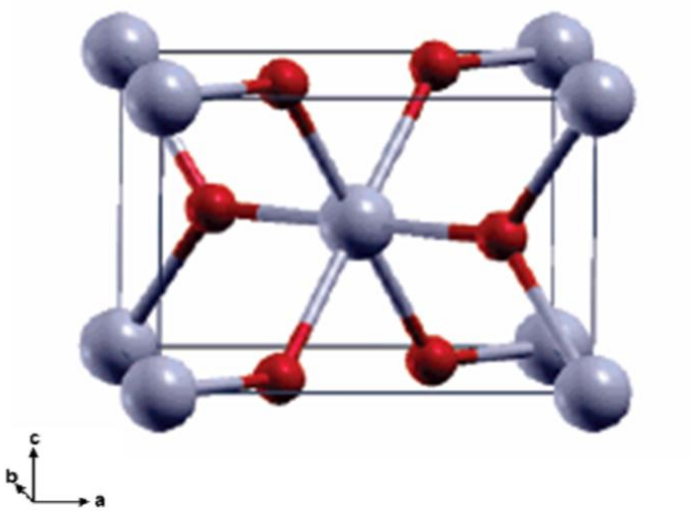

Figure 2.18 Structure of SnO_2 (gray and red colors represents Sn and O atoms, repectively), rutile unit cells with $P4_2/mnm$ space group[89]

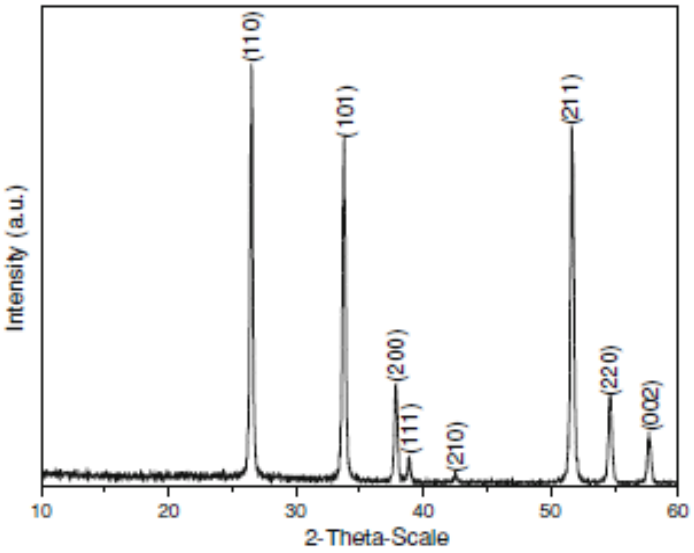

Figure 2.19 XRD pattern of SnO_2[90]

The fundamental reaction of tin oxide during lithium intercalation was studied by Courteny et al. (1997) [91]. It is shown in the following equations:

$$SnO_2 + 4Li^+ + 4e^- \rightarrow Sn + 2Li_2O \qquad \textbf{2.22}$$

$$Sn + xLi^+ + xe^- \leftrightarrow + Li_xSn \qquad \textbf{2.23}$$

Equation **2.22** is the first reaction, which occurs when lithium is inserted. It is an irreversible reaction that also helps form Sn nanoparticles, which will disperse homogeneously in a Li_2O matrix and from a composite. By activating SnO_2 to Sn and dispersing the Sn into the Li_2O network, the volume expansion caused by lithium ion is minimized, as so the rapid pulverization and the failure of Li-ion battery is prevented. Equation **2.23** shows the reversible reaction during the lithium intercalation.

As Courtney et al. (1999) showed, even with the help of Li_2O dispersion, the Li_2O network does not totally prevent the growth of Sn particles during lithium intercalation, eventually leading to pulverization of the material. As a result, some authors have suggested dispersing the Sn_2O within the carbon matrix.[25, 92-95] To prevent capacity fade resulting from the pulverization of Sn, many syntheses such as template-assisted synthesis,[96] microwave-assisted synthesis[40], molten salt synthesis[97], solvo-thermal synthesis[98] and polyol synthesis[25] were suggested.

2.4 References:

1. Blomgren, G.; Hunter, J., Batteries, Primary Cells. John Wiley & Sons, Inc.: 2000.

2. Bard, A. J.; Faulkner, L. R., ELECTROCHEMICAL METHODS: Fundamentals and Applications. John Wiley & Sons: New York, Chichester, Weinheim, Brisbane, Singapore, Toronto, 2001; p 833-833.

3. Patil, A.; Patil, V.; Wook Shin, D.; Choi, J. W.; Paik, D. S.; Yoon, S. J., Issue and challenges facing rechargeable thin film lithium batteries. Mater Res Bull 2008, 43, (8-9), 1913-1942.

4. Amatucci, G. G.; Tarascon, J. M.; Klein, L. C., CoO2, the end member of the LixCoO2 solid solution. Journal of the Electrochemical Society 1996, 143, (3), 1114-1123.

5. Cho, J.; Kim, Y. J.; Park, B., LiCoO2 Cathode Material That Does Not Show a Phase Transition from Hexagonal to Monoclinic Phase. Journal of the Electrochemical Society 2001, 148, (10).

6. Wang, H.; Jang, Y. I. I.; Huang, B.; Sadoway, D. R.; Chiang, Y. M., TEM Study of Electrochemical Cycling-Induced Damage and Disorder in LiCoO2 Cathodes for Rechargeable Lithium Batteries. Journal of the Electrochemical Society 1999, 146, (2), 473-480.

7. Choi, Y. M.; Pyun, S. I., Effects of intercalation-induced stress on lithium transport through porous LiCoO2 electrode. Solid State Ionics 1997, 99, (3-4), 173-183.

8. Goodenough, J. B., Design considerations. Solid State Ionics 1994, 69, (3-4), 184-198.

9. Nicholson, R. S.; Shain, I., Theory of stationary electrode polarography single scan and cyclic methods applied to reversible, irreversible, and kinetic systems. Analytical Chemistry 1964, 36, (4), 706-723.

10. Evans, D. H.; O'Connell, K. M.; Petersen, R. A.; Kelly, M. J., Cyclic voltammetry. Journal of chemical education 1983, 60, (4), 290-293.

11. Evans, D. H., Voltammetry: Doing chemistry with electrodes. Accounts of Chemical Research 1977, 10, (9), 313-319.

12. Brown, E. R.; Sandifer, J. R.; Rossiter, B. W.; Hamilton, J. F., Cyclic Voltammetry, AC Polarography, and Related Techniques. John Wiley & Sons: New York, Chichester, Brisbane, Toronto, Singapore, 1986; p 273-432.

13. Hulbert, M. H.; Shain, I., Rate-controlled adsorption of product in stationary electrode polarography. Analytical Chemistry 1970, 42, (2), 162-171.

14. Kissinger, P. T.; Heineman, W. R., Cyclic voltammetry. Journal of chemical education 1983, 60, (9), 702-706.

15. Kissinger, P. T.; Heineman, W. R., Large-Amplitude controlled-Potential Techiniques. In Laboratory Techniques in Electroanalytical Chemistry, Heineman,W.R.; Kissinger,P.T.: New York and Basel, 1984; pp 51-128.

16. Uchida, I.; Mohamedi, M.; Dokko, K.; Nishizawa, M.; Itoh, T.; Umeda, M., Recent investigations on thin films and single particles of transition metal oxides for lithium batteries. Journal of Power Sources 2001, 97-98, 518-524.

17. Uchida, I.; Sato, H., Preparation of binder-free, thin film LiCoO2 and its electrochemical responses in a propylene carbonate solution. Journal of the Electrochemical Society 1995, 142, (9).

18. Totir, D. A.; Cahan, B. D.; Scherson, D. A., Electrochemical characterization of lithiated transition metal oxide cathode particles in the absence of carbon, binders and other additives. Electrochimica Acta 1999, 45, (1), 161-166.

19. Pyun, S. I.; Shin, H. C., The kinetics of lithium transport through Li1-灌 CoO2 thin film electrode by theoretical analysis of current transient and cyclic voltammogram. Journal of Power Sources 2001, 97-98, 277-281.

20. Rho, Y. H.; Kanamura, K.; Umegaki, T., LiCoO2 and LiMn2O4 thin-film electrodes for rechargeable lithium batteries. Preparation using PVP sol-gel to produce excellent electrochemical properties. Journal of the Electrochemical Society 2003, 150, (1).

21. Padhi, A. K.; Nanjundaswamy, K. S.; Goodenough, J. B., Phospho-olivines as positive-electrode materials for rechargeable lithium batteries. Journal of the Electrochemical Society 1997, 144, (4), 1188-1194.

22. Yao, J.; Wang, G. X.; Ahn, J. H.; Liu, H. K.; Dou, S. X., Electrochemical studies of graphitized mesocarbon microbeads as an anode in lithium-ion cells. Journal of Power Sources 2003, 114, (2), 292-297.

23. Fu, Z. W.; Ma, J.; Qin, Q. Z., Nanostructured LiCoO2 and LiMn2O4 fibers fabricated by a high frequency electrospinning. Solid State Ionics 2005, 176, (17-18), 1635-1640.

24. Takahashi, M.; Tobishima, S. I.; Takei, K.; Sakurai, Y., Reaction behavior of LiFePO4 as a cathode material for rechargeable lithium batteries. Solid State Ionics 2002, 148, (3-4), 283-289.

25. Courtel, F. M.; Baranova, E. A.; Abu-Lebdeh, Y.; Davidson, I. J., In situ polyol-assisted synthesis of nano-SnO2/carbon composite materials as anodes for lithium-ion batteries. Journal of Power Sources 2010, 195, (8), 2355-2361.

26. Eskra, M. D.; Ralston, P.; Salkind, A.; Plivelich, R. F., Pulse power 350 V nickel-metal hydride battery power-D-005-00181. Journal of Power Sources 2006, 162, (2 SPEC. ISS.), 900-905.

27. Belt, J. R.; Ho, C. D.; Motloch, C. G.; Miller, T. J.; Duong, T. Q., A capacity and power fade study of Li-ion cells during life cycle testing. Journal of Power Sources 2003, 123, (2), 241-246.

28. Abraham, D. P.; Poppen, S. D.; Jansen, A. N.; Liu, J.; Dees, D. W., Application of a lithium-tin reference electrode to determine electrode contributions to impedance rise in high-power lithium-ion cells. Electrochimica Acta 2004, 49, (26), 4763-4775.

29. Abraham, D. P.; Reynolds, E. M.; Sammann, E.; Jansen, A. N.; Dees, D. W., Aging characteristics of high-power lithium-ion cells with LiNi 0.8Co0.15Al0.05O2 and Li 4/3Ti5/3O4 electrodes. Electrochimica Acta 2005, 51, (3), 502-510.

30. Holland, C. E.; Weidner, J. W.; Dougal, R. A.; White, R. E., Experimental characterization of hybrid power systems under pulse current loads. Journal of Power Sources 2002, 109, (1), 32-37.

31. Stewart, S. G.; Srinivasan, V.; Newman, J., Modeling the performance of lithium-ion batteries and capacitors during hybrid-electric-vehicle operation. Journal of the Electrochemical Society 2008, 155, (9).

32. Dees, D.; Gunen, E.; Abraham, D.; Jansen, A.; Prakash, J., Electrochemical modeling of lithium-ion positive electrodes during hybrid pulse power characterization tests. Journal of the Electrochemical Society 2008, 155, (8).

33. Smith, K.; Wang, C. Y., Solid-state diffusion limitations on pulse operation of a lithium ion cell for hybrid electric vehicles. Journal of Power Sources 2006, 161, (1), 628-639.

34. Doyle, M.; Fuller, T.; Newman, J., Modeling of galvanostatic charge and discharge of the lithium/ polymer/insertion cell. Journal of the Electrochemical Society 1993, 140, (6), 1526-1533.

35. Li, G.; Azuma, H.; Tohda, M., LiMnPO4 as the cathode for lithium batteries. Electrochem Solid State Letters 2002, 5, (6).

36. Xia, Y.; Yoshio, M., Spinel Cathode Materials for Lithium-Ion Batteries. In Lithium Batteries, 2003; pp 361-380.

37. Pasquali, M.; Passerini, S.; Pistoia, G., Trends in Cathode Materials for Rechargeable Batteries. In Lithium Batteries, 2003; pp 315-360.

38. Manthiram, A., Materials Aspects: An Overview. In Lithium Batteries, 2003; pp 3-41.

39. Ammundsen, B., Layered Manganese Oxides as Cathodes. In Lithium Batteries, 2003; pp 382-409.

40. Wang, Y.; Su, F.; Lee, J. Y.; Zhao, X. S., Crystalline carbon hollow spheres, crystalline carbon-SnO2 hollow spheres, and crystalline SnO2 hollow spheres: Synthesis and performance in reversible Li-ion storage. Chemistry of Materials 2006, 18, (5), 1347-1353.

41. Bazito, F. F. C.; Torresi, R. M., Cathodes for lithium ion batteries: The benefits of using nanostructured materials. Journal of the Brazilian Chemical Society 2006, 17, (4), 627-642.

42. Liu, H.; Wu, Y. P.; Rahm, E.; Holze, R.; Wu, H. Q., Cathode materials for lithium ion batteries prepared by sol-gel methods. J.Solid State Electrochem. 2004, 8, (7), 450-466.

43. Whittingham, M. S., Lithium batteries and cathode materials. Chemical reviews 2004, 104, (10), 4271-4301.

44. Huang, H.; Yin, S. C.; Nazar, L. F., Approaching theoretical capacity of LiFePO4 at room temperature at high rates. Electrochemical and Solid-State Letters 2001, 4, (10).

45. Yamada, A.; Hosoya, M.; Chung, S. C.; Kudo, Y.; Hinokuma, K.; Liu, K. Y.; Nishi, Y., Olivine-type cathodes: Achievements and problems. Selected Papers Presented at the 11th IMLB 2003, 119-121, 232-238.

46. Jugovic, D.; Uskokovic, D., A review of recent developments in the synthesis procedures of lithium iron phosphate powders. Journal of Power Sources 2009, 190, (2), 538-544.

47. Yang, M. R.; Teng, T. H.; Wu, S. H., LiFePO4/carbon cathode materials prepared by ultrasonic spray pyrolysis. Journal of Power Sources 2006, 159, (1 SPEC. ISS.), 307-311.

48. Beninati, S.; Damen, L.; Mastragostino, M., Fast sol-gel synthesis of LiFePO4/C for high power lithium-ion batteries for hybrid electric vehicle application. Journal of Power Sources 2009, 194, (2), 1094-1098.

49. Doherty, C. M.; Caruso, R. A.; Smarsly, B. M.; Drummond, C. J., Colloidal crystal templating to produce hierarchically porous LiFePO 4 electrode materials for high power lithium ion batteries. Chemistry of Materials 2009, 21, (13), 2895-2903.

50. Huang, Y.; Ren, H.; Peng, Z.; Zhou, Y., Synthesis of LiFePO4/carbon composite from nano-FePO4 by a novel stearic acid assisted rheological phase method. Electrochimica Acta 2009, 55, (1), 311-315.

51. Huang, Y.; Ren, H.; Yin, S.; Wang, Y.; Peng, Z.; Zhou, Y., Synthesis of LiFePO4/C composite with high-rate performance by starch sol assisted rheological phase method. Journal of Power Sources 2010, 195, (2), 610-613.

52. Yang, J.; Xu, J. J., Synthesis and characterization of carbon-coated lithium transition metal phosphates LiMPO4 (M=Fe, Mn, Co, Ni) prepared via a nonaqueous Sol-Gel route. J Electrochem Soc 2006, 153, (4).

53. Vadivel Murugan, A.; Muraliganth, T.; Manthiram, A., One-pot microwave-hydrothermal synthesis and characterization of carbon-coated LiMP O4 (M=Mn, Fe, and Co) Cathodes. J Electrochem Soc 2009, 156, (2).

54. Martha, S. K.; Markovsky, B.; Grinblat, J.; Gofer, Y.; Haik, O.; Zinigrad, E.; Aurbach, D.; Drezen, T.; Wang, D.; Deghenghi, G.; Exnar, I., LiMnPO4 as an advanced

cathode material for rechargeable lithium batteries. Journal of the Electrochemical Society 2009, 156, (7).

55. Andersson, A. S.; Thomas, J. O.; Kalska, B.; H 채 ggstr 철 m, L., Thermal stability of LiFePO4-based cathodes. Electrochemical and Solid-State Letters 2000, 3, (2), 66-68.

56. Andersson, A. S.; Thomas, J. O., The source of first-cycle capacity loss in LiFePO4. Journal of Power Sources 2001, 97-98, 498-502.

57. Salah, A. A.; Mauger, A.; Julien, C. M.; Gendron, F., Nano-sized impurity phases in relation to the mode of preparation of LiFePO4. Mater Sci Eng B Solid State Adv Technol 2006, 129, (1-3), 232-244.

58. Whittingham, M. S., Synthesis of Battery Materials. In Lithium Batteries, 2003; pp 85-109.

59. Chen, J.; Vacchio, M. J.; Wang, S.; Chernova, N.; Zavalij, P. Y.; Whittingham, M. S., The hydrothermal synthesis and characterization of olivines and related compounds for electrochemical applications. Solid State Ionics 2008, 178, (31-32), 1676-1693.

60. Okada, S.; Sawa, S.; Egashira, M.; Yamaki, J. I.; Tabuchi, M.; Kageyama, H.; Konishi, T.; Yoshino, A., Cathode properties of phospho-olivine LiMPO4 for lithium secondary batteries. Journal of Power Sources 2001, 97-98, 430-432.

61. Chen, J.; Whittingham, M. S., Hydrothermal synthesis of lithium iron phosphate. Electrochem.Commun. 2006, 8, (5), 855-858.

62. Shiraishi, K.; Dokko, K.; Kanamura, K., Formation of impurities on phospho-olivine LiFePO4 during hydrothermal synthesis. Journal of Power Sources 2005, 146, (1-2), 555-558.

63. Yan, H.; Sokolov, S.; Lytle, J. C.; Stein, A.; Zhang, F.; Smyrl, W. H., Colloidal-crystal-templated synthesis of ordered macroporous electrode materials for lithium secondary batteries. Journal of the Electrochemical Society 2003, 150, (8).

64. Choi, D.; Kumta, P. N., Surfactant based sol-gel approach to nanostructured LiFePO4 for high rate Li-ion batteries. Journal of Power Sources 2007, 163, (2), 1064-1069.

65. Kim, J. K.; Choi, J. W.; Chauhan, G. S.; Ahn, J. H.; Hwang, G. C.; Choi, J. B.; Ahn, H. J., Enhancement of electrochemical performance of lithium iron phosphate by controlled sol-gel synthesis. Electrochim Acta 2008, 53, (28), 8258-8264.

66. Xu, Z.; Xu, L.; Lai, Q.; Ji, X., A PEG assisted sol-gel synthesis of LiFePO4 as cathodic material for lithium ion cells. Mater Res Bull 2007, 42, (5), 883-891.

67. Arc?on, D.; Zorko, A.; Dominko, R.; Jaglic?ic, Z., A comparative study of magnetic properties of LiFePO4 and LiMnPO4. J Phys Condens Matter 2004, 16, (30), 5531-5548.

68. Dominko, R.; Bele, M.; Gaberscek, M.; Remskar, M.; Hanzel, D.; Pejovnik, S.; Jamnik, J., Impact of the carbon coating thickness on the electrochemical performance of LiFePO4/C composites. J Electrochem Soc 2005, 152, (3).

69. Dominko, R.; Bele, M.; Goupil, J. M.; Gaberscek, M.; Hanzel, D.; Arcon, I.; Jamnik, J., Wired porous cathode materials: A novel concept for synthesis of LiFePO4. Chemistry of Materials 2007, 19, (12), 2960-2969.

70. Hsu, K. F.; Tsay, S. Y.; Hwang, B. J., Synthesis and characterization of nano-sized LiFePO4 cathode materials prepared by a citric acid-based sol-gel route. J.Mater.Chem. 2004, 14, (17), 2690-2695.

71. Wang, G. X.; Needham, S.; Yao, J.; Wang, J. Z.; Liu, R. S.; Liu, H. K., A study on LiFePO4 and its doped derivatives as cathode materials for lithium-ion batteries. J Power Sources 2006, 159, (1 SPEC. ISS.), 282-286.

72. Arnold, G.; Garche, J.; Hemmer, R.; Strobele, S.; Vogler, C.; Wohlfahrt-Mehrens, M., Fine-particle lithium iron phosphate LiFePO4 synthesized by a new low-cost aqueous precipitation technique. Journal of Power Sources 2003, 119-121, 247-251.

73. Higuchi, M.; Katayama, K.; Azuma, Y.; Yukawa, M.; Suhara, M., Synthesis of LiFePO4 cathode material by microwave processing. Selected Papers Presented at the 11th IMLB 2003, 119-121, 258-261.

74. Sinha, N. N.; Munichandraiah, N., Single-shot preparation of crystalline nanoplate LiFePO4 by a simple polyol route. Journal of the Electrochemical Society 157, (7).

75. Cho, T. H.; Chung, H. T., Synthesis of olivine-type LiFePO4 by emulsion-drying method. Journal of Power Sources 2004, 133, (2), 272-276.

76. Palomares, V.; Goni, A.; Muro, I. G. d.; de Meatza, I.; Bengoechea, M.; Miguel, O.; Rojo, T., New freeze-drying method for LiFePO4 synthesis. Journal of Power Sources 2007, 171, (2), 879-885.

77. Kwon, S. J.; Kim, C. W.; Jeong, W. T.; Lee, K. S., Synthesis and electrochemical properties of olivine LiFePO4 as a cathode material prepared by mechanical alloying. Journal of Power Sources 2004, 137, (1), 93-99.

78. Lai, C.; Xu, Q.; Ge, H.; Zhou, G.; Xie, J., Improved electrochemical performance of LiFePO4/C for lithium-ion batteries with two kinds of carbon sources. Solid State Ionics 16: Proceedings of the 16th International Conference on Solid State Ionics (SSI-16), Part II 2008, 179, (27-32), 1736-1739.

79. Nien, Y. H.; Carey, J. R.; Chen, J. S., Physical and electrochemical properties of LiFePO4/C composite cathode prepared from various polymer-containing precursors. Journal of Power Sources 2009, 193, (2), 822-827.

80. Ravet, N.; Gauthier, M.; Zaghib, K.; Goodenough, J. B.; Mauger, A.; Gendron, F.; Julien, C. M., Mechanism of the Fe3+ reduction at low temperature for LiFePO4 synthesis from a polymeric additive. Chemistry of Materials 2007, 19, (10), 2595-2602.

81. Chung, S. Y.; Bloking, J. T.; Chiang, Y. M., Electronically conductive phospho-olivines as lithium storage electrodes. Nat.Mater. 2002, 1, (2), 123-128.

82. Yang, H.; Amiruddin, S.; Bang, H. J.; Sun, Y. K.; Prakash, J., A review of Li-ion cell chemistries and their potential use in hybrid electric vehicles. Journal of Industrial and Engineering Chemistry 2006, 12, (1), 12-38.

83. Nazar, L. F.; Crosnier, O., Anodes and Composite Anodes: An Overview. In Lithium Batteries, 2003; pp 112-143.

84. Besenhard, J. O.; Yang, J.; Winter, M., Will advanced lithium-alloy anodes have a chance in lithium-ion batteries? Journal of Power Sources 1997, 68, (1), 87-90.

85. Liu, H.; Long, D.; Liu, X.; Qiao, W.; Zhan, L.; Ling, L., Facile synthesis and superior anodic performance of ultrafine SnO2-containing nanocomposites. Electrochimica Acta 2009, 54, (24), 5782-5788.

86. Deng, D.; Kim, M. G.; Lee, J. Y.; Cho, J., Green energy storage materials: Nanostructured TiO2 and Sn-based anodes for lithium-ion batteries. Energy and Environmental Science 2009, 2, (8), 818-837.

87. Courtney, I. A.; McKinnon, W. R.; Dahn, J. R., On the aggregation of tin in SnO composite glasses caused by the reversible reaction with lithium. Journal of the Electrochemical Society 1999, 146, (1), 59-68.

88. Bruce, P. G.; Scrosati, B.; Tarascon, J. M., Nanomaterials for rechargeable lithium batteries. Angewandte Chemie - International Edition 2008, 47, (16), 2930-2946.

89. Gracia, L.; Beltran, A.; Andres, J., Characterization of the high-pressure structures and phase transformations in SnO₂. A density functional theory study. Journal of Physical Chemistry B 2007, 111, (23), 6479-6485.

90. Li, Z. J.; Qin, Z.; Zhou, Z. H.; Zhang, L. Y.; Zhang, Y. F., SnO2 nanowire arrays and electrical properties synthesized by fast heating a mixture of SnO2 and CNTs waste soot. Nanoscale Research Letters 2009, 4, (12), 1434-1438.

91. Courtney, I. A.; Dahn, J. R., Electrochemical and in situ X-ray diffraction studies of the reaction of lithium with tin oxide composites. Journal of the Electrochemical Society 1997, 144, (6), 2045-2052.

92. Noh, M.; Kwon, Y.; Lee, H.; Cho, J.; Kim, Y.; Kim, M. G., Amorphous carbon-coated tin anode material for lithium secondary battery. Chemistry of Materials 2005, 17, (8), 1926-1929.

93. Lee, K. T.; Jung, Y. S.; Oh, S. M., Synthesis of tin-encapsulated spherical hollow carbon for anode material in lithium secondary batteries. Journal of the American Chemical Society 2003, 125, (19), 5652-5653.

94. Wang, Y.; Lee, J. Y., Microwave-assisted synthesis of SnO2-graphite nanocomposites for Li-ion battery applications. Journal of Power Sources 2005, 144, (1), 220-225.

95. Kim, C.; Noh, M.; Choi, M.; Cho, J.; Park, B., Critical size of a nano SnO2 electrode for Li-secondary battery. Chemistry of Materials 2005, 17, (12), 3297-3301.

96. Deng, D.; Lee, J. Y., Hollow core-shell mesospheres of crystalline SnO2 nanoparticle aggregates for high capacity Li+ ion storage. Chemistry of Materials 2008, 20, (5), 1841-1846.

97. Wang, Y.; Lee, J. Y., Molten salt synthesis of tin oxide nanorods: Morphological and electrochemical features. Journal of Physical Chemistry B 2004, 108, (46), 17832-17837.

98. Lou, X. W.; Wang, Y.; Yuan, C.; Lee, J. Y.; Archer, L. A., Template-free synthesis of SnO2 hollow nanostructures with high lithium storage capacity. Advanced Materials 2006, 18, (17), 2325-2329.

Chapter 3

Template-Assisted Synthesis and Characterization of Olivine-based Materials for Li-ion Batteries

---

3.1 Introduction

$LiFePO_4$ (LFP) was first introduced as an alternative to $LiCoO_2$ by Padhi et al.[1] Due to the two-phase reaction of the olivine material during the intercalation of the lithium ion, the material showed high practical capacity (~140 mAh/g for LFP), constant potential discharge output[1] and safer operation at elevated temperatures (~60°C)[2]. Moreover, LFP is less costly and more environmentally friendly than $LiCoO_2$. The major drawback of the olivine materials is their low electronic conductivity. To overcome or improve this drawback, nano-

sized and carbon-coated olivine particles were suggested in order to shorten the solid diffusion paths for Li^+ and to achieve better electronic conductivity. As a result, many synthetic methods were developed and studied to obtain nano-sized and carbon-coated LFP.[3] To obtain the nano-sized material, researchers developed a microstructure template-assisted synthetic method that uses a microstructure as a template to synthesize a material with desired morphology. With this template-assisted method, particle size and morphology could be controlled by changing the structure of the template.

Template-assisted synthesis was adapted to synthesize three-dimensionally ordered macroporous (3DOM) materials that consisted of highly ordered spherical voids surrounded by a desired material as a solid wall (in this experiment, $LiMPO_4$, where M = Fe, Mn, Ni or Co). The structure consisted of a nano- to micro-sized wall whose thickness depended on the size and shape of the colloidal template, where the template is a polymer colloids assembled into desired structure. To synthesize a 3DOM structure, 300- to 500-nm diameters of colloidal particles (such as silica, polystyrene, poly methyl methacrylate or a mix of other polymers) were used as a template. 3DOM materials are being used in a wide range of applications such as in biosensors[4-6], photonics[7-9], and nanofabrications.[10] The materials for the colloidal templates were chosen according to the hydrophobicity between the precursor solutions and the templates. For this experiment, polystyrene (PS) colloids were used for the interest of PS carbon coating onto 3DOM LFP.

In this work, 3DOM LFP was produced by means of organic template-assisted synthesis. The organic template not only controlled the morphology, but also served as a carbon source, resulting in the formation of carbon-coated LFP. Recently, Doherty et al. (2009)[11] synthesized 3DOM LFP using a poly methyl methacrylate (PMMA) colloidal

template. The use of PMMA colloidal templates was necessary to infiltrate the concentrated LFP precursor solution due to the hydrophobicity of the template and the solution. However, improvements to LFP performance in Li-ion batteries can be made with different carbon sources. Different carbon sources were studied by others to improve electronic conductivity.[12, 13] Nien et al. (2009) studied carbon sources from different polymers and found that PS as a carbon source resulted in the highest capacity for LFP. However, PS as a colloidal template is too hydrophobic to immerse into the water-based LFP solution. For the first time, Brij 78 (Aldrich) was used in this experiment to change the hydrophobicity. Brij 78 contains a long hydrophobic and hydrophilic chain, as shown in Figure 3.1. Infiltration of Brij 78 into the PS template changes the hydrophobicity from hydrophobic to hydrophilic. Figure 3.2 is a detailed schematic that compares the procedure used to synthesize 3DOM material with and without Brij 78. The solid arrow, in Figure 3.2, shows the procedure using Brij 78, where the 3DOM material is synthesized by changing the hydrophobicity of the PS spheres. The dashed arrow shows the procedure without Brij 78, where the infiltrated solution coats only the surface of the PS template due to the high hydrophobicity.

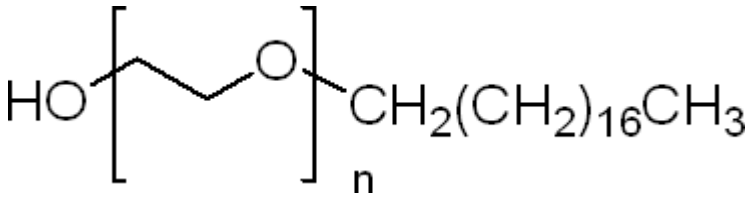

Figure 3.1 Chemical structure of Brij 78 used to change the hydrophobicity of PS colloidals

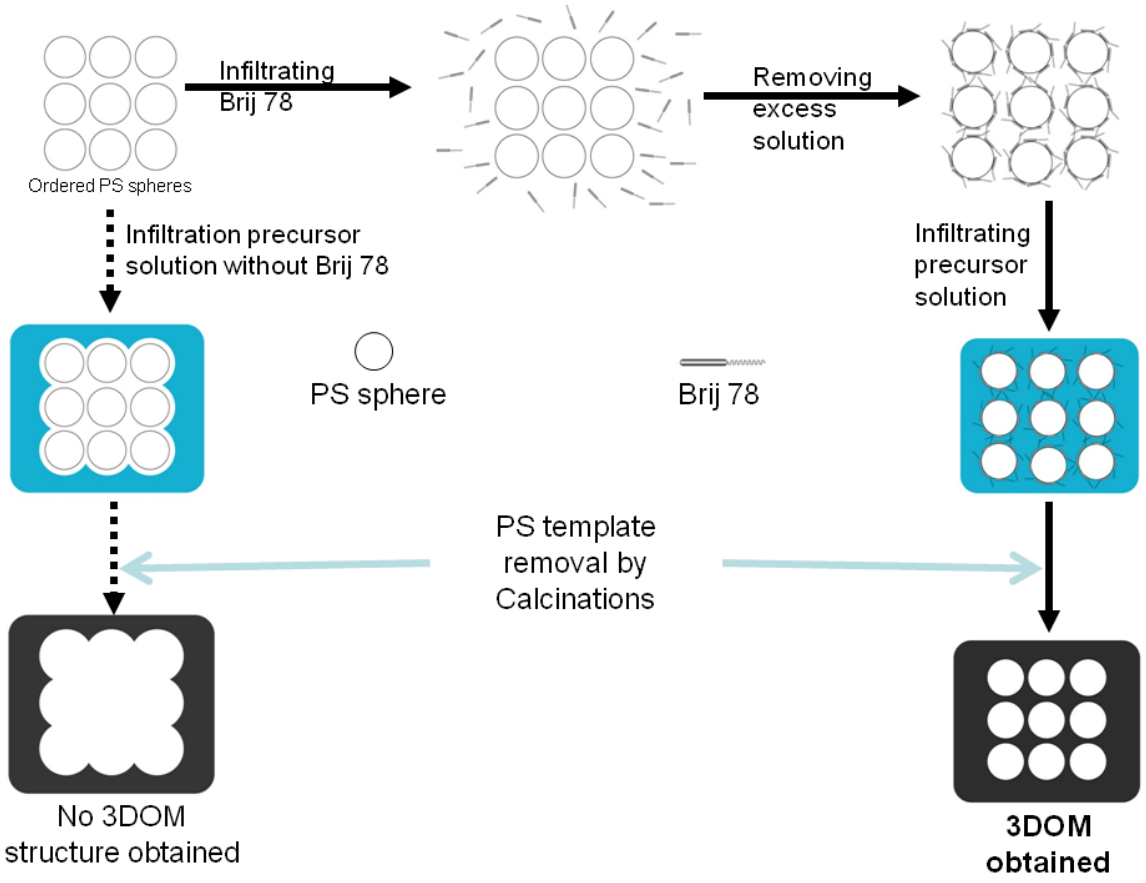

Figure 3.2 Schematic of the experimental procedure with and without Brij 78

The objective of this work was to use the PS colloidal template to obtain 3DOM high-performance olivine materials for Li-ion batteries. Brij 78 was used for the first time to change the hydrophobicity of the template. Using Brij 78, flexible choice of organic template can be tested as a carbon source to synthesize LFP.

3.2 EXPERIMENTAL

3.2.1 Synthesis of polystyrene spheres (PS) colloidal template

PS colloids were synthesized by emulsion polymerization, as described by Holland et al. (1999).[14] The styrene solution was obtained from Sigma-Aldrich (≥99% Reagentpuls), and prior to the polymerization of styrene, it was deaerated from oxygen (Nitrogen gas was bubbled through the solution while stirring on a magnetic plate). Then, 50 mL of styrene was mixed with 425 mL of de-ionized water, which had also been deaerated with the nitrogen gas. The temperature of the mixture was increased to 70°C. To initialize the polymerization, 25 mL of 0.1M $K_2S_2O_8$ (Sigma-Aldrich, 99%) solution was added to the styrene and water mixture. The $K_2S_2O_8$ solution was obtained by adding 0.667 g of $K_2S_2O_8$ to 25 mL de-ionized water and deaerated with nitrogen. The styrene solution was kept at 70°C and allowed to react under nitrogen for 24 hours. The synthesized PS colloids were washed with ethanol (Commercial Alcohols Inc., 95%) and centrifuged at 10000 rpm for 1 hr to obtain the ordered organic template, as shown in Figure 3.3, Step 1. The resulting template was dried in open atmosphere prior to the infiltration of LFP.

3.2.2 Synthesis of LFP

To infiltrate the hydrophilic LFP precursor solution, the hydrophobicity of the PS template was changed with Brij 78, as shown in Figure 3.3, Step 2. First, 0.01 g/mL of Brij

78 (Sigma-Aldrich) solution was prepared by adding 0.3 g of Brij 78 to 30 mL of ethanol. The PS template was immersed in the Brij 78 solution for five minutes to make sure the Brij is infiltrated into the template. The excess solution was removed by way of vacuum filtration, and the template was transferred to an alumina boat for further infiltration of the olivine-based precursor solution. The olivine-based precursor solution was prepared by mixing $LiNO_3$, H_3PO_4 (BDH Inc, 85%), and metal chloride, $FeCl_2$ $4H_2O$ (Alfa Aesar, 98%), $MnCl_2$ $4H_2O$ (BDH Inc, 98%), or $NiCl_2$ $6H_2O$ (Alfa Aesar, 99.95%) in distilled water. The precursor solution was prepared to yield 1 g of the olivine-based material. Metal chloride was fully dissolved in 1 g of water, and H_3PO_4 and $LiNO_3$ were added and mixed until the salts were fully dissolved. A few more drops were added during mixing to fully dissolve all the metal precursors. The precursor solution of the olivine-based material was infiltrated in the template. A pipette was used to slowly coat the template with the solution, as shown in Figure 3.3, Step 3. The infiltrated template was allowed to dry overnight. Then, the dry organic template was sintered under argon (Linde Canada, 99.999%). Calcinations were performed in two stages under argon: once at 260^{o}C for three hours to remove the PS template from the olivine-based materials, and again at 700^{o}C for three hours to obtain the olivine-based materials with a carbon coat. To prevent the volatile decomposition of the PS template, a slow temperature rate of 2°C/min was used.

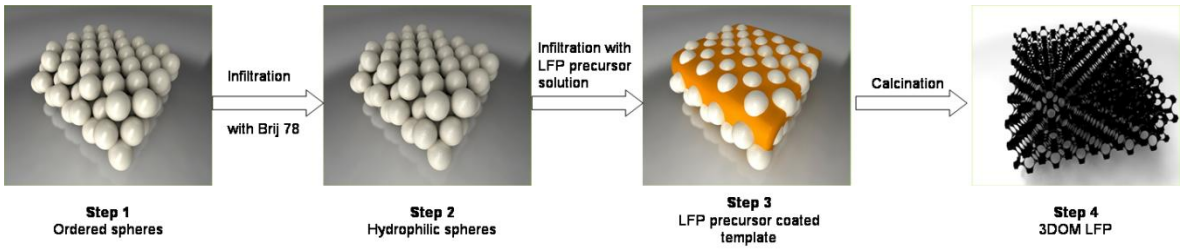

Figure 3.3 General synthesis of 3DOM material: Step 1: Ordering organic colloids; Step 2: Rendering hydrophobicity with Brij 78; Step 3: Immersion with precursor solution, and Step 4: Calcination to produce 3DOM material

3.2.3 Physicochemical characterization of PS and $LiFePO_4$

To ensure the presence of the structural order of PS colloidal and 3DOM LFP, scanning electron microscope (SEM) micrographs were captured using a JSM-840A JEOL instrument. X-ray diffraction (XRD) was performed to verify the purity. XRD patterns were obtained using a Cu Kα source with 35kV and 45mA power and then, recoded between 15° and 85° in 2θ angle, with a step size of 0.03 and 1s per step (Bruker D8 diffractormeter). TGA analyses were performed in order to quantify the amount of carbon in the synthesized olivine materials. TGA was set to scan the temperature from room temperature (~25°C) to 800°C with 10°C/min under oxygen atmosphere.

3.2.4 Testing of Li-ion batteries with synthesized LFP

The active materials synthesized were mixed using mortar and pestle with 5 wt% of carbon super S (Timcal), 5 wt% of carbon graphite (Timcal) and 15 wt% of polyvinylidene fluoride (PVDF, Kynar Flex 2800 dissolved in N-Methyl-pyrrolidinone from Aldrich). Then, the mixed active materials were spread onto the aluminum foil current collector using an automated doctor-blade. They were dried overnight at 85°C in a vacuum oven to remove all of the NMP solution. The obtained aluminum electrodes with active materials were punched and assembled to a 2325-type coin cell using 1M $LiPF_6$ in ethylene carbonate/dimethyl carbonate (1:1, v/v) electrolyte wetted onto a double layer of microporous propylene separators (Celgard 2500, 30μm think, 2.1mm diameter). Assembling was done under an argon-filled glove box to prevent the oxidation of electrolytes and lithium metal. Figure 3.4 illustrates the parts and schematics of the assembled battery. The cell was tested using a multichannel galvanostat from Arbin Cycler. The capacity was tested at different C-rates of charge/discharge: C/12, C/6, C, 2C and 5C. Five full cycles of charge/discharge were measured for each C-rate.

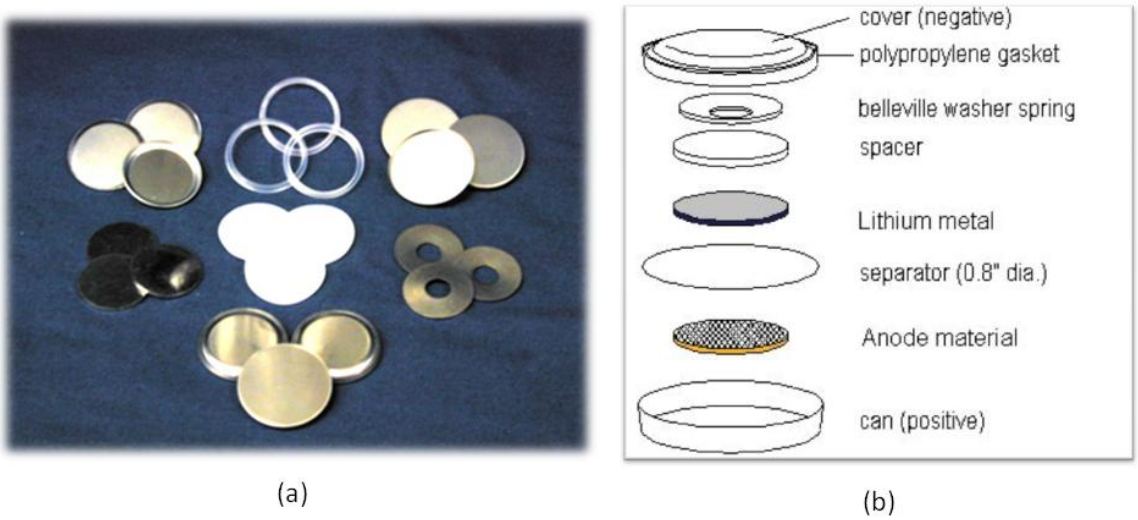

Figure 3.4 2325-type coil cell (a) Image of battery parts (b) Schematic of the battery assembly

3.3 Results and discussion

To ensure the correct order and morphology of PS colloids, SEM micrographs of the dry PS template were taken. Figure 3.5 shows a typical SEM micrograph of the synthesized PS colloids. From the SEM micrographs, the average sphere diameters were found to be between 300 and 500 nm. As seen from the figure, the spheres are closely packed and three-dimensionally ordered.

Because the metal precursors were dissolved in a small amount of water (1g), the solution had difficulty to infiltrate into the hydrophobic PS template. As such, Brij 78 was used to change the hydrophobicity of the PS template. Brij 78 consists of long hydrophilic

and hydrophobic chains. The hydrophobic chains bound with the PS colloids and the hydrophilic chains helped infiltrate the water-based precursor solution.

The dry organic template was immersed in a solution of Brij 78 in ethanol. The solid organic template broke into millimetre-sized particles after immersion in the ethanol and Brij 78 solution. The millimetre-sized templates in the Brij solution produced fine bubbles due to the air trapped between the template's void. After a couple minutes, the fine bubbles could no longer be observed, which signalled the end of the infiltration. To complete the infiltration of the Brij solution, the template had left few more minutes. The total infiltration of the Brji solution was approximately 5 minutes. The excess Brij solution was removed using vacuum filtration. The filtered template was coated with the precursor solution to infiltrate the precursors into the PS template.

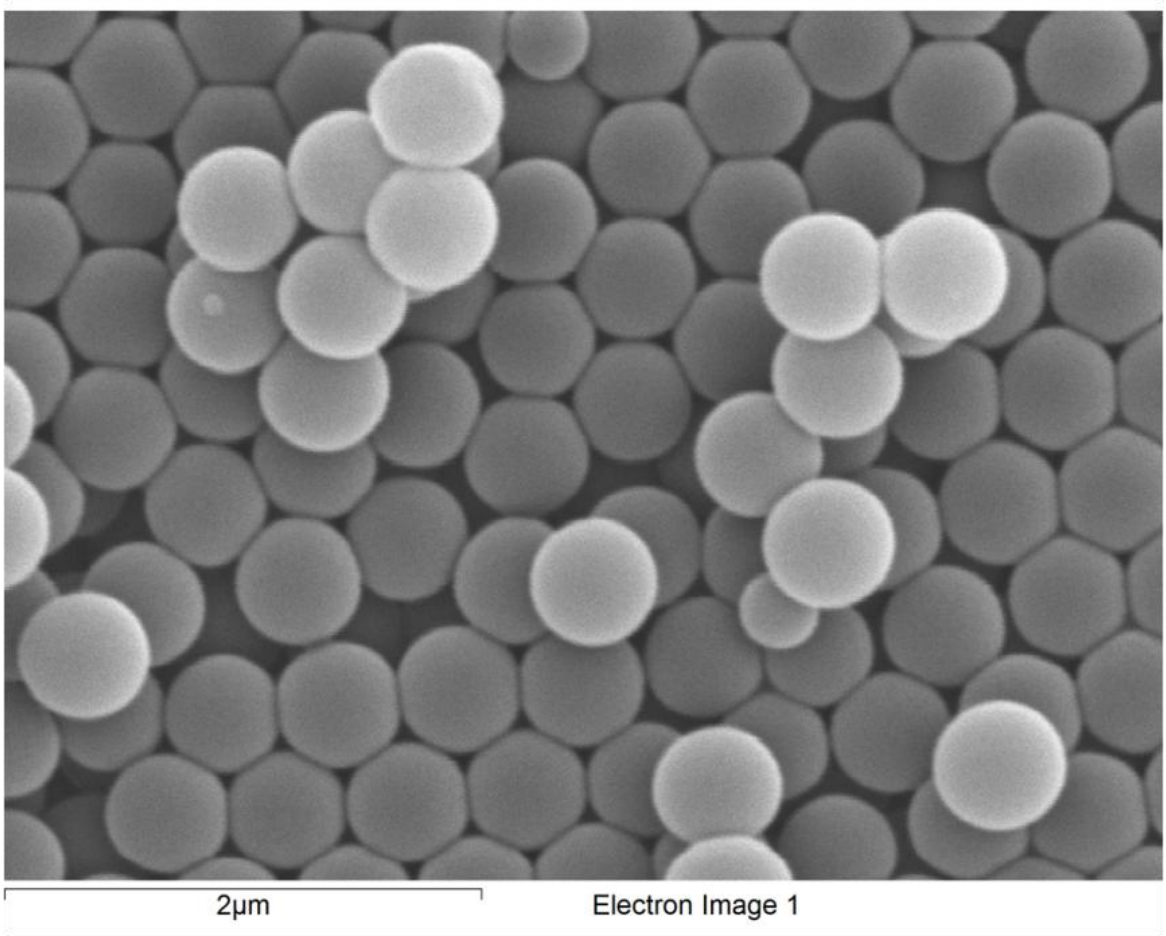

Figure 3.5 SEM micrograph of the synthesized polystyrene (PS) spheres

When the template was immersed in the precursor solution, two wetted templates were prepared to compare the infiltration speed: ethanol solutions with and without the Brij 78. Without Brij, the infiltration of the precursor solution to the PS colloids template was unsufficient as the solution formed droplet at the surface without infiltrating even after a day. However, when Brij 78 was used, the infiltration time was short and the precursor solution was homogenously infiltrated through the PS colloidal template. Reproduction of the 3DOM LFP was attempted and same results was achieved. Similar attempts have been made for

other applications.[15, 16] In this work, the application was adapted to improve the immersion of the water-based precursor solution in the highly hydrophobic organic template in order to synthesize 3DOM olivine materials. The immersion was also tested on PMMA colloidal template and similar results were obtained. The same experiment was performed using PMMA colloidal template, however, severe impurity was observed when the LFP was synthesized after the calcinations.

It was necessary to perform the calcinations at a slow heating rate (2°C/min) in order to remove the PS spheres and maintain the structure. The slow heating rate prevented the volatile decomposition of PS colloids. To give enough time to condense the inorganic material and remove the PS colloids template, two step calcination was performed at different temperatures. The first step calcination occurred at 260°C and lasted three hours in order to remove the PS and condense the material. The second step calcination occurred at 700°C for another three hours in order to synthesize and crystallize the LFP. At the end of the calcinations the synthesized materials were cooled down naturally to the room temperature. The calcinations were performed under argon to prevent the oxidization of Fe^{2+} to Fe^{3+}, and also to carbon coat the materials. Figure 3.5 shows the macroporous structure of the LFP synthesized with a Brij 78-coated PS template. It is possible to see that the ordered macroporous structure was maintained during the calcinations. The thickness of the walls is approximately 100 nm. In some areas, there are ruptures in the structure that were caused by the volatile decomposition of the PS and Brij template. The procedure was repeated to ensure that the synthesis of 3DOM LFP could be reproduced and that the same results could be obtained from SEM and XRD.

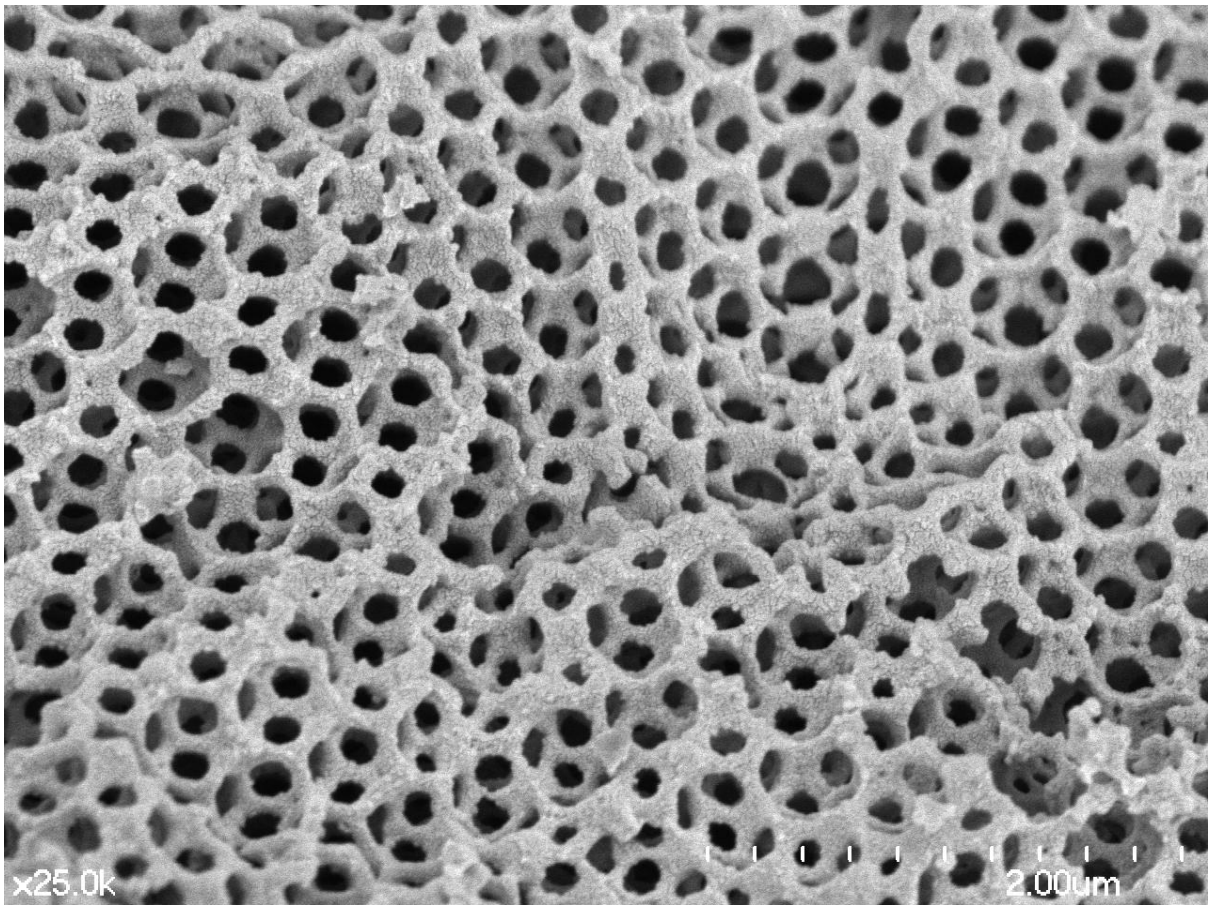

Figure 3.6 SEM micrograph of the synthesized 3DOM LFP – Wall thickness of 100 nm of was observed as well as some minor ruptures of the structure in the bottom right corner of the image.

Thermal gravimetric analysis (TGA), commonly used for evaluating the oxidized state of LFP, was used to obtain the carbon amount.[17] TGA analysis was performed under air to oxidize and decompose all the carbon residue in the material. At high temperatures and pressure, Fe (II) in LFP oxidized to Fe (III), as shown in Equation 3.1. The reaction was confirmed by Belharouak et al. (2005)[17]. As a result of the oxidization, weight gain of 5%

was observed due to the oxiygen reacting to the Fe from LFP. The same calculation can be made using the TGA results. When the oxidation at high temperature has the reaction as shown in Equation 3.1, using the initial and final weight carbon contents in the materials can be obtained.

Figure 3.7 shows the TGA results of LFP. Based on the results, the commercial LFP, otained from Phostech Lithium Inc., had 3% weight gain, suggesting 1% of carbon in the active material, when 5% weight gain is assumed to be the result of LFP oxidation. The synthesized LFP showed 19% weight loss, that is, 23% of the carbon contained in the LFP.

$$LiFePO_4 + \tfrac{1}{4}O_2 \rightarrow \tfrac{1}{3}Li_3Fe_2(PO_4)_3 + \tfrac{1}{6}Fe_2O_3 \qquad 3.1$$

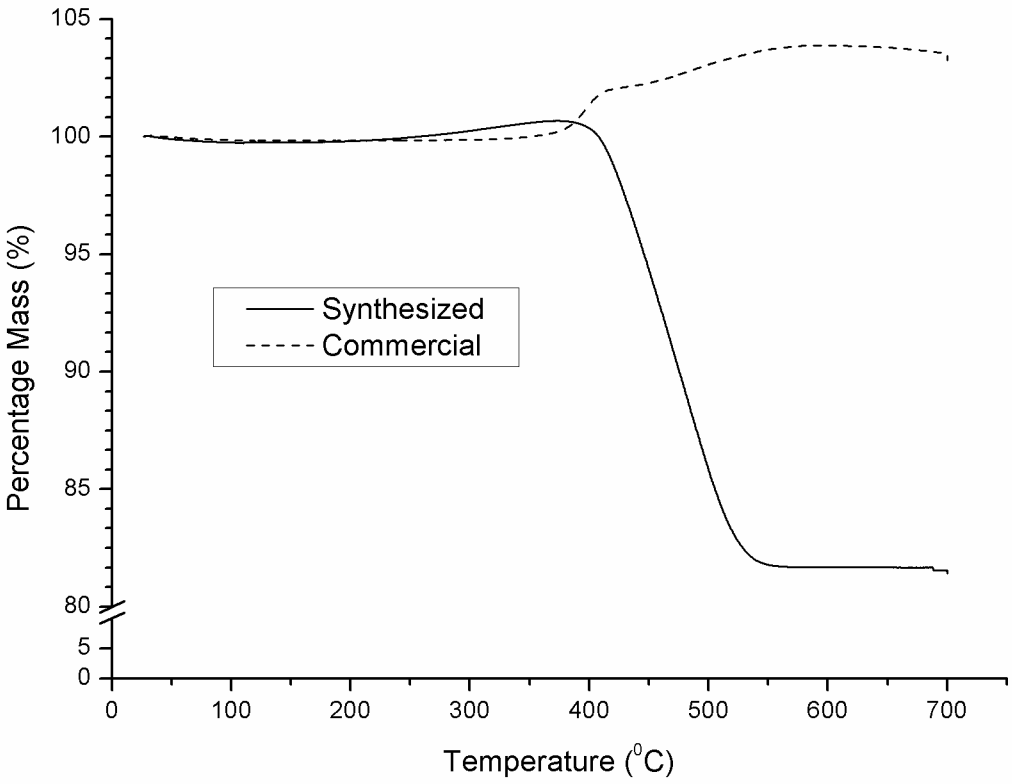

Figure 3.7 TGA analysis of LFP under oxygen - The final weight of the samples was subtracted from 105% to obtain amount of carbon in LFP.

To ensure the purity and crystal size of LFP, XRD analysis was conducted. The results are shown in Figure 3.8. The solid red line represents a simulated result obtained using Topas (commercial program from Bruker to simulate the XRD pattern), while the black dots are the experimental results. The differences between the simulated and experimental results are shown at the zero axes. The reference peaks for LFP (ISCD 161479) are shown as black lines right above the x-axis. The reference peaks are used to simulate the fit to evaluate the lattice parameter and crystal size using TOPAS.

These XRD results show that there is no evidence of impurity found in the materials. From the simulated result using Topas the space group of LFP was identified as *Pmna* and the lattice parameters are determined, as listed in Table 3.1. The parameter and crystal structure results agree with the results described in earlier literature.[1, 3, 11, 17]

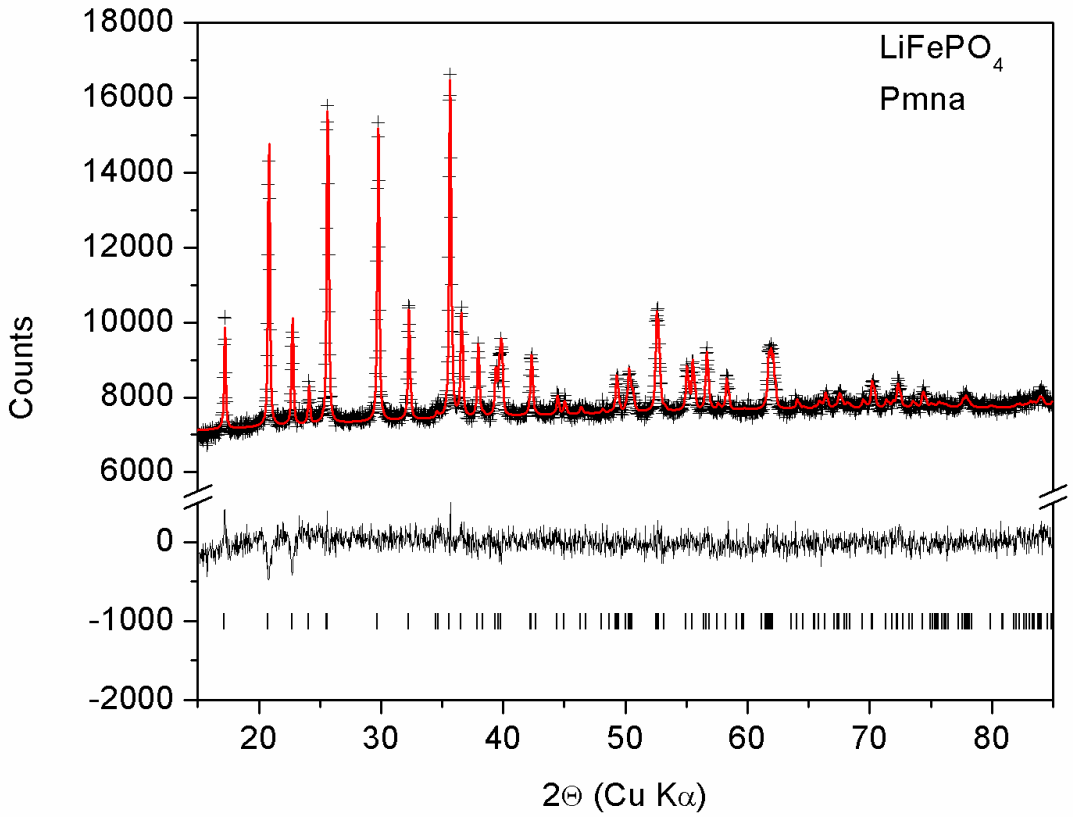

Figure 3.8 XRD pattern of the synthesized LFP - The red line represents the simulated results to find the lattice parameters; the black line represents the difference between the simulated and XRD results; the black line at -1000 shows the peaks of LFP references used to simulate the Topas results.

Table 3.1 Lattice parameters of synthesized and reference LFP

Lattice parameters	Synthesized	Reference[18]
a (Å)	10.3331 ± 0.0005	10.33
b (Å)	6.0106 ± 0.0003	6.01
c (Å)	4.6953 ± 0.0003	4.70
Crystal size (nm)	78.1 ± 0.2	N/A

Synthesized LFP was prepared for use as the cathode electrode as explained in the experimental section. It was tested in a coin cell with lithium metal for the anode electrode. Figure 3.9 shows the first charge/discharge curve of LFP and flat discharge curve was observed. A discharge capacity of 158 mAh/g (close to the theoretical capacity of 170 mAh/g) was obtained. As previously mentioned[1], due to the two-phase reaction of $LiFePO_4$/ $FePO_4$, the potential output is a plateau.

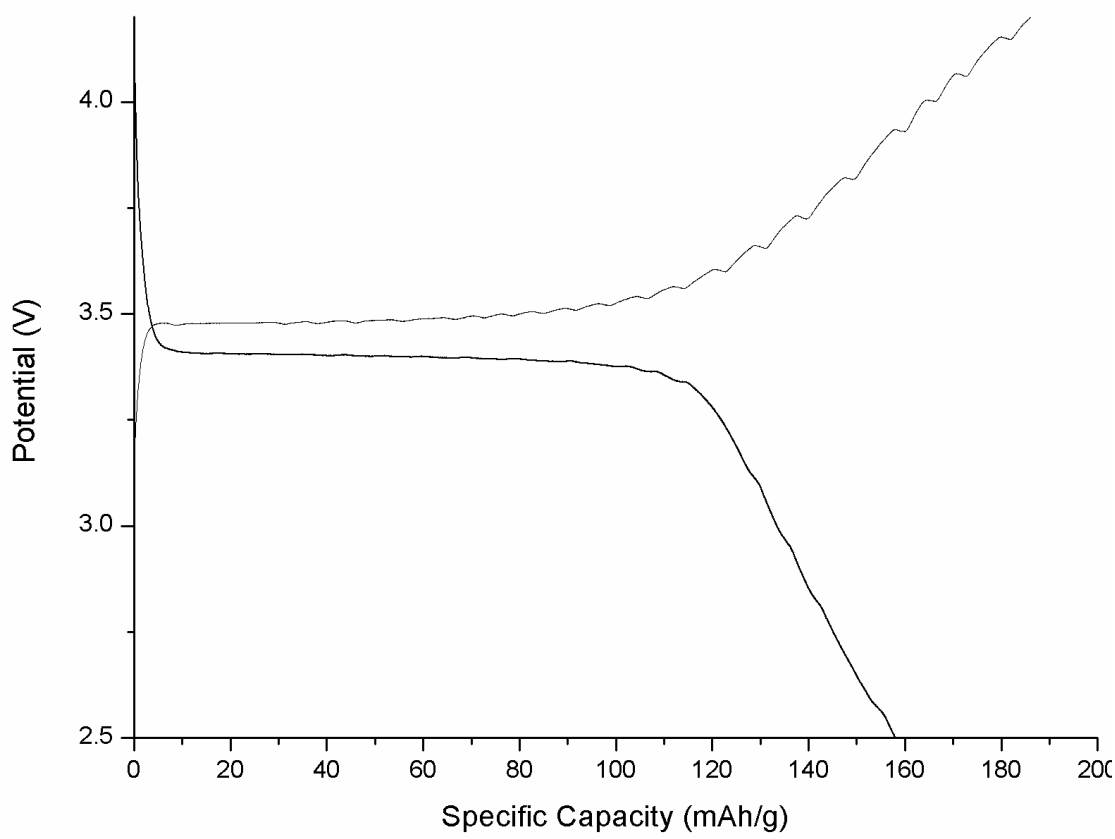

Figure 3.9 Charge/discharge curve of LFP half-cell battery - during first cycle at C/12

LFP was also tested at different C-rates, as described in Chapter 2.2. The results are shown in Figure 3.10. Five cycles were repeated at each C-rate: C/12, C/6, C, 2C, 5C, and back to C/12 again to check for any capacity fade after high C-rate cycling. During the first 10 cycles (at C/12 and C/6), capacity fade of 6 % was observed. The capacity fade was calculated using the difference of the capacity at the first and fifth cycle of each C-rate. It might have been the cause of the cathode-electrolyte interface (CEI).[19] The formation of the CEI causes the decomposition of the electrolytes, which might cause the chemical barrier at the interface of the active material and the electrolyte that results an capacity loss. After the

tenth cycle, the capacity was stabilized and also recovered at low C-rate (C/12), with a 12% of capacity fade that was calculated using the first capacity obtained (158 mAh/g). Figure 3.11 shows the specific capacity related to the C-rate. The x-axis for currents is in logarithm scale. The obtained specific capacity related to C-rate shows a logarithmic relationship with very good R^2 values (0.9766).

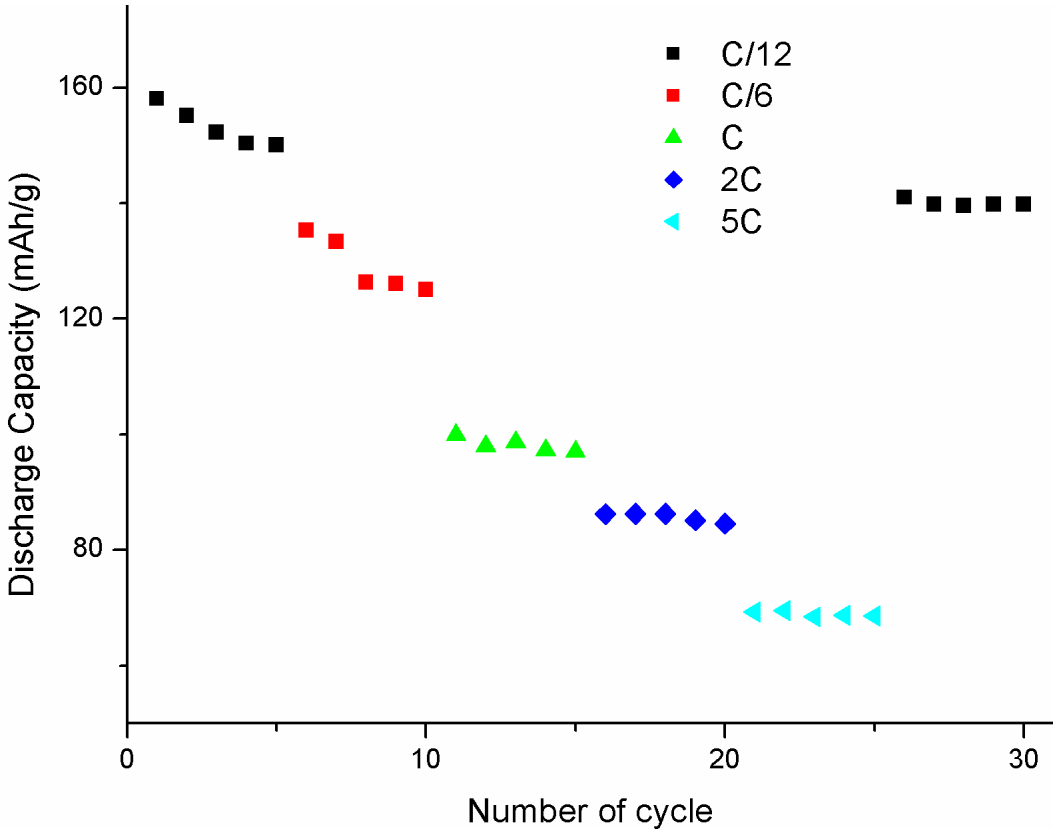

Figure 3.10 Specific capacity of LFP at different C-rates

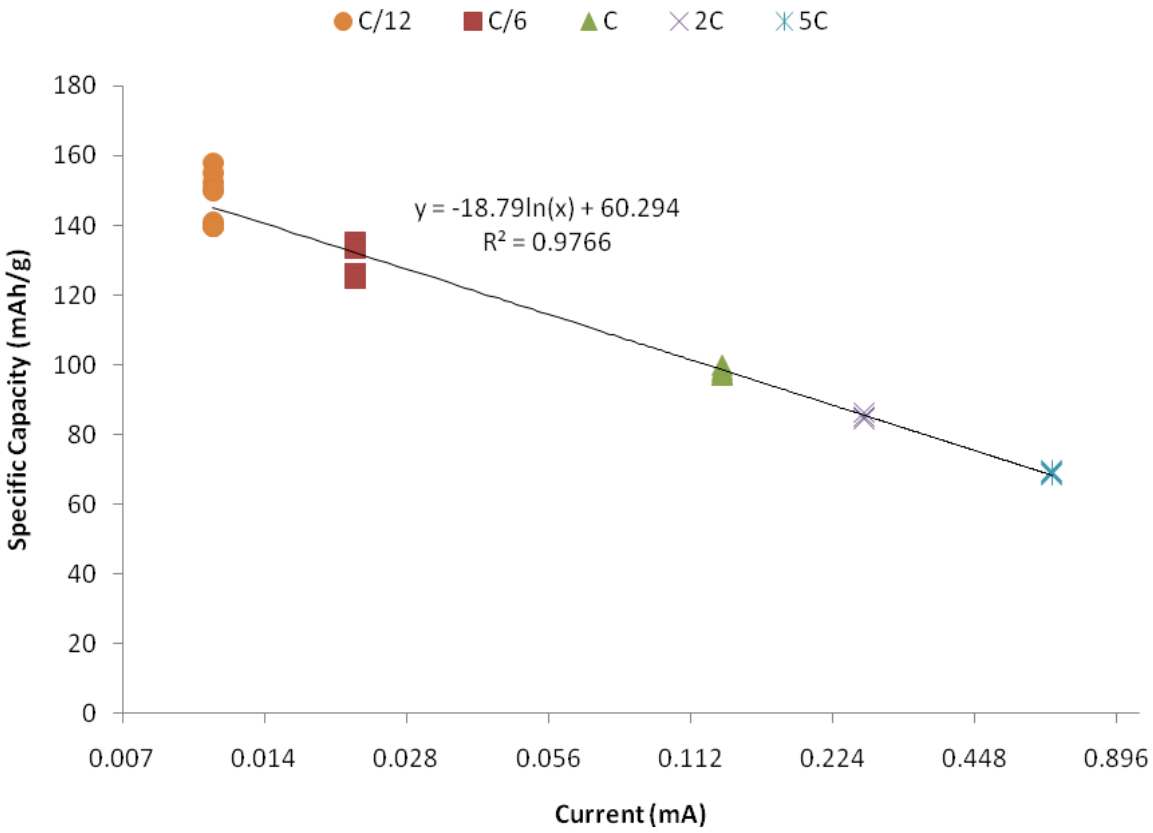

Figure 3.11 Discharge capacity at different C-rates; x-axis (current) in log scale

The first discharge curves for each C-rate are shown in Figure 3.12. As the C-rate increases, the flat plateau disappears due to diffusion polarization. Due to the highly ordered porosity of the synthesized LFP, the diffusion polarization was expected to be minimized[11]; however, such a trend was not observed. The flat plateau of the LFP discharge curve was observed with this synthesis up to 1C rate. As a result of diffusion limitation of the lithium ion, the electrodes were charged faster then the intercalation of the Li^+ into the LFP and voltage start to decrease faster compared to the lower C-rate (C/12. C/6, and C), as so the flat plateau started to fade at high C-rates (2C to 5C).

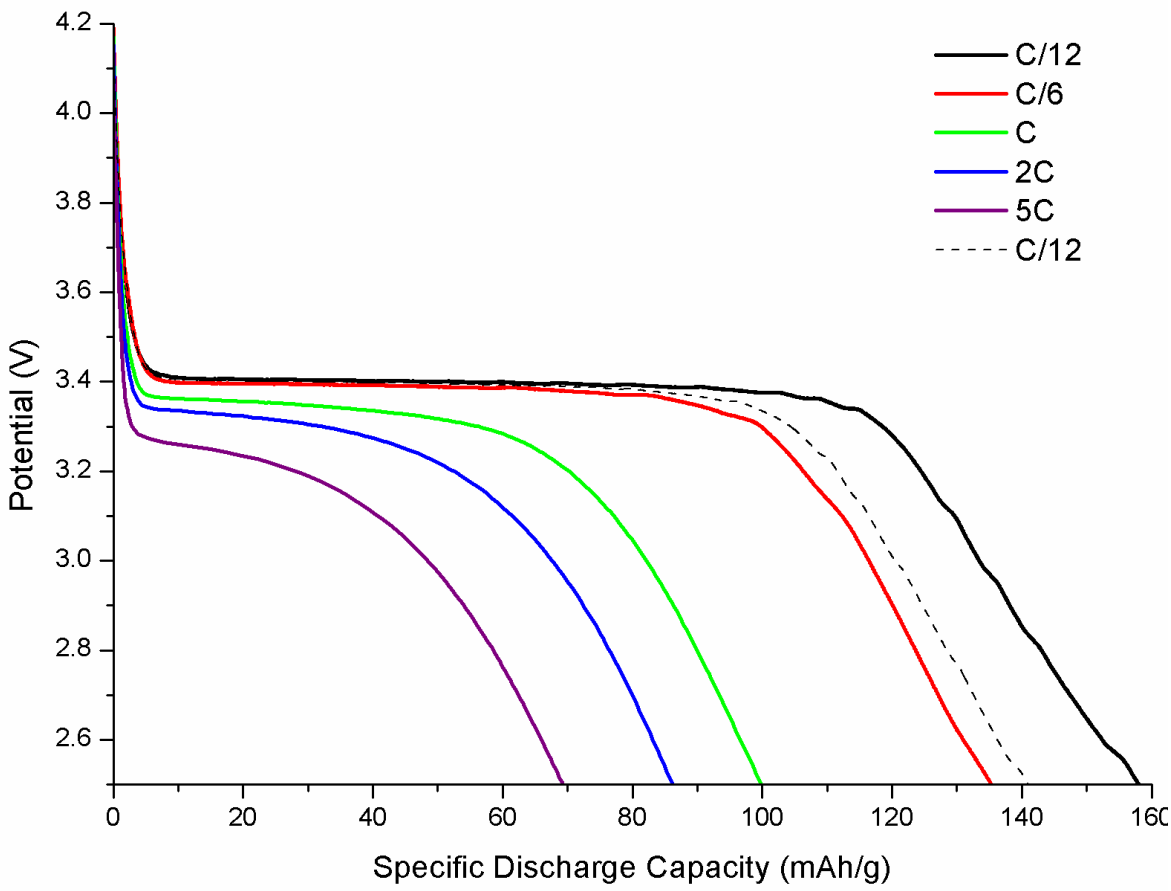

Figure 3.12 Discharge curve at different C-rates

3.4 Conclusions

From this work, pure nano-structured 3DOM LFP were successfully synthesized by means of a new organic template-assisted synthesis. The organic template consisted of PS colloids that were synthesized by emulsion polymerization in a water base. The diameters of the PS colloids measured between 300 and 500 nm. The PS colloids were ordered successfully by centrifugation. The hydrophobicity was changed with Brij 78 to improve the infiltration time and shorten the total process time of LFP synthesis. Calcination of the PS

colloidal template and crystallization of 3DOM LFP was achieved under argon to prevent the Fe^{2+} oxidation and to carbon coat LFP. SEM micrographs and XRD results confirmed the crystal structure and morphology of the 3DOM LFP. The wall thickness measured 100 nm and the porous diameter measured between 300 and 500 nm from the SEM micrograph. The resulting LFP had pure crystal structure, a Pmna space group and a 78.1-nm crystal size. The resulting LFP cathode material had a promising high capacity (158mAh/g), which was close to the theoretical capacity (170 mAh/g). The synthesized LFP was able to charge/discharge at high C-rates (2C to 5C) and to recover capacity to the initial capacity with 12% of capacity fade at lower C-rates (C/12).

3.5 References:

1. Padhi, A. K.; Nanjundaswamy, K. S.; Goodenough, J. B., Phospho-olivines as positive-electrode materials for rechargeable lithium batteries. *Journal of the Electrochemical Society* **1997,** 144, (4), 1188-1194.

2. Andersson, A. S.; Thomas, J. O.; Kalska, B.; Haggstrom, L., Thermal stability of $LiFePO_4$-based cathodes. *Electrochemical and Solid-State Letters* **2000,** 3, (2), 66-68.

3. Jugovic, D.; Uskokovic, D., A review of recent developments in the synthesis procedures of lithium iron phosphate powders. *Journal of Power Sources* **2009,** 190, (2), 538-544.

4. Weissman, J. M.; Sunkara, H. B.; Tse, A. S.; Asher, S. A., Thermally switchable periodicities and diffraction from mesoscopically ordered materials. *Science* **1996,** 274, (5289), 959-960.

5. Reese, C. E.; Baltusavich, M. E.; Keim, J. P.; Asher, S. A., Development of an intelligent polymerized crystalline colloidal array colorimetric reagent. *Analytical Chemistry* **2001,** 73, (21), 5038-5042.

6. Cassagneau, T.; Caruso, F., Inverse opals for optical affinity biosensing. *Advanced Materials* **2002,** 14, (22), 1629-1633.

7. Cheng, W.; Wang, J.; Jonas, U.; Fytas, G.; Stefanou, N., Observation and tuning of hypersonic bandgaps in colloidal crystals. *Nature Materials* **2006,** 5, (10), 830-836.

8. Joannopoulos, J. D.; Villeneuve, P. R.; Fan, S., Photonic crystals: Putting a new twist on light. *Nature* **1997,** 386, (6621), 143-149.

9. Yablonovitch, E., Photonic crystals: Semiconductors of light. *Scientific American* **2001,** 285, (6), 34-41.

10. Fischer, U. C.; Zingsheim, H. P., SUBMICROSCOPIC PATTERN REPLICATION WITH VISIBLE LIGHT. *Journal of vacuum science & technology* **1981,** 19, (4), 881-885.

11. Doherty, C. M.; Caruso, R. A.; Smarsly, B. M.; Drummond, C. J., Colloidal crystal templating to produce hierarchically porous $LiFePO_4$ electrode materials for high power lithium ion batteries. *Chemistry of Materials* **2009,** 21, (13), 2895-2903.

12. Dominko, R.; Bele, M.; Gaberscek, M.; Remskar, M.; Hanzel, D.; Pejovnik, S.; Jamnik, J., Impact of the carbon coating thickness on the electrochemical performance of $LiFePO_4$/C composites. *J Electrochem Soc* **2005,** 152, (3).

13. Nien, Y. H.; Carey, J. R.; Chen, J. S., Physical and electrochemical properties of LiFePO4/C composite cathode prepared from various polymer-containing precursors. *Journal of Power Sources* **2009,** 193, (2), 822-827.

14. Holland, B. T.; Blanford, C. F.; Do, T.; Stein, A., Synthesis of Highly Ordered, Three-Dimensional, Macroporous Structures of Amorphous or Crystalline Inorganic Oxides, Phosphates, and Hybrid Composites. *Chemistry of Materials* **1999,** 11, (3), 795-805.

15. Deng, X.; Hu, G.; Peng, Z.; Yang, Y.; Cao, Y.; Du, K., Preparation and electrochemical characteristics of $Co_3(PO_4)_2$-coated $LiNi_{0.8}Co_{0.2}O_2$ by solid-state reaction at room temperature. *Rare Met* **2008,** 27, (5), 502-506.

16. Wang, T.; Keddie, J. L., Design and fabrication of colloidal polymer nanocomposites. *Advances in Colloid and Interface Science* **2009,** 147-148, (C), 319-332.

17. Belharouak, I.; Johnson, C.; Amine, K., Synthesis and electrochemical analysis of vapor-deposited carbon-coated LiFePO4. *Electrochemistry Communications* **2005,** 7, (10), 983-988.

18. Song, M. S.; Kang, Y. M.; Kim, Y. I.; Park, K. S.; Kwon, H. S., Nature of insulating-phase transition and degradation of structure and electrochemical reactivity in an olivine-structured material, $LiFePO_4$. *Inorganic Chemistry* **2009,** 48, (17), 8271-8275.

19. Duncan, H.; Abu-Lebdeh, Y.; Davidson, I. J., Study of the cathode-electrolyte interface of $LiMn_{1.5}Ni_{0.5}O_4$ synthesized by a sol-gel method for li-ion batteries. *Journal of the Electrochemical Society* 157, (4).

Chapter 4

Synthesis and Characterization of Macroporous Tin Oxide as an Anode for Li-ion Batteries

---

4.1 Introduction

Graphite has been the most popular material used for anodes in Li-ion batteries due to the low cost, long life cycle and negligible volume change during battery charging[1]. However, due to its limited theoretical capacity (~372 Ah/kg and 833 Ah/l) and slow lithium intercalation, other materials are being sought out. Among the anode materials being studied are metal alloys such as Al, Si, Ge, Sn, Pb, Sb and Bi.[1] These metal alloys are promising anode materials due to their lithium uptake at a low potential and three to ten fold higher

theoretical capacities to graphite. However, the major problem with these materials is the extremely high volume expansion (~250%) upon the insertion of lithium. The repeated expansion and contraction during a battery's charge/discharge cycle causes mechanical cracks, pulverization and loss of electronic conductivity between the particles and the current collector. The result of all of this is an extremely poor life cycle of the materials.

To prevent pulverization during the charge/discharge cycle, Besenhard et al. (1997) suggested minimizing the particle size in multiphase alloy matrices[2] for metal alloys. Courtney et al.[3] studied tin oxide. They showed an irreversible reaction of SnO_2 to Sn that further formed an alloy with lithium. It resulted in networks of Li_2O layers in Sn. As a result, the network of Li_2O layers prevented the severe volume expansion and kept the Sn in nano-sized form. However, building up the lithium oxide networks could not prevent complete volume changes of Sn, leading to pulverization. Other alternatives have been introduced, such as coating Ni-Sn onto the Cu nano-rods[4], and spherically porous multi-deck cage SnO_2[5]. Other approaches include dispersion of SnO_2 onto the carbon materials[6], or carbon coating of SnO_2[7].

In this work, porous carbon-coated SnO_2 was synthesized by means of a hydrothermal reaction with polystyrene (PS) colloidal templates. This was followed by the calcining the obtained SnO_2/PS composite in order to decompose PS colloids and form a carbon coating on the SnO_2. The former step was important to prevent the pulverization of Sn. A colloidal template was used to synthesize nano-crystals for highly three-dimensionally ordered macroporous structures[8]. The 3DOM crystal synthesis has been used for a variety of applications in chemical and biochemical sensors[9-11], photonic band gap materials[12-14] and nanofabrication[15]. The 3DOM synthesis was adapted in this work to obtain ordered carbon-

coated porous material and to prevent significant volume change and Sn pulverization during battery charge/discharge. The use of the PS organic colloidal template, made it possible to create 3DOM SnO_2/C. However, there were several challenges. First, the tin precursor had to undergo oxidization reaction without destroying the PS colloids. Moreover, the organic template had to be calcined under non-oxygen atmosphere to obtain a carbon coat. Thus, a hydrothermal reaction was used to oxidize the tin precursor with PS colloidal and sintering of the SnO_2/PS composite at a high temperature of 600°C without oxygen was performed to obtain a carbon coat.

4.2 Experimental

4.2.1 Synthesis of tin oxide

Tin oxide was synthesized by means of a hydrothermal reaction. First, 0.356 g of $SnCl_2 2H_2O$ (Fisher, 98.4%) was dissolved in 50 mL of de-ionized water and 50 mL of ethanol. PS colloids were synthesized via emulsion polymerization, as described in Chapter 3. Then, 240 mg of PS colloids were added to the solution and mixed for one day using magnetic stirring to homogenize and disperse the PS colloids in the solution. The beaker containing the solution was covered with the parafilm to prevent the evaporation. The resulting solution had a milky colour due to the undissolved PS colloids in the solution. The solution was put into an autoclave reactor (Parr, Bomb No. 4744) for six hours at 120°C. After the synthesis, the autoclave reactor containing the solution was cooled to room

temperature. The resulting solution was centrifuged to separate the synthesized SnO_2 and to order the PS colloids to build the template. The precipitates were washed three times with ethanol (95 wt%), and then calcinated under argon at 600°C for three hours at a slow heating rate of 2°C/min. The calcination was performed under argon to obtain carbon coating to the SnO_2.

4.2.2 Characterization of tin oxide

To ensure the nano-sized crystal and morphology of the synthesized SnO_2, XRD (using a Bruker D8 diffractometer and a Co Kα source) and an SEM (JSM-840A JEOL instrument) were used, respectively.

XRD patterns were collected from 15° to 85° 2θ angles with a step size of 0.03 and 1 s per step. 35 kV and 45 mA of power were used to obtain the XRD pattern. The synthesized SnO_2 was ground using mortar and pestle by hand, and prepared for XRD as it is. With the scanning results from XRD, Topas v4.2 (Bruker) was used to fit all the data points and evaluate the crystal size and the structure. To ensure the morphology of SnO_2 SEM micrographs were captured using a JSM-840A JEOL instrument. Thermal gravimetric analysis (TGA) was performed to quantify the amount of carbon using a TGA 2950 TA instrument. The synthesized SnO_2 was heated at a rate of 10°C/min up to 110°C for 30 min to remove moisture contained in the SnO_2 and heated continuously to 800°C to observe the weight loss due to the carbon residue.

Further electrochemical characterization was performed using a 2325-type coin cell. For the interest of SnO_2, only a half cell with lithium as a counter electrode was used. The electrode was made of 75% prepared SnO_2, 5% carbon super S (Timcal), 5% carbon graphite (Timcal) and 15% carboxymethyl cellulose (CMC) (prepared with 5 wt% NaCMC from Sigma-Aldrich in aqueous solution) as a binder. The prepared electrode material was coated onto the copper foil, as described by Courtel et al. (2010)[16]. Prior to the coating of the prepared SnO_2 to the copper foil, the copper electrode was washed with 2.5% HCl solution to improve the cleanness. After the coating of the active material, the foil was dried in a vacuum oven at 85°C. The electrolyte used for the cell was 1M $LiPF_6$ in ethylene carbonate/dimethyl carbonate (1:1, v/v) wetted to Celgard separator. The battery was built in an argon-filled glove box to prevent the oxidation of electrolytes and lithium electrodes. To measure capacity, the built cells were cycled at a C/12 rate and tested using cyclic voltammetry techniques describe in Chapter 2.2. The potential of the electrode was swept from open circuit to 5 mV at 0.1 mV/s with a new cell, and then cycled between 5 mV to 1.5 V at the same scan rate (0.1 mV/s) for five cycles.

4.3 Results and discussion

Two-step synthesis of SnO_2 was necessary to achieve macroscopic porous structure of carbon coated SnO_2 and the carbon network in which the SnO_2 were dispersed. PS colloids were used to obtain the porous morphology of SnO_2 and carbon. The challenge here was to synthesize SnO_2 without destroying the PS colloids. To achieve this, a hydrothermal reaction was required. The synthesized SnO_2 with PS colloids was washed with an ethanol solution three times and centrifuged. During the centrifuge, the PS colloids were ordered and

the voids among the colloids were filled with the SnO_2 nanoparticles. Figure 4.1 shows the SEM micrographs of the prepared and dried SnO_2/PS composite. The PS colloids are ordered and preserved. Figure 4.2 shows an XRD pattern of the SnO_2/PS composite. Several peaks can be observed from the figure. A broad peak around 23° 2θ corresponds to carbon graphite 002 reflection, and peaks at 31°, 40°, and 61° 2θ that correspond to SnO_2 110, 101, and 211 reflections, respectively. The space group of the synthesized SnO_2 was P42/*mnm* with the lattice parameters shown in Table 4.1. The values are in agreement with the reference values. No formation of metallic tin or other phases was observed from the XRD patterns.

Table 4.1 Lattice parameters of synthesized SnO_2 compared to reference values

	Synthesized	Reference[17]
a (Å)	4.78	4.73
c (Å)	3.31	3.18

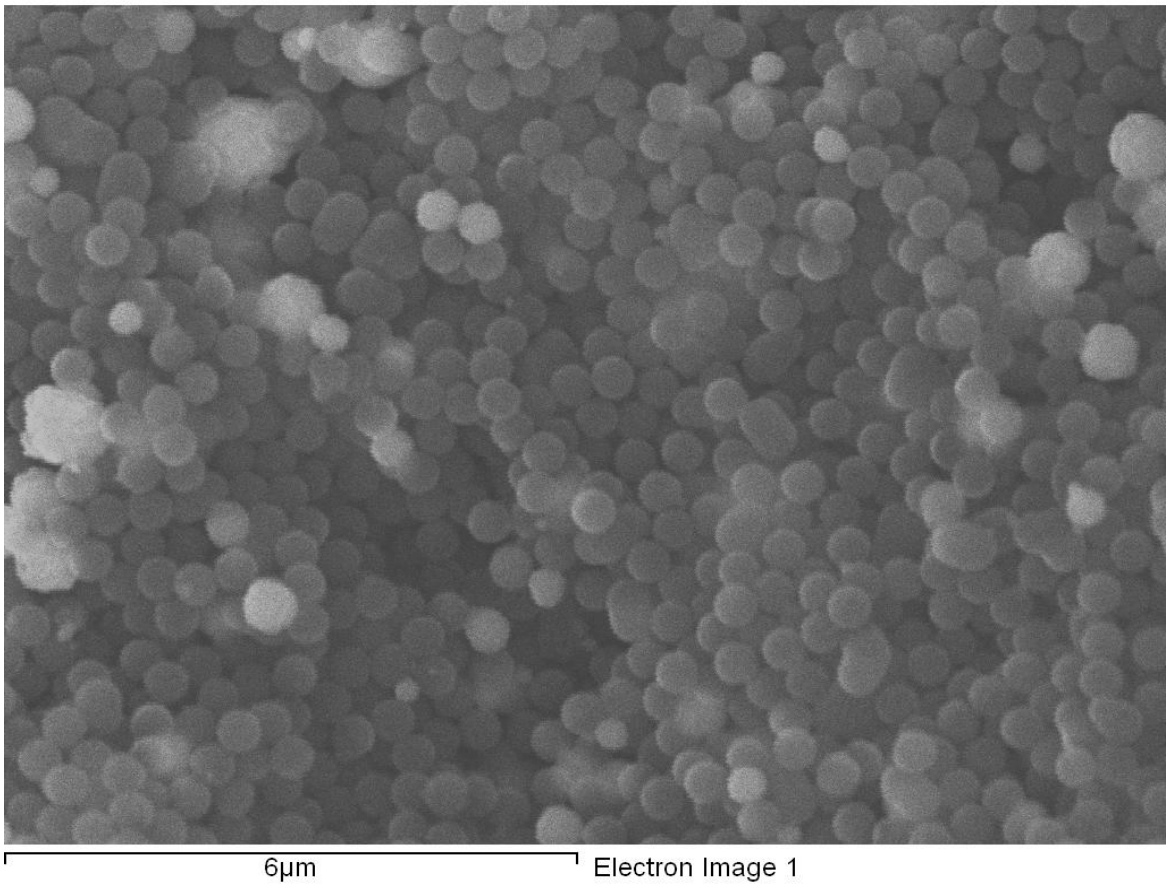

Figure 4.1 SEM micrographs of centrifuged and dried PS colloids with SnO_2 synthesized in a hydrothermal reaction

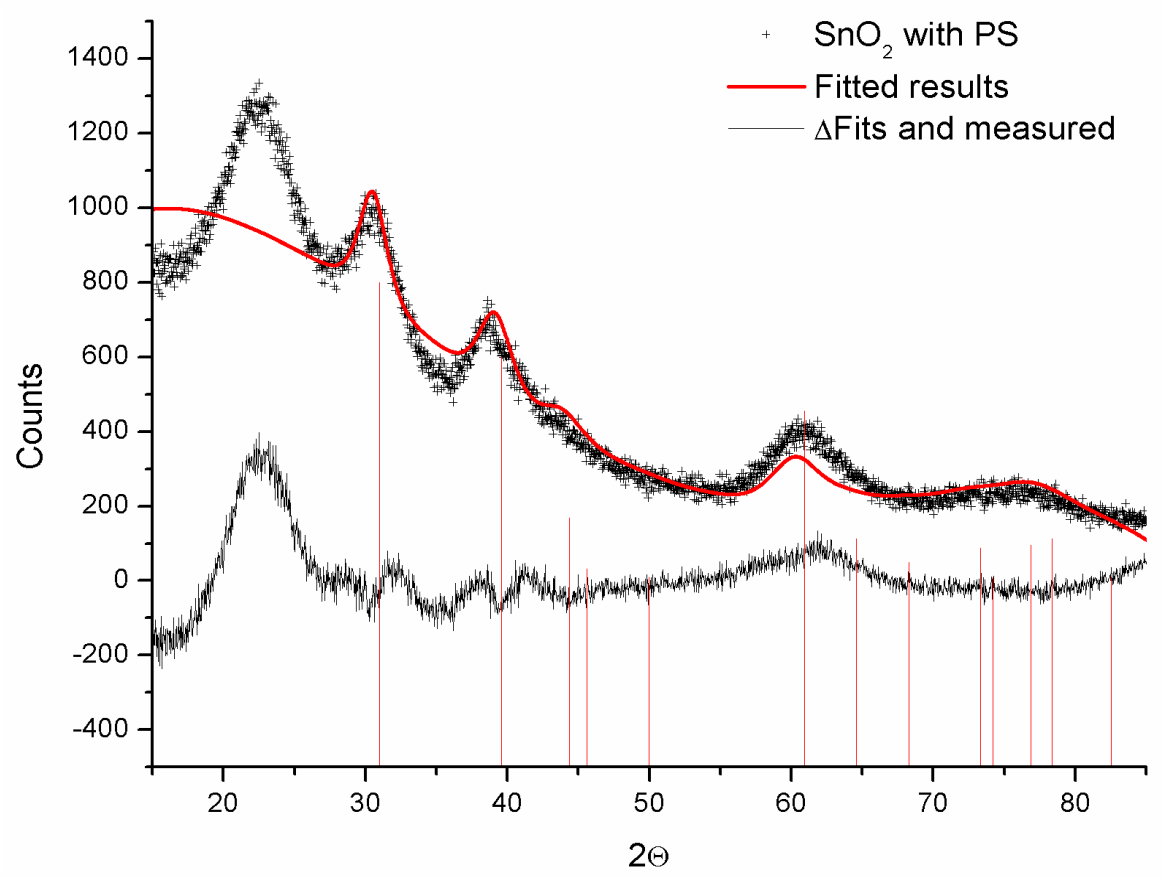

Figure 4.2 XRD pattern of SnO_2/PS composite

The resulting SnO_2/PS composites were calcined under argon in order to obtain porous and carbon-coated SnO_2. A porous morphology was achieved by a slow heating rate at 2°C/min and sintering at two different temperatures in order to prevent the volatile decomposition of PS. The first sintering was conducted at a rate of at 260°C for three hours. The second sintering was conducted at 600°C for another three hours. Since the melting point of PS is 240°C, the first sintering (at 260°C) ensured that the PS melted down from the crystallized SnO_2 phase. Figure 4.3 shows the SEM micrographs after the PS template was removed at 260°C. Traces of PS colloids can be observed by spherical porous morphology

from the SEM micrographs of the calcinated product after the PS removal in Figure 4.3. To verify the crystal structure of the SnO_2, XRD measurements were taken. Figure 4.4 shows the pattern of the final SnO_2. Two phases of SnO_2 and Sn can be observed. The appearance of Sn after calcination is believed to be the result of the reducing atmosphere. The calcining procedure at an elevated temperature under argon with carbon (PS) provided strong reducing conditions, leading to the reduction of Sn^{+4} in SnO_2 to Sn^0. As a result, 1.1% of the Sn element was produced. Due to the high temperature calcination, growth in the size of the crystals was observed, from the narrowed peaks compared to the XRD results in Figure 4.2. Table 4.2 shows the lattice parameters obtained from the XRD results of the sintered SnO_2. These results are also in agreement with the referenced values.

Table 4.2 Lattice parameters of SnO_2 after removal of organic template

		a (Å)	c (Å)
SnO_2	Synthesized	4.74	3.19
	Reference[17]	4.73	3.18
Sn	Synthesized	5.83	3.13
	Reference[18]	5.83	3.18

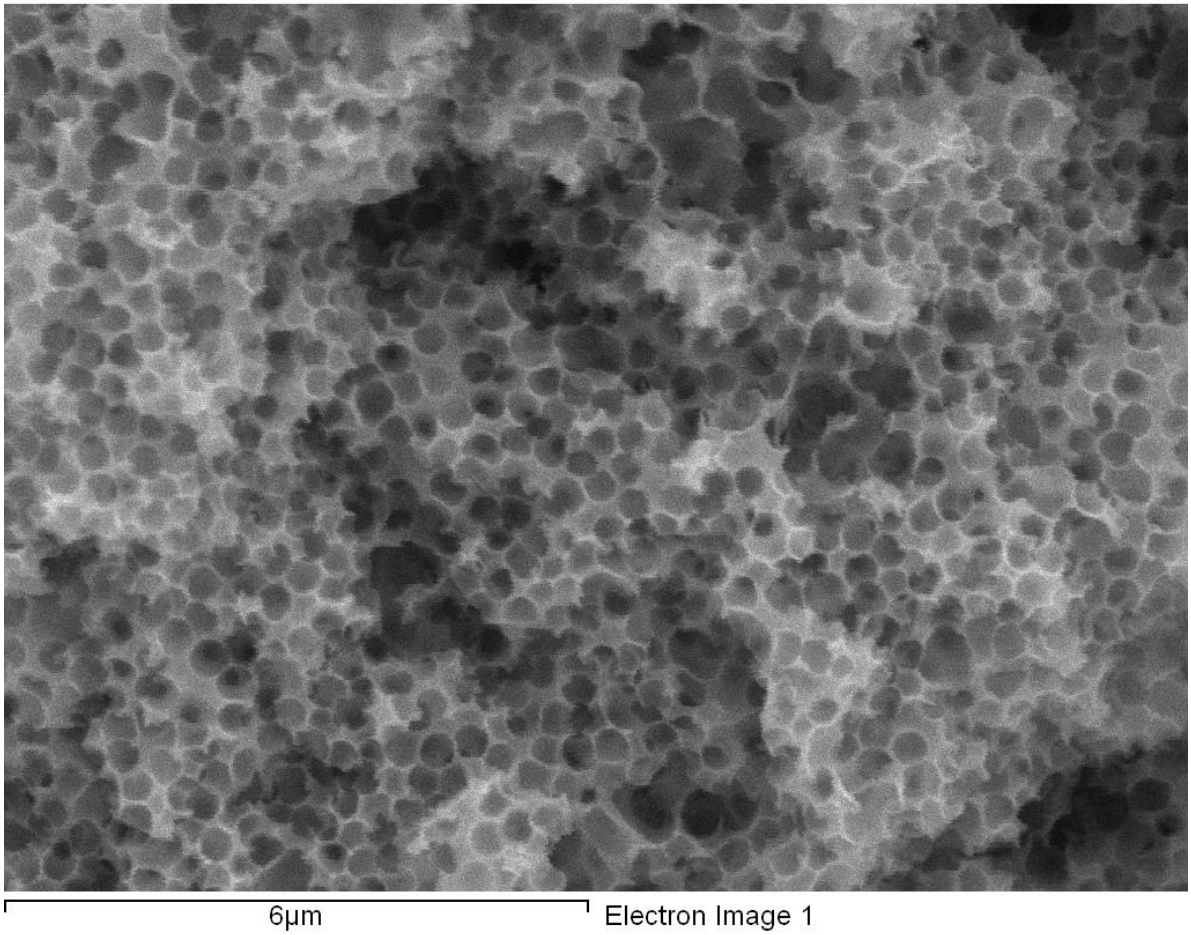

Figure 4.3 SEM micrograph of SnO_2 after PS template removal by sintering

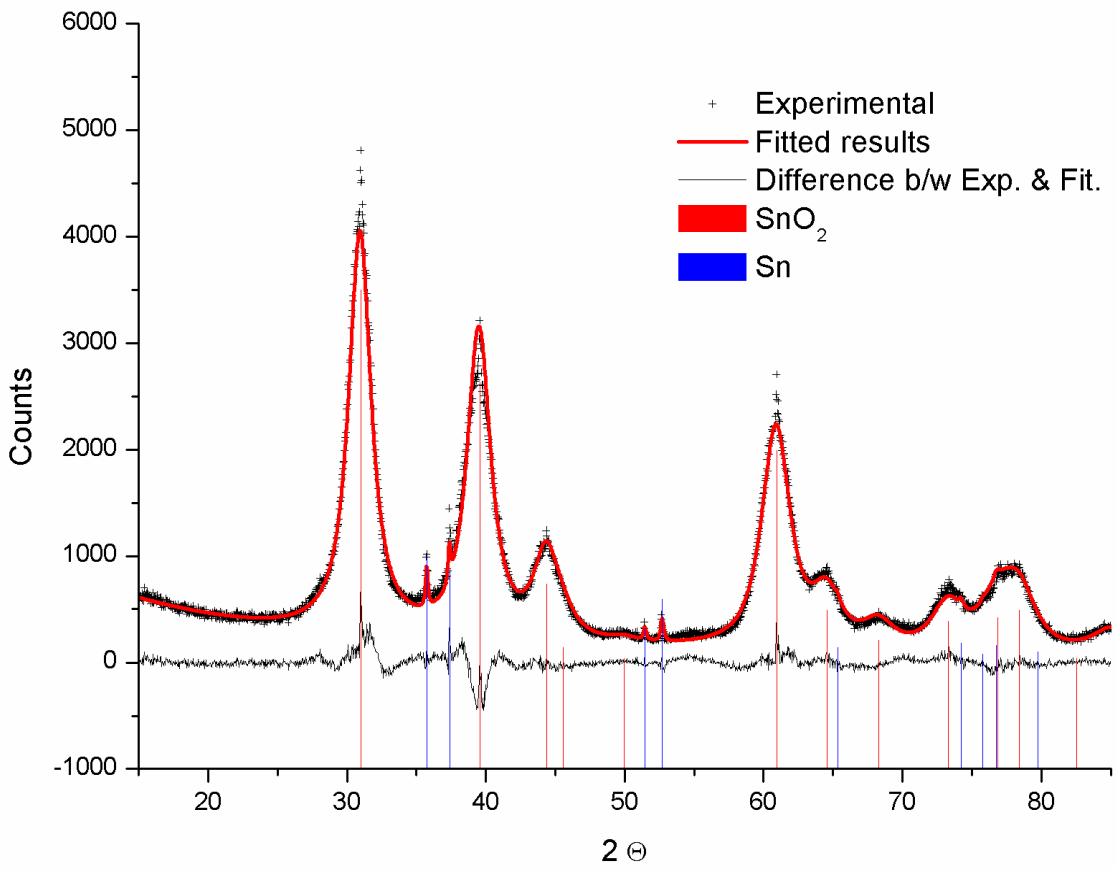

Figure 4.4 XRD pattern of SnO_2 after removal of PS template

To estimate the amount of carbon in the synthesized SnO_2, TGA was conducted on the resulting material, as shown in Figure 4.5. Continuous weight loss was observed when the temperature was raised to 110°C. The temperature was maintained at 110°C for 30 minutes to remove any moisture. Then, the temperature was continuously increased and weight loss was observed due to the decomposition of carbon. Significant weight loss between 350 and 450°C was the result of the decomposition of the carbon residue in SnO_2. From the results, 8.3% of the weight loss occurred due to the carbon decomposition. When

considering that in 1% of Sn, 0.2% weight gain occurred due to the oxidation of Sn. As a result, 0.2% should be added to the 8.3% weight loss to more accurately estimate the amount of carbon in the synthesized SnO_2. The total amount of carbon residue in SnO_2 is 8.5wt%.

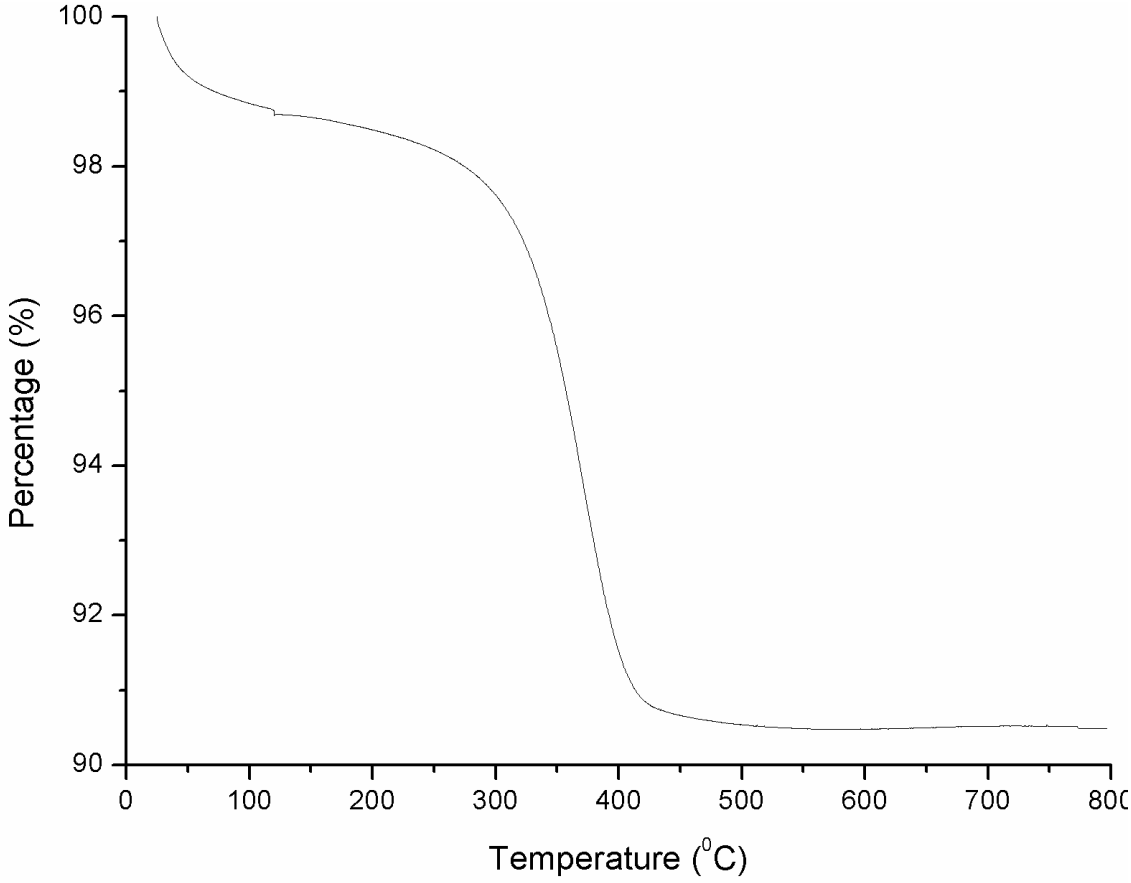

Figure 4.5 TGA analysis of SnO_2/C under air

Figure 4.6 shows the cyclic voltammograms (CVs) of 3DOM SnO_2. The irreversible reduction of SnO_2 to Sn (blue line) can be observed from the first cycle of CVs. This is also

known as Sn activation from SnO_2.[16] A small cathodic peak around 1.25 V (peak A) is due to the Sn reduction, as previously shown by Qiang et al. (2005).[19] The second irreversible cathodic peak at 0.65 V (peak B) is due to solid electrolyte interface (SEI) formation, which is formed during the first charging and discharge cycle caused by reactions of the electrolytes and the active materials at the interface. Both of the peaks disappear after the first cycle. The cathodic peaks shown at 0.1 V (peak b) are due to the formation of a Li_xSn alloy ($0 \leq x \leq 4.4$). The anodic peak at 0.6 V (peak b') is due to the de-alloying of the lithium ion from the Li_xSn alloy. The anodic and cathodic peaks suggest reversibility of the Sn alloying with lithium during the charging/discharging cycle. Additional anodic peaks (1.25 V, peak a') and cathodic peaks (1.0 V, peak a) are observed. These are caused by the lithium alloying with pure Sn from activated SnO_2. Similar results were observed by Mohamedi et al. (2001).[20] The increasing peaks at 0.1~0.65 V (peaks b and b') and decreasing current of the reversible peaks at 1.0~1.25 V (peaks a and a') clearly suggest that more lithium was alloying with LiSn and that less lithium was allowing with pure Sn. It is clear that the carbon coating and amorphous morphology prevented pulverization due to extreme volume expansion by preventing the alloying of Li with pure Sn from the initially activated material.[16,19,20] The noisy cathodic peaks at 0.1 V are due to the multi-stage lithium intercalation of Li_xSn alloys.[20]

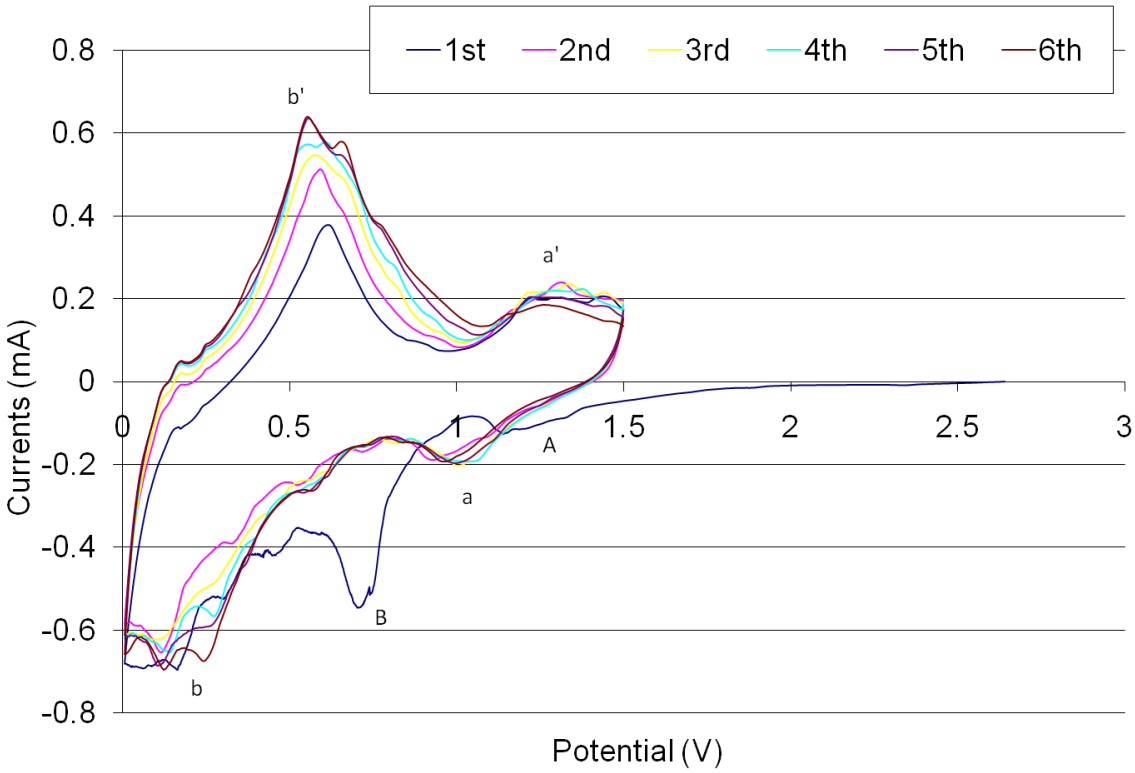

Figure 4.6 Cyclic voltammograms of the synthesized SnO_2

Figure 4.7 shows the first five cycles of the charge/discharge curves. The charge/discharge rates were set to C/12, meaning that the battery could be completely charged or discharged in 12 hours. As previously discussed, the first charge had the highest value due to the irreversible reduction of SnO_2 to Sn and the formation of LiO_x and SEI that resulted in 707 mAh/g of theoretical specific capacity, as explained in Chapter 2. The total specific capacity from the first discharge was 1705 mAh/g. The irreversible capacity of SnO_2 could be observed in the first cycle. The first discharge capacity was 800 mAh/g higher then the first charging capacity due to the Li_xO formation from SnO_2.[16] The first discharge curve contains several fluctuations due to the noise of the equipment. The shift of the

charge/discharge curve to higher capacity suggests the moderate loss discharge capacity. As so, to find the loss of the capacity the charge/discharge capacities were summarized in Figure 4.8 along with the columbic efficiency.

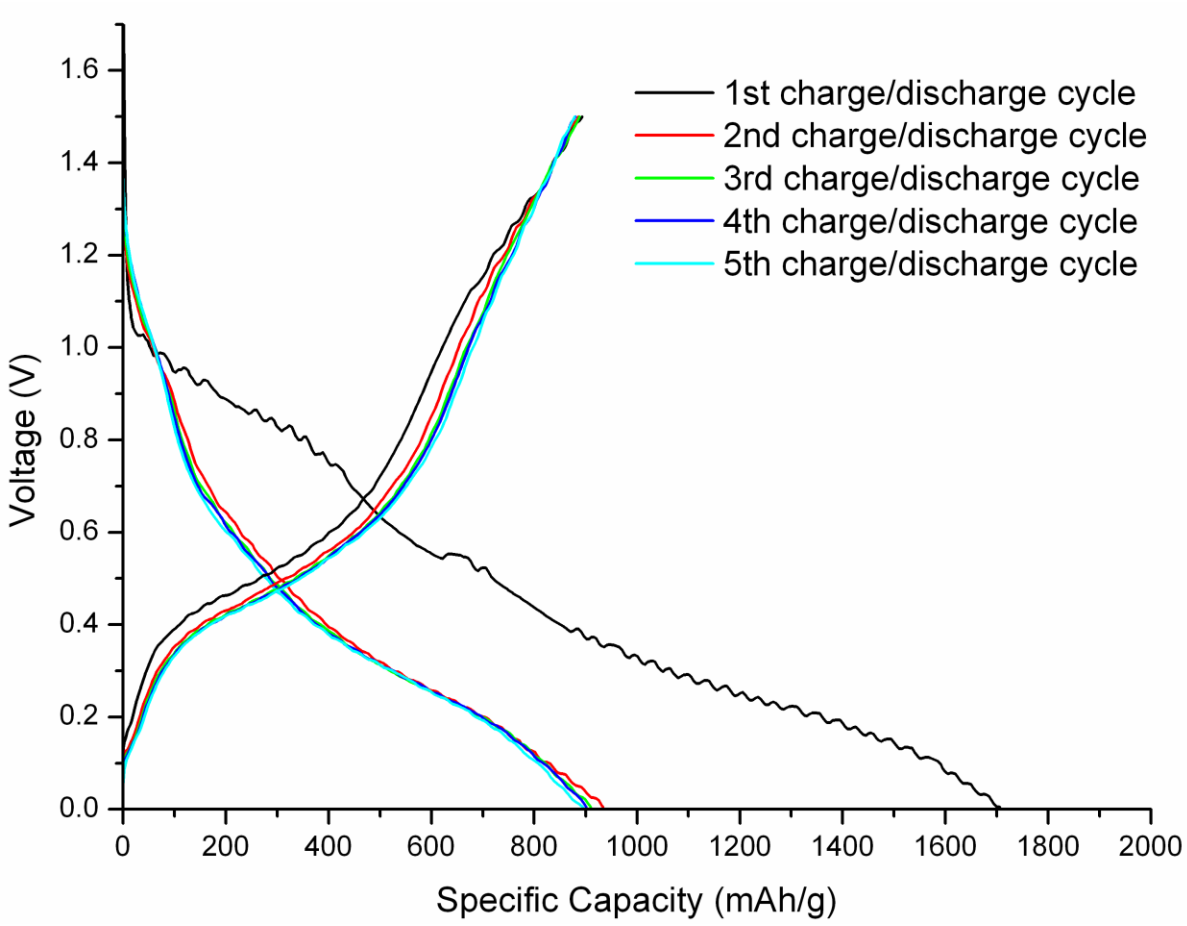

Figure 4.7 The first five charge/discharge curves of SnO_2

Figure 4.8 shows the charge/discharge capacity and the columbic efficiency of the battery. The columbic efficiency of the battery in Figure 4.8 was obtained using Equation

2.11, as described in Chapter 2. The partial reduction of SnO_2 was caused by a smaller charge capacity than discharge capacity, which shows the partial reduction of SnO_2 in every cycle. As a result, higher discharge capacity was shown. Capacity fade was observed in the repeated cycles; however, no efficiency fade was observed. Big capacity fades after fifth cycle was observed after 12 h of resting. The fade had similar trend as the first cycle, where the big charge capacity was observed compared to the discharge capacity that proves a partial reduction of SnO_2. The severe fade after the 12 h of resting was assumed because of the equilibration of the electrolytes, which causes easier diffusion and reduces rest of SnO_2 to Li_xO.

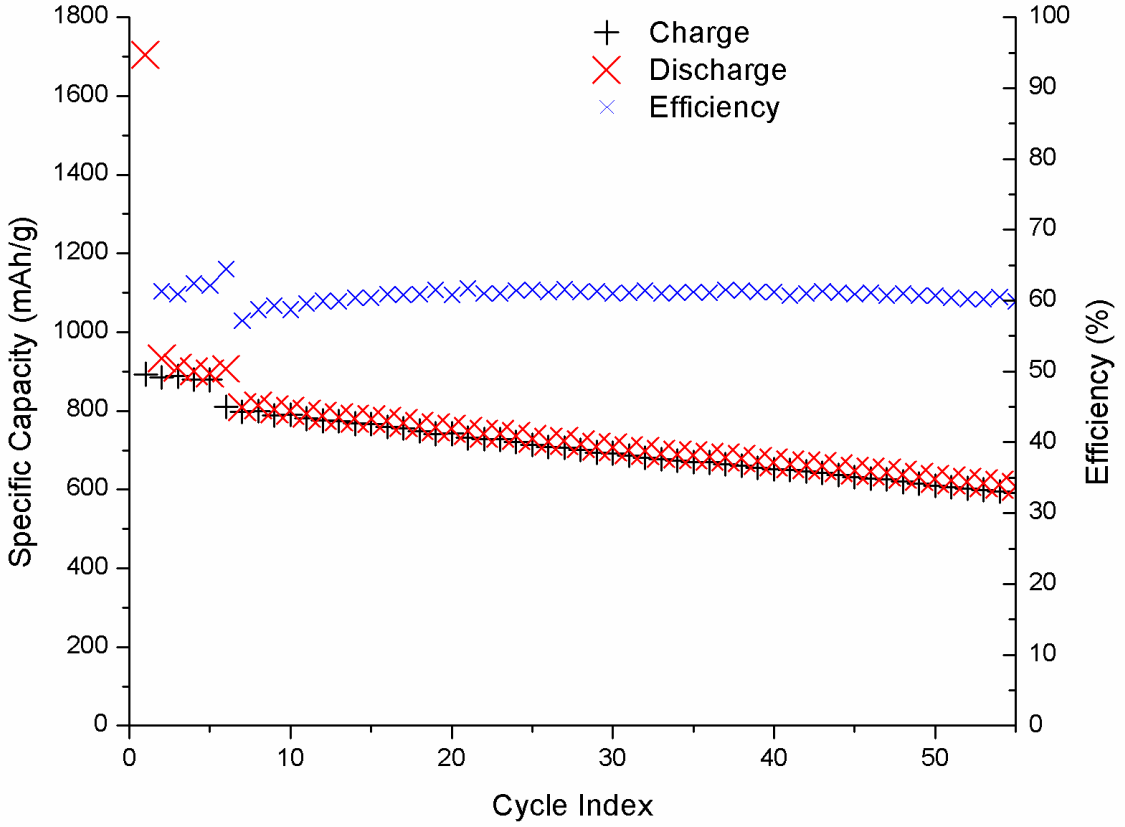

Figure 4.8 Discharge capacity of SnO_2 - Efficiency was calculated with the charge/discharge energy measured from the cell, as described in Chapter 2 (Equation 2.11).

4.4 Conclusions

In the present work, porous nanostrucutured SnO_2 anodic material was synthesized using organic template-assisted hydrothermal synthesis. This synthesis was introduced for the first time in this work. The synthesized SnO_2 provided promising results for battery performance. The synthesized SnO_2 was highly pure and contained 8.5% carbon with porous

morphology. The material synthesized was characterized as an anode in the Li-ion battery and stable performance of the battery was observed, suggesting that nano-sized porous SnO_2 matrix material is very stable and resistant to pulverization during charge/discharge. The obtained SnO_2 had 700 mAh/g of charge/discharge specific capacity with 60% efficiency. Also, the results provided clear evidence of partial activation of SnO_2 to Sn, which may be attributed to the porous matrix of SnO_2.

4.5 References:

1. Nazar, L. F.; Crosnier, O., Anodes and Composite Anodes: An Overview. In *Lithium Batteries*, 2003; pp 112-143.

2. Besenhard, J. O.; Yang, J.; Winter, M., Will advanced lithium-alloy anodes have a chance in lithium-ion batteries? *Journal of Power Sources* **1997,** 68, (1), 87-90.

3. Courtney, I. A.; Dahn, J. R., Electrochemical and in situ X-ray diffraction studies of the reaction of lithium with tin oxide composites. *Journal of the Electrochemical Society* **1997,** 144, (6), 2045-2052.

4. Hassoun, J.; Panero, S.; Simon, P.; Taberna, P. L.; Scrosati, B., High-rate, long-life Ni-Sn nanostructured electrodes for lithium-ion batteries. *Advanced Materials* **2007,** 19, (12), 1632-1635.

5. Yu, Y.; Chen, C. H.; Shi, Y., A tin-based amorphous oxide composite with a porous, spherical, multideck-cage morphology as a highly reversible anode material for lithium-ion batteries. *Advanced Materials* **2007,** 19, (7), 993-997.

6. Lee, J. Y.; Zhang, R.; Liu, Z., Lithium intercalation and deintercalation reactions in synthetic graphite containing a high dispersion of SnO. *Electrochemical and Solid-State Letters* **2000,** 3, (4), 167-170.

7. Moon, T.; Kim, C.; Hwang, S. T.; Park, B., Electrochemical properties of disordered-carbon-coated SnO2 nanoparticles for Li rechargeable batteries. *Electrochemical and Solid-State Letters* **2006,** 9, (9).

8. Holland, B. T.; Blanford, C. F.; Do, T.; Stein, A., Synthesis of Highly Ordered, Three-Dimensional, Macroporous Structures of Amorphous or Crystalline Inorganic Oxides, Phosphates, and Hybrid Composites. *Chemistry of Materials* **1999,** 11, (3), 795-805.

9. Cassagneau, T.; Caruso, F., Inverse opals for optical affinity biosensing. *Advanced Materials* **2002,** 14, (22), 1629-1633.

10. Reese, C. E.; Baltusavich, M. E.; Keim, J. P.; Asher, S. A., Development of an intelligent polymerized crystalline colloidal array colorimetric reagent. *Analytical Chemistry* **2001,** 73, (21), 5038-5042.

11. Weissman, J. M.; Sunkara, H. B.; Tse, A. S.; Asher, S. A., Thermally switchable periodicities and diffraction from mesoscopically ordered materials. *Science* **1996,** 274, (5289), 959-960.

12. Cheng, W.; Wang, J.; Jonas, U.; Fytas, G.; Stefanou, N., Observation and tuning of hypersonic bandgaps in colloidal crystals. *Nature Materials* **2006,** 5, (10), 830-836.

13. Joannopoulos, J. D.; Villeneuve, P. R.; Fan, S., Photonic crystals: Putting a new twist on light. *Nature* **1997,** 386, (6621), 143-149.

14. Yablonovitch, E., Photonic crystals: Semiconductors of light. *Scientific American* **2001,** 285, (6), 34-41.

15. Fischer, U. C.; Zingsheim, H. P., SUBMICROSCOPIC PATTERN REPLICATION WITH VISIBLE LIGHT. *Journal of vacuum science & technology* **1981,** 19, (4), 881-885.

16. Courtel, F. M.; Baranova, E. A.; Abu-Lebdeh, Y.; Davidson, I. J., In situ polyol-assisted synthesis of nano-SnO2/carbon composite materials as anodes for lithium-ion batteries. *Journal of Power Sources* 195, (8), 2355-2361.

17. Maekawa, T.; Minagoshi, C.; Nakamura, S.; Nomura, K.; Kageyama, H., Crystal structure analysis of the catalysts based on tin oxide using a neutron diffraction method. *Chemical sensors* **2008,** 24, 3.

18. Wolcyrz, M.; Kubiak, R.; Maciejewski, S., X-RAY INVESTIGATION OF THERMAL EXPANSION AND ATOMIC THERMAL VIBRATIONS OF TIN, INDIUM, AND THEIR ALLOYS. *Physica Status Solidi (B) Basic Research* **1981,** 107, (1), 245-253.

19. He, Z.-Q.; Li, X.-H.; Xiong, L.-Z.; Wu, X.-M.; Xiao, Z.-B.; Ma, M.-Y., Wet chemical synthesis of tin oxide-based material for lithium ion battery anodes. *Materials Research Bulletin* **2005,** 40, (5), 861-868.

20. Mohamedi, M.; Lee, S. J.; Takahashi, D.; Nishizawa, M.; Itoh, T.; Uchida, I., Amorphous tin oxide films: Preparation and characterization as an anode active material for lithium ion batteries. *Electrochimica Acta* **2001,** 46, (8), 1161-1168.

Chapter 5

Hybrid Pulse Power Characterization on $LiFePO_4$ and its Comparison to State-of-the-Art $LiCoO_2$

5.1 Introduction

The development and design of a fuel-efficient car has been an ongoing challenge in recent years. This has become even more important lately due to greenhouse gas generation and global warming. Major car manufacturers have developed new vehicles called Plug-in Hybrid Electric Vehicles (PHEVs) that run on a newly developed power train system. PHEVs operate partially on an electric motor and partially on a conventional gasoline engine. As a result, the importance of electric energy generation and energy storage in PHEVs

increases significantly. Lithium-ion (Li-ion) batteries have been suggested for electrical energy production and storage due to their high capacity (~200 Ah/kg). However, because of the high cost of the active materials needed for Li-ion batteries, as well as their low efficiency and stability, new materials are being investigated. $LiFePO_4$ (LFP) is one of the excellent candidates for cathode materials.

Hybrid pulse power characterization was developed to test battery performance in electric vehicles.[1] For electric vehicles, battery operation is extreme when compared to that of small portable devices or industrial stationary batteries, which are regular, steady and stable. Energy consumption is extremely dynamic in vehicles. Normal driving conditions in a vehicle consist of: acceleration, cruising and deceleration. In each stage, the battery has to be able to withstand dynamic conditions in order for the PHEV to run. Simple hybrid pulse power characterization testing comprises three steps, which correspond to the three major driving stages: high-pulse discharge for acceleration, open-circuit resting or low discharge rate for cruising and high pulse charge for deceleration.

In this chapter, two materials were tested: $LiCoO_2$ (LCO) and LFP. LCO is a common material currently used for cathodes in Li-ion batteries. HPPC testing was used to study several types of batteries with a variety of active materials.[2-9] All of the HPPC was conducted on full-cell batteries with the aim of determining their feasibility in electric vehicles[7, 8] and testing for aging, [2, 3, 9] which is an accumulation of capacity fade in a battery. To study fundamental phenomena of the HPPC testing in the current active materials, the experiment was designed to show the voltage profile of the HPPC effect on a single active material and also to test the direct feasibility of the active material in PHEVs.

5.2 Experimental

5.2.1 Synthesis of the cathode material, $LiFePO_4$

A solid-state reaction was used to synthesize $LiFePO_4$ (LFP). Li_2CO_3 (Sigma-Aldrich, 99%), $Fe(C_2H_3O_2)_2\,2H_2O$ (Riedel deHaen, 99%), and $NH_4H_2PO_4$ (Sigma-Aldrich, 99%) were mixed in a molar ratio of 0.5:1:1. Citric acid was added to the mixture to carbon coat the LFP. The amount of citric acid was 5 wt% of final synthesized LFP. The mixture was soft ball milled using a 60 mL NALGENE jar (VWR) with zirconia beads (Tosoh Corp, 5 mm diameter) for homogenous mixing. Enough acetone to fill half of the NALGENE jar was added to the mixture with 20 zirconia beads. The mixture was ball milled for three days—the jar was placed into the vibrator at room temperature. Once the ball milling was complete after three days, the acetone in the mixture was evaporated under a fume hood. The remaining mixture was sintered under argon at 700°C with 10 ^{0}C/min heating rate. The material for $LiCoO_2$ (LCO) was purchased from Umicore Group, Begium.

5.2.2 Preparation of the electrochemical cells for HPPC

The active materials, LFP and LCO, were mixed with carbon super S (Timcal, Canada), carbon graphite (Timcal, Canada) and 3wt% polyvinylidene fluoride (PVDF, Kynar Flex 2800, Canada) dissolved in N-Methyl-pyrrolidinone (NMP, Aldrich, Canada). Table 5.1 summarizes the ratio of the mixtures for LFP and LCO. The prepared electrode material was used to coat on aluminum foil, as described in Chapter 3.2.4.

Table 5.1 Active material used for Li-ion batteries to test HPPC

	LFP (%)	LCO (%)
Active material	80.15	80.15
Carbon super S	4.91	4.94
Graphite	4.91	8.55
PVDF	10.03	6.36

5.2.3 HPPC profile

All batteries were tested using a multichannel galvanostat (Arbin instrument BT2000). Prior to the HPPC testing, all batteries were fully charged and discharged to measure their full capacity. For the LFP half-cell battery, 1C charging was used and kept at 4.2 V until the current reached C/60. This is also referred to as constant current, constant voltage (CC-CV) charging. For the LCO half-cell battery, C/12 charging was used. For both half-cell batteries, C/12 discharge rates were used to measure the full discharge capacity. All batteries were tested at room temperature (25°C). To measure the HPPC at different states of charge (SOCs), the batteries were fully charged and rested for one hour to stabilize and equilibrate the electrolytes. After the HPPC cycle, the LFP cell was discharged for 6 minutes at C/1. The LCO cell was discharged for 72 minutes at C/12. Both cells were set to discharge 10% of the theoretical specific capacity in order to reveal the phenomena of pulse charging/discharging profile at different SOCs.

The HPPC profile from the PNGV (Partnership for a New Generation of Vehicles) Battery Test Manual[1] was used and adapted to test the half cells. The HPPC profile comprised four steps. The first step involved resting to obtain the stable and stationary state of the cells. The cells were left in open circuit and the voltages were measured. The second step was pulse discharge, in which the cells were exposed to 5C for 18 seconds. The potentials were measured and recorded. The third step involved a resting period of 32 seconds, during which the cells were left in open circuit. The fourth step was pulse charge, in which the cells were exposed to 3.75C for 10 seconds. Following the full cycle of HPPC, the batteries were discharged for 10% of the active materials' specific capacity. The voltages were measured during the HPPC cycles, during the one hour of resting and during discharge. Figure 5.1 shows the current profile of the HPPC for LFP cells and Figure 5.2 shows one cycle of HPPC. In all cases, the limits for the potential range were set between 2.5 and 4.2 V to prevent a decomposition of electrolytes and active materials. As a result, when the measured potential exceeded the potentials, the HPPC profile continued to the next step.

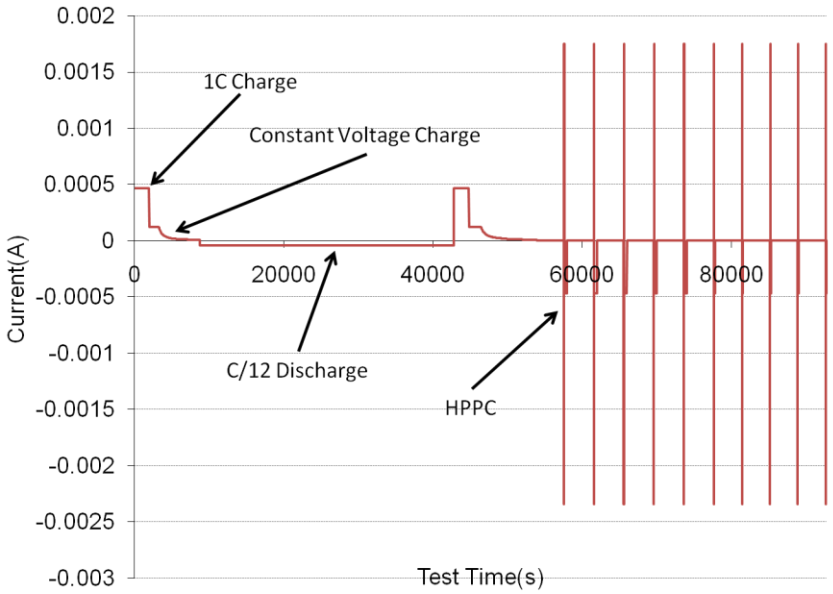

Figure 5.1 Example of current profile for CC-CV charging, C/12 discharging and HPPC for LFP

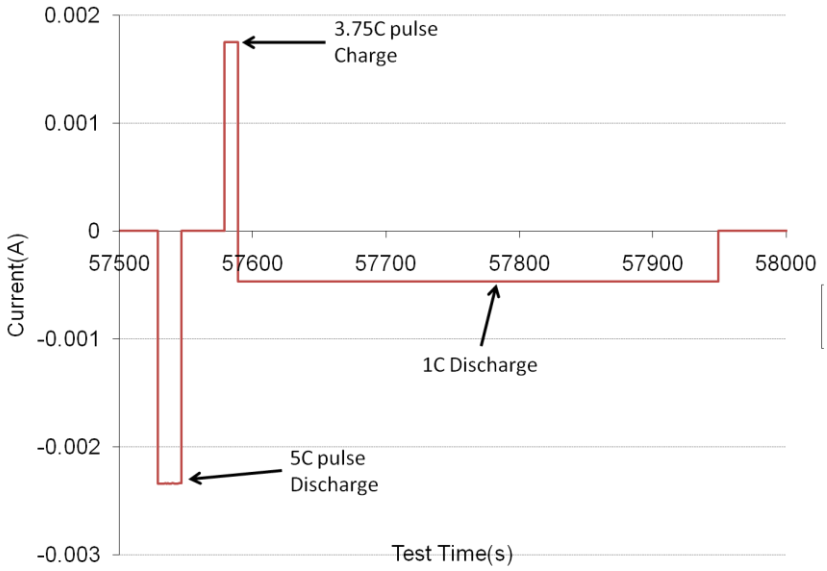

Figure 5.2 First cycle of HPPC at 5C discharge (18s), resting (32s), 3.73C charge (10s) and 1C discharge for 6 minutes to reduce 10% SOC

5.3 Results and discussion

HPPC profile was performed on the LFP half cell and the results are shown in Figure 5.3 to Figure 5.9. Figure 5.3 shows the measured potential from the HPPC profile of LFP. Each HPPC cycle has a different SOC, as shown in Table 5.2. The SOC is calculated using the total specific discharge capacity obtained from the prior charge/discharge cycle at C/12. From the obtained full specific capacity, the charge/discharge capacities were added and subtracted cumulatively to the full capacity prior to the HPPC cycle. In all cases of charge/discharge, the limits for the potential range were set between 2.5 and 4.2 V to prevent battery failure. At lower SOCs (<60%), incomplete pulse discharge was observed due to the potential limits and attempts to prevent battery failure. The incomplete pulse discharge was due to slower lithiation onto LFP compared to the potential change caused by the charge transfer of the electrodes, as described in Chapter 2.2.1. The results clearly show that the limit of the pulse discharge depends on the SOC. The full period of pulse charge could be obtained from all SOC

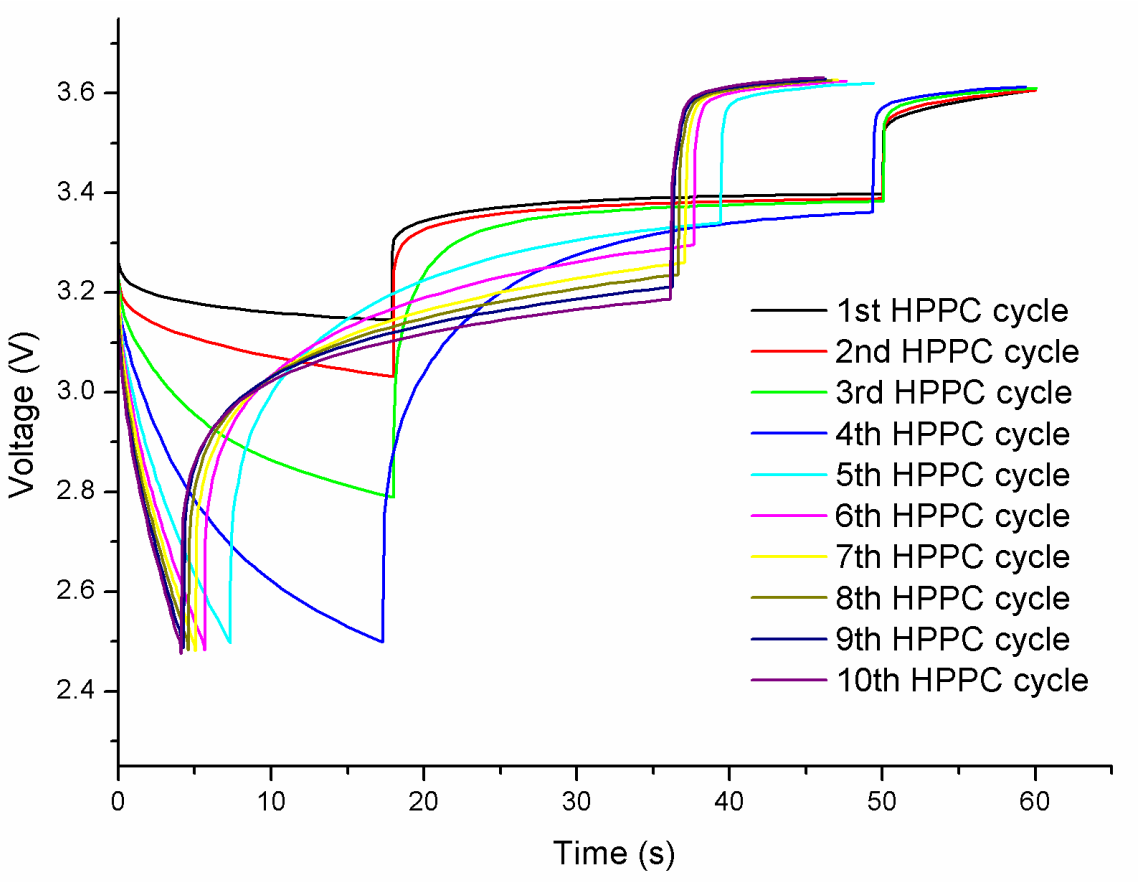

Figure 5.3 Potential measured for LFP by the HPPC profile

Table 5.2 SOC for each HPPC cycle of LFP

HPPC cycle	SOC (%)
1	100.0
2	85.4
3	70.9
4	56.3
5	41.9
6	29.2
7	24.6
8	21.4
9	18.7
10	16.3

Figure 5.4 shows the resistance, calculated during the change in voltage by the pulse charge and discharge, plotted versus the SOC, from the HPPC profile. The total resistances are obtained by calculating the change of potential during pulse charge or discharge divided by the pulse C-rate. It clearly shows an decrease in resistance at higher SOCs due to the lack of a lithium acceptor site at lower SOC[10]. The results also show a lower charge resistance due to a lower C-rate, 3.75C compared to 5C. A similar trend—decreased resistance at higer SOCs—was observed due to the lower open circuit potential following the 32-second resting period. Figure 5.5 shows that, at lower SOCs, the time to recover the equilibrium potential

takes longer, while full recoveries were observed after the one-hour resting period with the constant potential in every cycle.

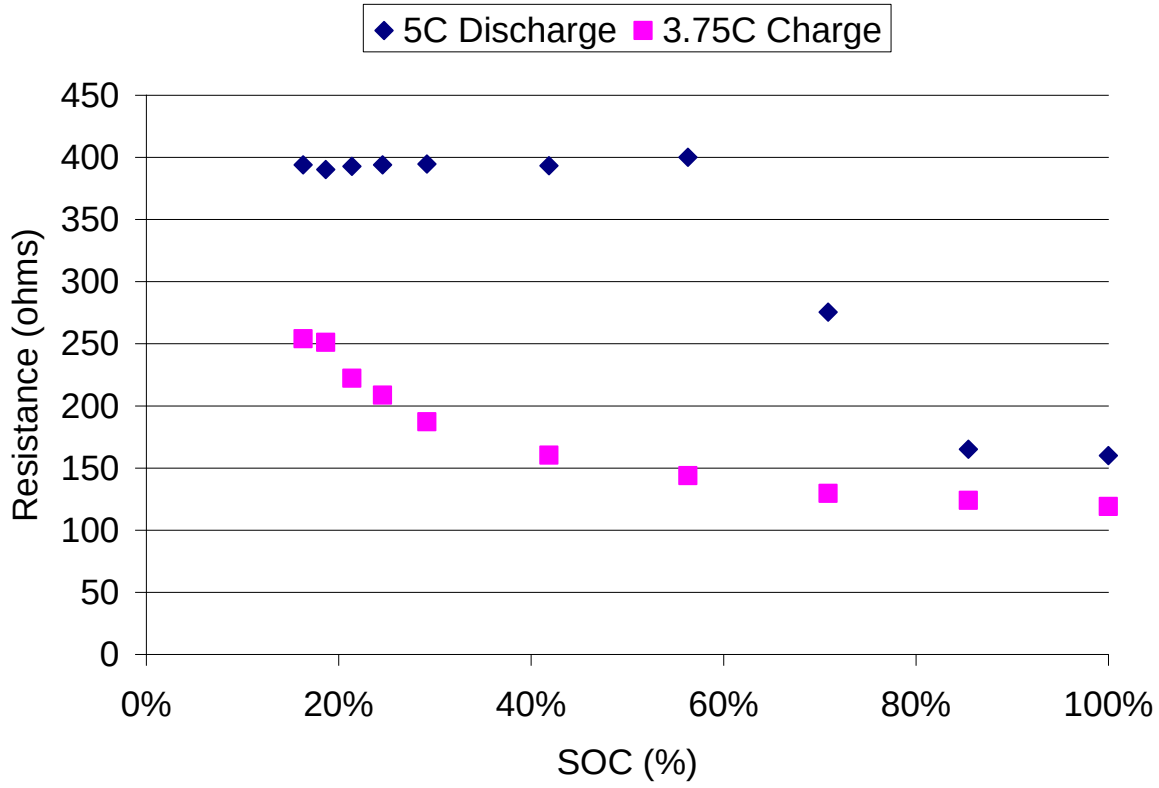

Figure 5.4 Resistance of LFP at different SOCs during the HPPC

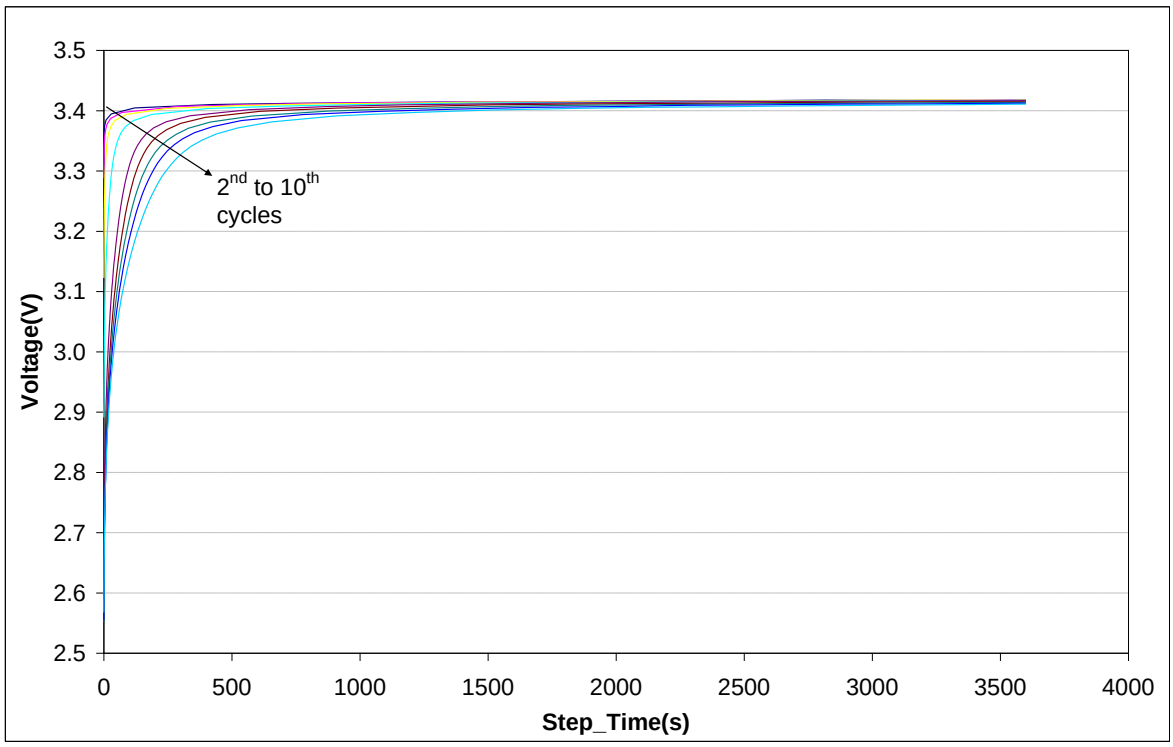

Figure 5.5 Potential measured during 1 h resting period of LFP

At lower SOCs, the pulse discharge cannot tolerate the full HPPC cycle due to the increase in resistance caused by high diffusion polarization resistance described in Chapter 2.2. To clarify the time that could handle the pulse charge/discharge, the duration was recorded in Figure 5.6. As a result, the pulse discharge could not achieve 18s of 5C rate at a SOC under 56.3%. LFP could deal with the pulse charge at all SOCs by full 10 seconds of 3.75C, as seen in Figure 5.6. Pulse charging at all SOCs, the LFP cell withstands 10 s of pulse 3.75C charge. However, it can only withstand 18s of pulse 5C discharge down to 60% of SOC. In lower SOC, it could only withstand 4 to 6 s at 18 to 30% SOC at 5C discharge.

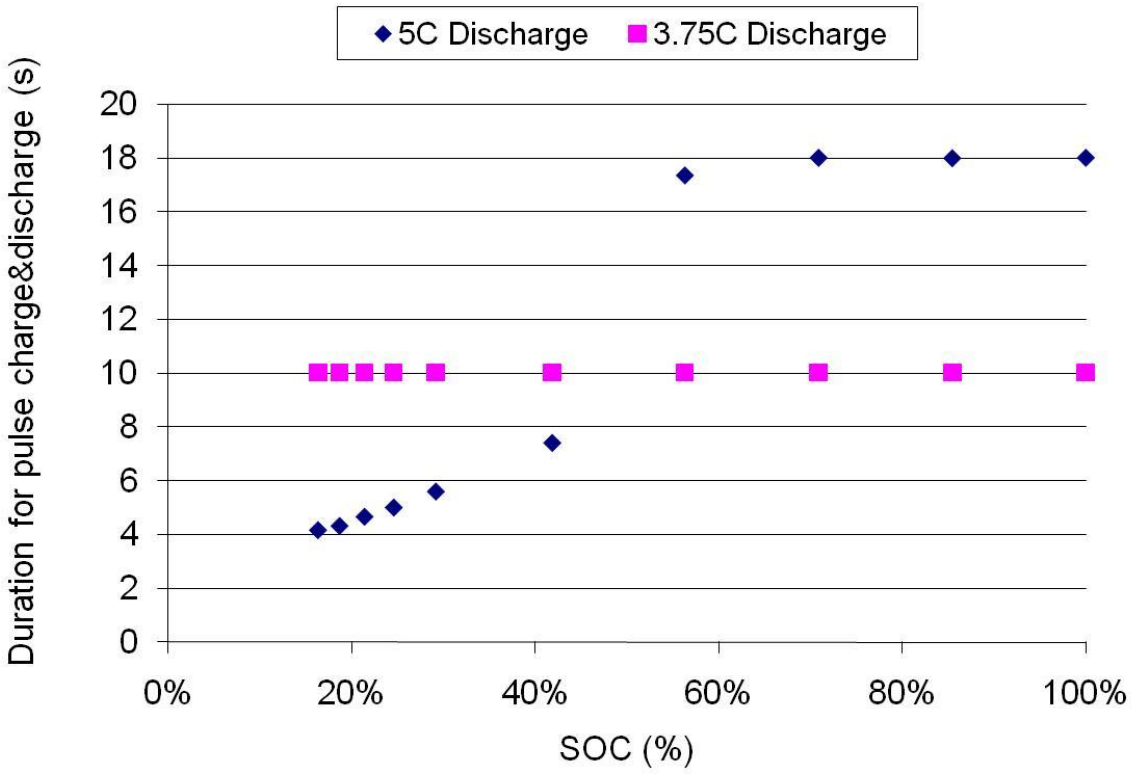

Figure 5.6 Duration of pulse charge/discharge of LFP at different SOCs

Different pulse C-rate but same pulse C-rate charge/discharge profiles were tested to compare resistance. To achieve full pulse profile during charge/discharge, low pulse C-rate was tested. The test was performed to see the resistance as a function of SOC by eliminating the effect of C-rate. Figure 5.7 shows the HPPC profile at different SOCs with 2.3C. These have a lower C-rate than the previous HPPC profiles. Similar results were obtained: as the SOC decreased, the diffusion resistance increased. As a result, dramatic drops of potentials were observed at the end of the pulse discharge. However, during the pulse charge, no increase of potentials was observed, but an increase of resistance due to lower open circuit

potentials at the beginning of the pulse charge was observed, as shown in Figure 5.3 and Figure 5.7. The potentials after 32 seconds decreased in every cycle due to the lower SOC.

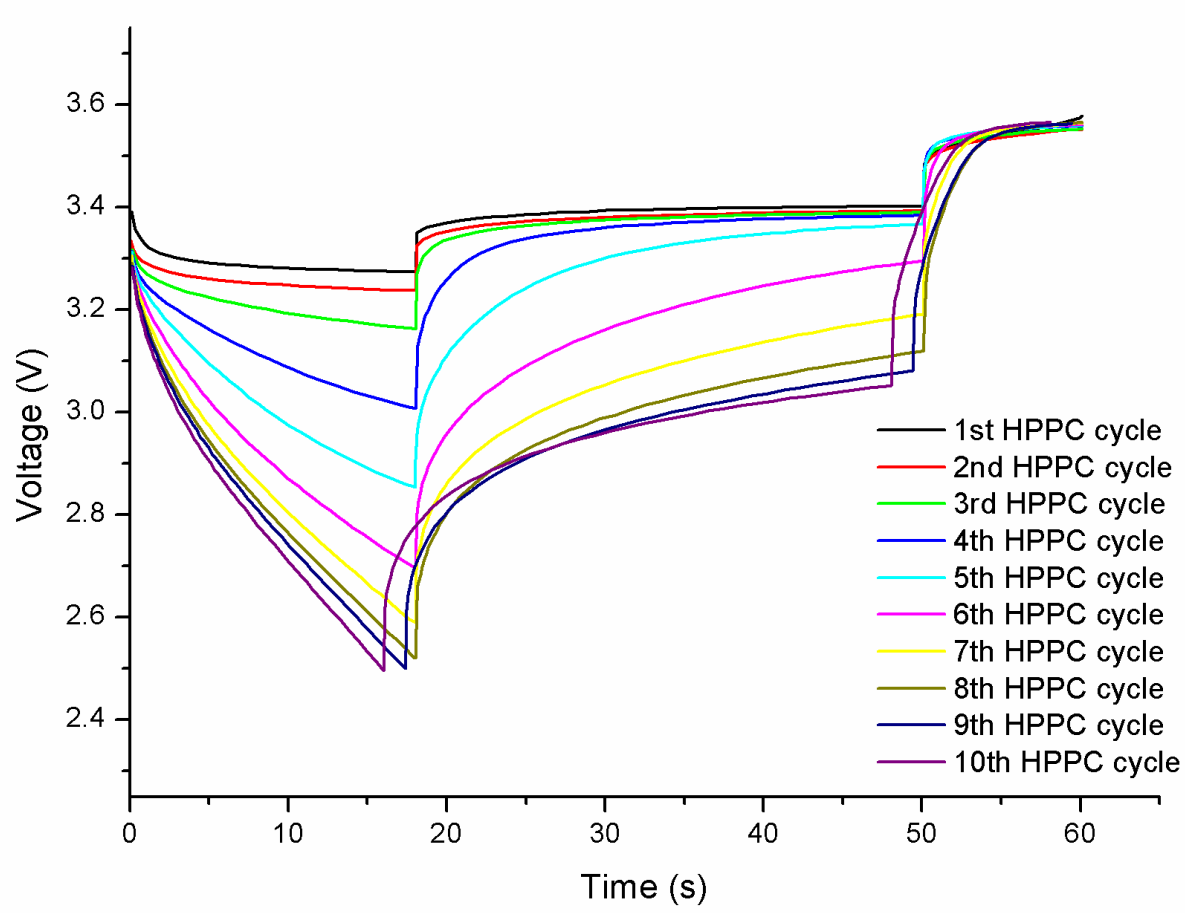

Figure 5.7 HPPC profile with 2.3C of pulse charge/discharge for LFP

Resistance at high SOCs was smaller for pulse charge/discharge compared to the resistance at low SOCs. As the SOC decreased, the resistance at the pulse discharge increased more than the resistance at the pulse charge. This could be explained by a lack of

lithium-accepting sites due to an increase of diffusion polarization resistance. In both the pulse charge and discharge, an increase in resistance was observed. As mentioned previously, the increase in resistance at low SOC during the pulse discharge was caused by the increase diffusion polarization resistance. However, the increase in resistance during the pulse charge was the result of insufficient time to stabilize potential during 32 seconds of resting. This can be observed in Figure 5.5. As the SOC decreased, the time required to stabilize the potential increased. As a result, immediately following the 32-second resting period, the pulse charge started at a lower potential and SOC, leading to greater difference between the initial and final potentials. This difference of potentials resulted in greater resistance at low SOC for pulse charge.

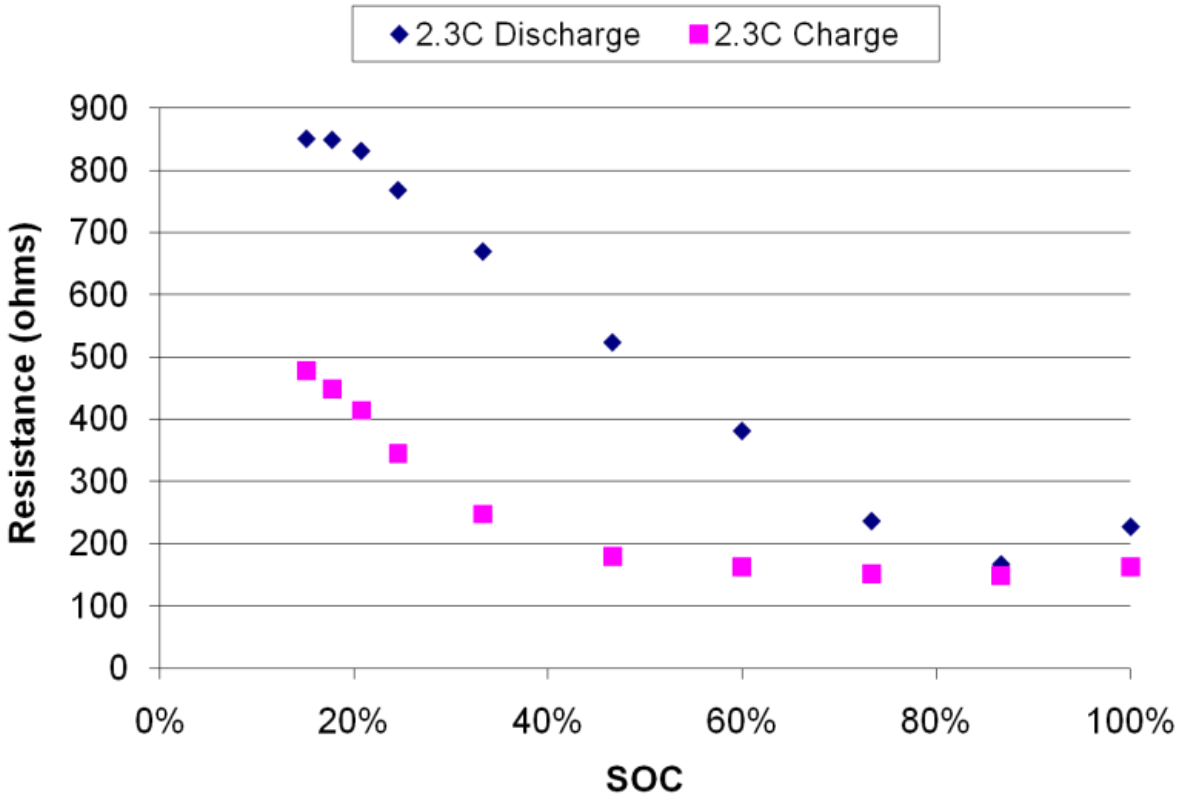

Figure 5.8 Resistance measured from HPPC at 2.3C pulse charge/discharge for LFP

The battery withstands better in lower pulse discharge (2.3C), as shown in Figure 5.9, compare to higher C-rate (5C). Similar results were confirmed by Delacourt et al. (2006)[11] where a significant drop and 0 mAh/g of capacity was observed when the LFP cell was discharged at a high C-rate (5C) . The capacity drop at a high C-rate could be prevented by the addition of more carbon source into the active material in order to disperse the LFP in the electrodes[11]. Based on the two HPPC results of LFP, the SOC affects the maximum pulse discharge rate; however, it does not have any effect on the pulse charge rate.

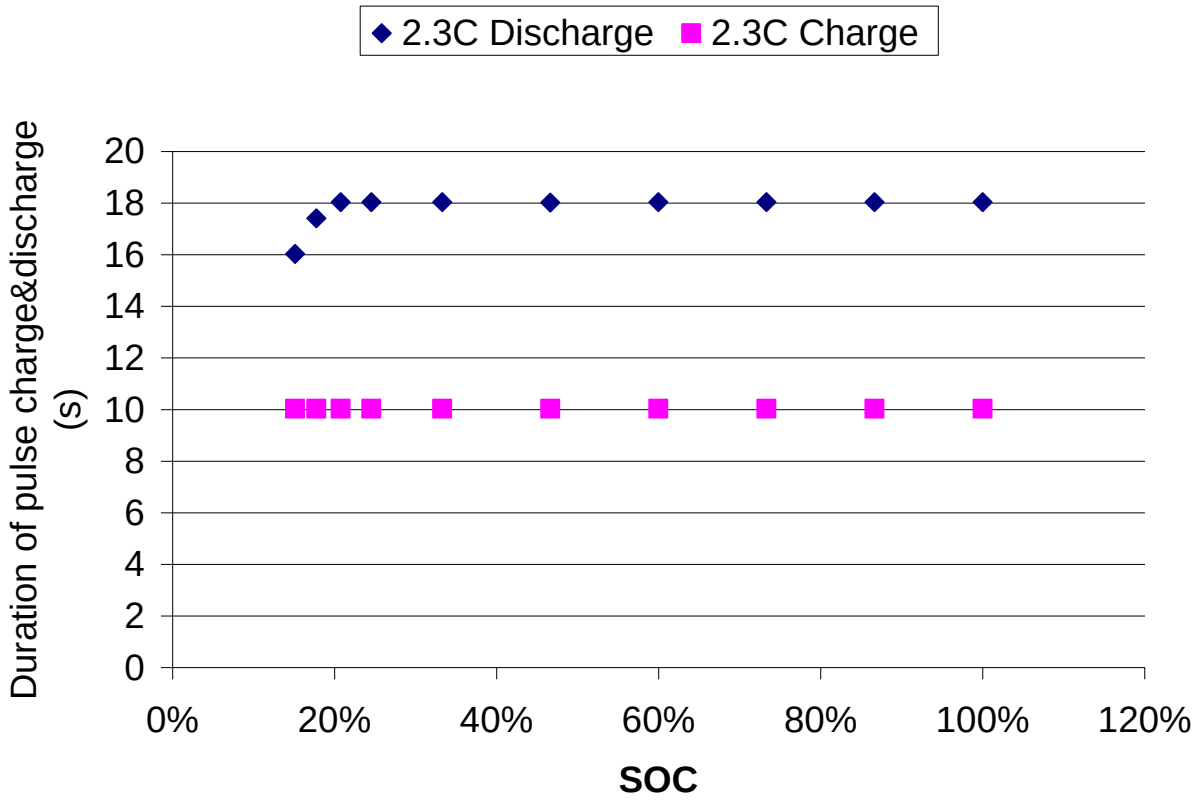

Figure 5.9 Duration of pulse charge/discharge at 2.3C for LFP

HPPC on LCO was also tested, the results of which are shown in Figure 5.10 to Figure 5.12. Table 5.3 shows the SOC in each HPPC cycle. The LCO was not able to achieve the full HPPC profile in any SOC. As shown in Figure 5.10 and Figure 5.11, the full 10 seconds of the pulse charge during HPPC could not be obtained in all SOCs. The reason for the incomplete pulse charge/discharge is the high conductivity of LCO. Due to this high conductivity of LCO, the lithium insertion is the main rate limiting reaction for charging ($Li_xCoO_2 + Li_{(1-x)} \rightarrow LiCoO_2$, $0 < x < 1$). As a result, the safety limits for the potentials (2.5V and 4.5V) were reached much faster. The results show that LCO is not a good candidate for

EV due to the incomplete pulse charge, as shown in Figure 5.10. However, the previous work on full cells, which successfully performed the full HPPC profile, suggests the importance of the anode materials.

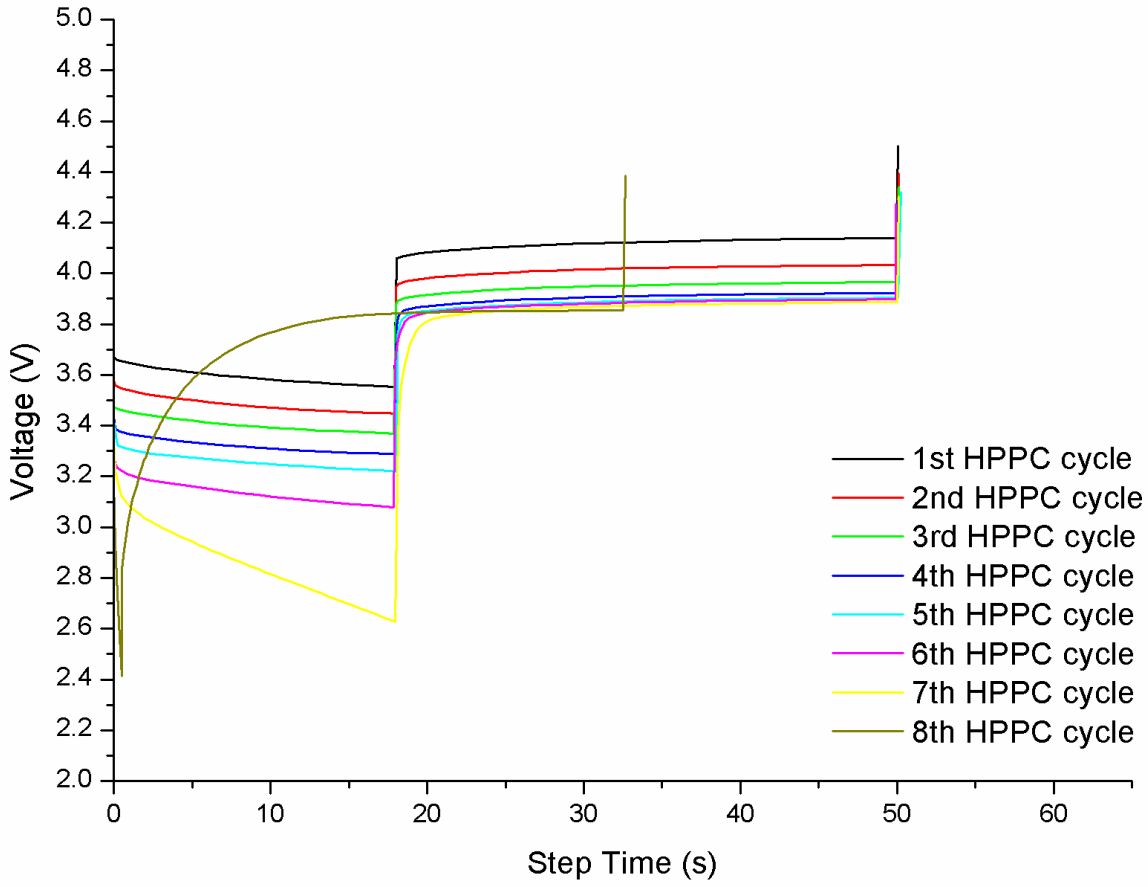

Figure 5.10 HPPC cycle of LCO a function of SOCs

Due to the higher electrical conductivity of LCO compared to LFP, resistance at all SOCs was lower than that of LFP. Moreover, due to the safety limitations of the HPPC

profile design, the LCO could not achieve the full duration of pulse 3.75C charge. The potential reached the limits without completing the pulse charge that the profile preceded to the next stage of the HPPC profiles. Figure 5.11 shows the constant resistance. From the 8th HPPC cycle (2% SOC), the full pulse discharge lasted less then 1 s due to the increase of the diffusion polarization resistance. Resistance of LCO as a function of SOC also increased as the SOC lowers for both pulse charge/discharge. However, the resistance during the pulse charge increased small amount compare to the increase resistance from LFP. The reason for the small increase in the resistance can be explained from Figure 5.11, where the potential stabilise faster at 32 s of resting period then LFP, which might be due to the lower diffusion polarization resistance compared to LFP. Figure 5.12 shows the duration of the pulse charge/discharge. At all SOCs, the pulse charge was stopped due to the sudden increase in potential. However, the discharge pulse was achieved at most SOCs, except at the really low SOC (2%).

Table 5.3 SOC for each HPPC cycle of LCO

HPPC cycle	SOC (%)
1	100.0
2	86.0
3	71.9
4	57.9
5	43.9
6	29.8
7	15.8
8	1.8

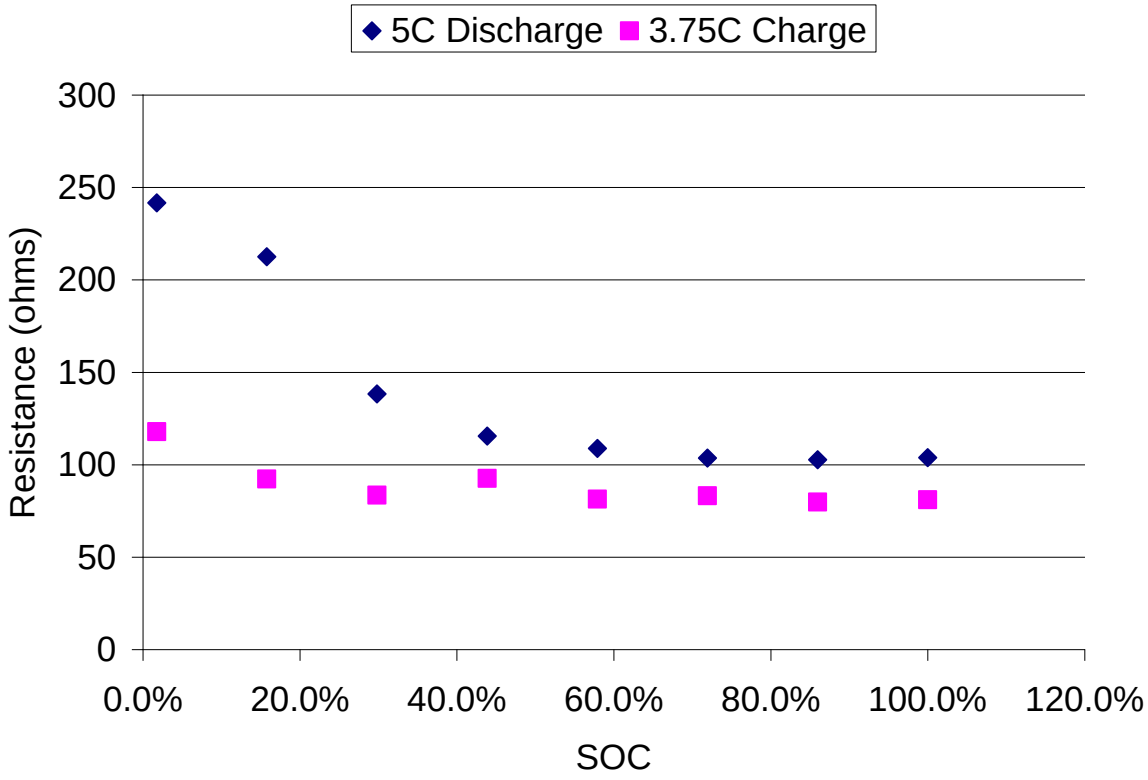

Figure 5.11 Resistance of pulse charge/discharge of LCO

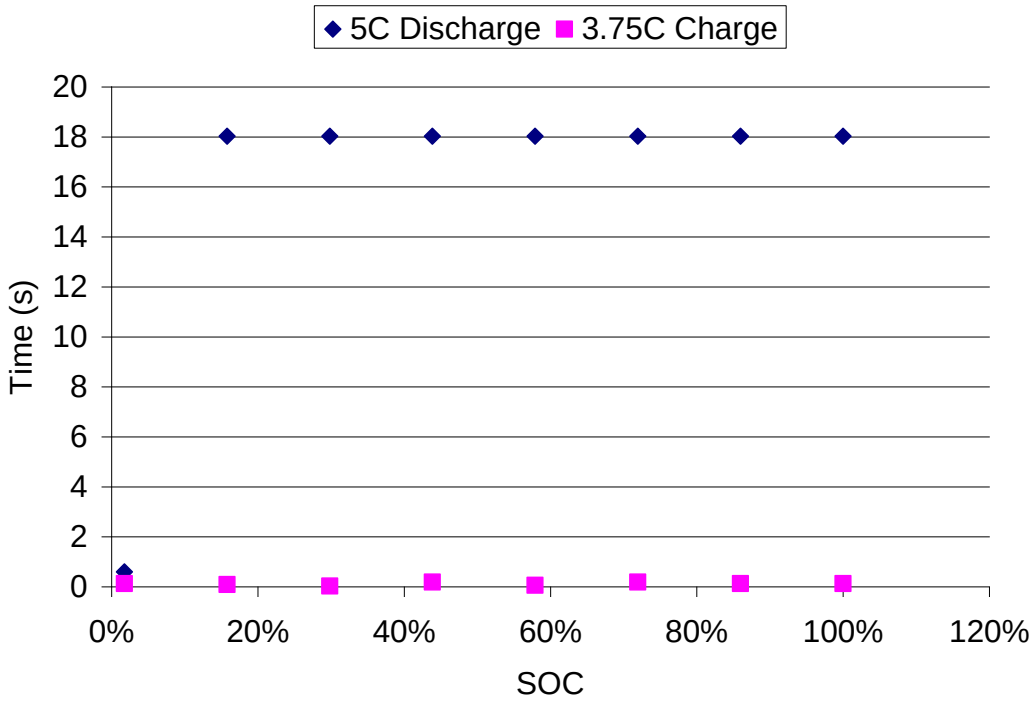

Figure 5.12 Duration of pulse charge/discharge for LCO

Figure 5.13 shows the measured potential after the one-hour resting period. The equilibrated potential of LFP shows constant potential at different SOCs. This can be attributed to the two-phase redox reaction[12] between $LiFePO_4$ and $FePO_4$. A continuous reduction of potential is observed for LCO, due to the single phase of $LiCoO_2/CoO_2$.

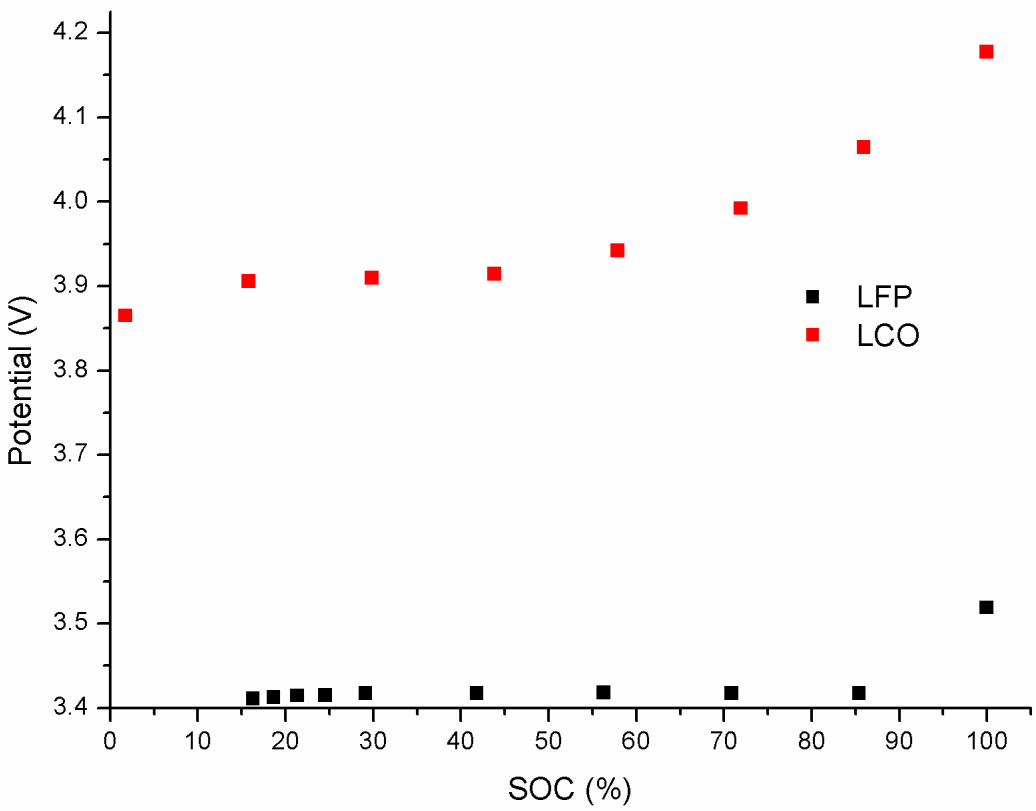

Figure 5.13 Equilibrated open-circuit potential measured after 1 h resting period after HPPC cycle

5.4 Conclusions

In conclusion, LFP is more suitable for an cathode material in electric vehicle than LCO. The full cycle of HPPC profile could be obtained using LFP half cell, but no full cycle of HPPC profile in any range of SOC could be obtained using a LCO half cell. Using the LFP half cell, the full cycle result of the HPPC profile can be obtained by within 56 to 100% of SOC for pulse discharge and all range of SOC for pulse charge for the LFP half-cell battery. Pulse discharge of LCO was possible at most SOC ranges, except for the lower range

(2%). However, pulse charge was not possible at any SOC. By testing the active materials in the half cells, it was possible to test their application for PHEVs using HPPC profiles. The results show that LFP is more practical for PHEVs when compared to LCO, since the LFP half cell could achieve the full HPPC cycle within 56% to 100% of SOC where no range of SOC was observed for LCO. Moreover, the different pulse discharge rate might have been correlated to the SOC. This requires further study. The significance of the experiment is the HPPC testing on half cells for the first time to test the individual active materials that give a direct correlation of practicality for Li-ion battery material in electric vehicles. This experiment can be used to optimize batteries for the use in PHEVs.

5.5 References:

1. Hunt, G., PNGV Battery Test Manual Rev.3. In 2001; p 40.

2. Abraham, D. P.; Poppen, S. D.; Jansen, A. N.; Liu, J.; Dees, D. W., Application of a lithium-tin reference electrode to determine electrode contributions to impedance rise in high-power lithium-ion cells. *Electrochimica Acta* **2004,** 49, (26), 4763-4775.

3. Abraham, D. P.; Reynolds, E. M.; Sammann, E.; Jansen, A. N.; Dees, D. W., Aging characteristics of high-power lithium-ion cells with LiNi 0.8Co0.15Al0.05O2 and Li 4/3Ti5/3O4 electrodes. *Electrochimica Acta* **2005,** 51, (3), 502-510.

4. Dees, D.; Gunen, E.; Abraham, D.; Jansen, A.; Prakash, J., Electrochemical modeling of lithium-ion positive electrodes during hybrid pulse power characterization tests. *Journal of the Electrochemical Society* **2008,** 155, (8).

5. Forgez, C.; Vinh Do, D.; Friedrich, G.; Morcrette, M.; Delacourt, C., Thermal modeling of a cylindrical LiFePO4/graphite lithium-ion battery. *Journal of Power Sources* 195, (9), 2961-2968.

6. Holland, C. E.; Weidner, J. W.; Dougal, R. A.; White, R. E., Experimental characterization of hybrid power systems under pulse current loads. *Journal of Power Sources* **2002,** 109, (1), 32-37.

7. Lackner, A. M.; Sherman, E.; Braatz, P. O.; David Margerum, J., High performance plastic lithium-ion battery cells for hybrid vehicles. *Journal of Power Sources* **2002,** 104, (1), 1-6.

8. Smith, K.; Wang, C. Y., Solid-state diffusion limitations on pulse operation of a lithium ion cell for hybrid electric vehicles. *Journal of Power Sources* **2006,** 161, (1), 628-639.

9. Belt, J. R.; Ho, C. D.; Motloch, C. G.; Miller, T. J.; Duong, T. Q., A capacity and power fade study of Li-ion cells during life cycle testing. *Journal of Power Sources* **2003,** 123, (2), 241-246.

10. Goodenough, J. B., Design considerations. *Solid State Ionics* **1994,** 69, (3-4), 184-198.

11. Delacourt, C.; Poizot, P.; Levasseur, S.; Masquelier, C., Size effects on carbon-free LiFePO4 powders. *Electrochemical and Solid-State Letters* **2006,** 9, (7).

12. Padhi, A. K.; Nanjundaswamy, K. S.; Goodenough, J. B., Phospho-olivines as positive-electrode materials for rechargeable lithium batteries. *Journal of the Electrochemical Society* **1997,** 144, (4), 1188-1194.

Chapter 6 Conclusions

In this thesis, new synthetic methods for $LiFePO_4$ (LFP) and SnO_2 were successfully developed, and Hybrid Pulse Power Characterization (HPPC) was tested on an LFP half-cell battery. The following is a summary of the conclusions:

1. Three-dimensionally ordered macroporous (3DOM) LFP was synthesized using new organic template-assisted synthesis. The synthesized LFP has a promising high capacity (158mAh/g) that is close to the theoretical capacity (170mAh/g).
2. Infiltration method in the organic-template assisted synthesis was improved by changing the hydrophobicity with the use of Brij 78 to synthesize 3DOM LFP.
3. New organic template-assisted hydrothermal synthesis was developed to produce of pure porous SnO_2 with 8.5% carbon contents.
4. Battery performance of the synthesized SnO_2 had 700 mAh/g of charge/discharge specific capacity with 60% efficiency and no sign of pulverization was observed.
5. The LFP was able to withstand HPPC simulation better than the LCO.

6. LFP could handle pulse discharge between 56 and 100% SOC, and pulse charge at all SOCs. LCO could handle pulse charge at most SOC ranges, much better than at lower ones (2% SOC).
7. By testing the HPPC in a half-cell battery for the first time, a new prospective of the potential phenomena of the active materials was gained.

6.1 Future work

Future work is summarized in three sections, one for each project or chapter (Chapter 3, 4 and 5).

6.1.1 Future work for Chapter 3

The main objective of this chapter was to obtain 3DOM olivine materials that have excellent performance for Li-ion batteries. In this project, the 3DOM LFP was successfully synthesized. However, further syntheses of other olivine materials are still in progress. The main problem for the other olivine materials is the preparation of the precursor solution. The use of the right mixture to prepare the solution is a major obstacle that is preventing the synthesis of a highly pure olivine material. Future work could involve achieving control of the carbon amount to optimize the battery performance during the calcination stage of olivine synthesis.

6.1.2 Future work for Chapter 4

In Chapter 4, SnO_2 was synthesized using the organic template-assisted method. The main objective was accomplished. However, battery performance with SnO_2 needs to be optimized by changing the mixture of the carbon sources (e.g. carbon graphite and carbon super S). Another big improvement could be made during the preparation of the electrodes. The SnO_2 coating on the copper foil was separating very easily. As such, it is necessary to further examine the drying conditions of the SnO_2 coating on the copper foil in order to achieve a good SnO_2 electrode.

6.1.3 Future work for Chapter 5

The objective of this chapter was to test whether the active materials could sustain the dynamic power use of electric vehicles. Simple HPPC was used to test the active materials. Two kinds of future work are suggested. Since simple HPPC was adapted to test LFP, it would be interesting to develop an HPPC profile that more closely simulates real driving conditions and test on the LFP half cell. Other future research involves testing the HPPC profile on an anode material to achieve a full voltage profile of the full cell to study the effect of the HPPC.